THESIS FOR THE DEGREE OF LICENTIATE OF PHILOSOPHY

Catalyst Design for the Valorisation of Biomass-derived Furans into Aromatics

Guido J.L. de Reijer

Department of Chemistry and Chemical Engineering
CHALMERS UNIVERSITY OF TECHNOLOGY
Göteborg, Sweden 2023

Catalyst Design for the Valorisation of Biomass-derived Furans into Aromatics

Guido J.L. de Reijer

Licentiatuppsatser vid Institutionen för kemi och kemiteknik
Chalmers tekniska högskola
Nr 2023:10

Department of Chemistry and Chemical Engineering
Chalmers University of Technology
SE-412 96 Göteborg
Telephone +46 31 772 1000

Cover:
Schematic conversion of biomass into commodity chemicals over an MFI-framework zeolite catalyst

Printed by Chalmers Digitaltryck
Göteborg, Sweden 2023

Catalyst Design for the Valorisation of Biomass-derived Furans into Aromatics
Guido J.L. de Reijer
Department of Chemistry and Chemical Engineering
Chalmers University of Technology

Abstract

Anno 2023, mankind must strive towards a more sustainable chemical industry; one that does not solely rely on fossil fuels but also utilises renewable feedstocks such as biomass. Biomass can be catalytically converted into commodity chemicals such as aromatics, through intermediates like furans. Aromatics serve as building blocks for everyday materials.

In this work, the conversion of one type of furans, 2,5-dimethylfuran, was studied at elevated temperatures in a flow reactor by using a selection of microporous, acidic catalysts. The effluent gas stream was analysed with Fourier-transform infrared spectroscopy and mass spectrometry. Zeolitic catalysts with the MFI-framework were synthesised bottom-up through hydrothermal synthesis, with aluminium or gallium substituted in their framework. Structural analysis was performed comprising X-ray fluorescence, X-ray diffraction, physisorption, thermogravimetric analysis, scanning electron microscopy, and acidity analysis by NH_3-TPD.

Both aluminium and gallium-substituted zeolites were active for converting 2,5-dimethylfuran into aromatics, of which Ga-MFI displayed superior benzene production and catalyst lifetime. Catalyst deactivation was caused by the loss of strong and extra-framework acid sites due to the coking. After deactivation towards aromatics, the intermediate products formed on weak acid sites such as 2,4-dimethylfuran, were detected as the main products.

It was found that an increase in gallium content increases catalytic activity until a limit of Si/Ga=13 was reached, at which the synthesis of the catalyst also yielded an inactive, amorphous phase. Increasing the crystallisation duration enabled approaching this limit and forming phase-pure MFI zeolite with a Si/Ga ratio of Si/Ga=17.

Mesopores were introduced to the catalyst to improve the mass transfer of reactants and products. Even though the total production of aromatics and the catalyst lifetime remained unchanged, its number of acid sites was halved implying that each acid site was able to produce twice as many aromatics.

Keywords: biomass conversion, catalysis, gallium, production of aromatics, zeolites, 2,5-dimethylfuran

List of Publications

This thesis is based on the following appended papers, referred to by Roman numerals in the text:

I. Isomorphous Subtitution of Gallium into MFI-Framework Zeolite Increases 2,5-Dimethylfuran to Aromatics Selectivity and Suppresses Catalyst Deactivation

Christopher Sauer, Guido J.L. de Reijer , Andreas Schaefer, Per-Anders Carlsson

Topics in Catalysis, **(2022)**, *doi:10.1007/s11244-022-01776-2*

II. Continuous isomerisation of 2,5-dimethylfuran to 2,4-dimethylfuran over Ga-silicate

Christopher Sauer, Guido J.L. de Reijer , Barbara Wilfinger, Anders Hellman, Per-Anders Carlsson

In manuscript

My Contributions to the Publications

Paper I

I was partially responsible for the conceptualisation, I planned and carried out the synthesis and experimental work with Christopher Sauer, I interpreted the results together with my co-authors, I wrote sections of the experimental, results and discussion, and conclusion.

Paper II

I planned and carried out experimental work and interpreted the results together with my co-authors. Responsible for review and submission.

Contents

List of Publications v

List of Figures x

List of Tables xi

List of Abbreviations xiii

1 Introduction 1

2 Background 5
2.1 Benzene, toluene, and xylenes . . . 5
2.2 Model compounds: furans . . . 6
2.3 Catalysis . . . 6
2.4 Zeolites . . . 8
2.4.1 Acidity . . . 8
2.4.2 Framework . . . 9
2.5 Objective of this thesis . . . 11

3 Methodology 13
3.1 Catalyst synthesis . . . 13
3.1.1 Synthesis protocol . . . 13
3.1.2 Sol-gel reaction . . . 16
3.2 Reaction set-up . . . 18
3.2.1 MS . . . 19
3.2.2 FTIR . . . 20
3.3 Structural analysis . . . 21
3.3.1 X-ray diffraction . . . 21
3.3.2 X-ray fluorescence . . . 23
3.3.3 Physisorption . . . 23
3.3.4 SEM and EDX . . . 25
3.3.5 TGA and DSC . . . 26
3.3.6 NH_3-TPD . . . 27

4 Results and discussion 29
4.1 Influence of incorporated metals . . . 29
4.1.1 Structural analysis . . . 29
4.1.2 Catalytic tests . . . 33
4.2 Influence of temperature . . . 39
4.3 Influence of gallium content . . . 42
4.3.1 Structural analysis . . . 42
4.3.2 Limit of gallium content . . . 48
4.3.3 Catalytic tests . . . 52

4.4 Influence of mesopores 56
4.4.1 Catalytic tests 58

5 Conclusions and future work **63**
5.1 Future directions 64

Acknowledgements **67**

Bibliography **69**

Appendix **77**

Appendix A **79**

List of Figures

1.1 World population forecast 1
1.2 World energy consumption per fuel 1
1.3 Overview components biomass 2
1.4 Overview furans 3
1.5 Overview aromatics 3

2.1 Benzene to PS 5
2.2 Para-xylene to PET 5
2.3 Cellulose to 2,5-DMF 6
2.4 Energy diagram catalysis 7
2.5 Energy diagram heterogeneous catalysis 7
2.6 Different acid sites in a zeolite 8
2.7 Building blocks MFI-framework zeolite 10

3.1 Overview synthesis 15
3.2 TEOS hydrolysis and condensation 17
3.3 Reaction rates hydrolysis and condensation of TEOS 18
3.4 Flow reactor set-up 19
3.5 FTIR spectroscopy vibrational modes 20
3.6 Schematic representation Bragg's law 21
3.7 Schematic mechanism of XRF 23
3.8 SEM interaction volume 25
3.9 Schematic NH_3-TPD profile 27

4.1 XRD patterns set 1 30
4.2 Close-up of XRD patterns set 1 30
4.3 N_2-physisorption set 1 31
4.4 TGA set 1 32
4.5 SEM images set 1 32
4.6 Main products of 2,5-DMF conversion 33
4.7 Conversion and selectivities over Ga-MFI(33) 33
4.8 Conversion and selectivities over Al-MFI 34
4.9 NH_3-TPD set 1 36
4.10 NH_3-TPD set 1, deconvoluted 37
4.11 Influence temperature over Ga-MFI(34) 39
4.12 Low temperature conversion over Ga-MFI(33) 40
4.13 Multiple cycles of 2,5-DMF conversion at 350 °C over Ga-MFI(33) . . 41
4.14 Mechanism of 2,4-DMF production 41
4.15 XRD patterns set 2 42
4.16 SEM and EDX of Ga-MFI(34) 43
4.17 SEM images set 2 44

4.18 N_2-physisorption set 2 45
4.19 TGA and DSC set 2 47
4.20 XRD patterns set 3 49
4.21 Close-up of XRD patterns set 3 49
4.22 TGA and DSC set 3 50
4.23 SEM images set 3 50
4.24 Physisorption set 3 51
4.25 Benzene production set 2 and 3 52
4.26 Conversion and selectivities over Ga-MFI(17) 53
4.27 NH_3-TPD profiles of Ga-MFI(34) 53
4.28 Overview acid sites set 2 and 3 54
4.29 XRD patterns set 4 56
4.30 TGA and DSC set 4 57
4.31 Physisorption isotherms set 4 57
4.32 Conversion over Ga-MFI(34) and Ga-MFI(34)-meso 58
4.33 Benzene production set 4 59

List of Tables

2.1 Ionic radii of metals 9
2.2 Kinetic diameters of furans and BTX 10

3.1 Overview sets of catalysts 13
3.2 Molar compositions of synthesis gels 16
3.3 Ionisation energies IMR-MS 20

4.1 XRF set 1 29
4.2 Textural properties set 1 31
4.3 Total BTX set 1, MS 35
4.4 Overview acid sites set 1 38
4.5 Total BTX per acid site set 1, MS 38
4.6 XRF set 2 42
4.7 Textural properties set 2 46
4.8 XRF set 3 48
4.9 Textural properties set 3 51
4.10 Total benzene set 2 52
4.11 Overview acid sites Ga-MFI(34) 53
4.12 NH_3-TPD set 2 and 3 54
4.13 Benzene production set 2 and 3 55
4.14 XRF set 4 56
4.15 Textural properties set 4 58
4.16 Overview acid sites set 4 60
4.17 Total benzene set 4 61

A.1 Chemicals used for synthesis 79
A.2 Overview synthesis conditions per catalyst 79
A.3 MS and FTIR settings of product analysis 80

List of Abbreviations

2,4-DMF	2,4-dimethylfuran
2,5-DMF	2,5-dimethylfuran
2-MCPO	2-methyl-2-cyclopentenone
2-MF	2-methylfuran
3-MCPO	3-methyl-2-cyclopentenone
BAS	Brønsted acid site
BET	Brunauer-Emmett-Teller
BTX	Benzene, toluene, and xylenes
CMR	Carcinogenic, mutagenic, and reptrotoxic
DRIFTS	Diffuse reflectance infrared Fourier transform spectroscopy
DSC	Differential scanning calorimetry
EDX	Energy-dispersive X-ray spectroscopy
FCC	Fluid catalytic cracking
FID	Flame ionisation detector
FTIR	Fourier-Transform infrared spectroscopy
GC	Gas chromatography
HMF	Hydroxymethylfurfural
IMR-MS	Ion-molecule-reaction mass spectrometry
IR	Infrared
LAS	Lewis acid site
MS	Mass spectrometry
PBU	Primary building unit
PET	Polyethylene terephthalate
PS	Polystyrene
SAXS	Small-angle X-ray scattering
SBU	Secondary building unit
scXRD	Single-crystal X-ray diffraction
SDA	Structure directing agent
SEM	Scanning electron microscopy
SNR	Signal-to-noise ratio
SSA	Specific surface area
ssNMR	Solid-state nuclear magnetic resonance
TCD	Thermal conductivity detector
TEM	Transmission electron microscopy
TEOS	Tetraethyl orthosilicate
TGA	Thermogravimetric analysis
TOS	Time-on-stream
TPA	Tetrapropylammonium
TPO	Temperature-programmed oxidation
XRD	X-Ray diffraction
XRF	X-Ray fluorescence

Introduction 1

At this moment, more than 8 billion people inhabit the earth, a number that is only predicted to rise and reach nearly 10 billion by 2050 (figure 1.1) [1, 2]. Simultaneously, an increasing amount of people are growing accustomed to a luxurious lifestyle, rich in bulging refrigerators, carefree travels around the globe, and easy access to numerous services and commodities with only a few clicks on a smartphone or computer. Human development, whether it be social, economic or technical, related to welfare or health, requires two main ingredients: energy and materials. . . and lots of it [3].

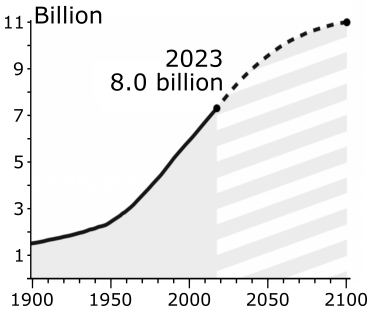

Figure 1.1: Predicted growth of mankind [1, 2]. Adapted from [4].

Humanity has always found ways to use the earth's resources for survival and prosperity, but several defining eras have played a major role in shaping today's world: the four Industrial Revolutions [5]. Starting in the 1800s, the first and most well-known Industrial Revolution is characterised by the transition towards steam-powered production and processes, fuelled by burning the most abundant fossil fuel: coal [6]. The Second Industrial Revolution, also known as the Technological Revolution, is characterised by the large-scale use of steel, electricity, chemicals, and fossil fuels like oil and gas, leading to mass production. The Third Industrial Revolution, or Digital Revolution, refers to electronics, internet, and nuclear energy, [7, 8] whereas the Fourth Industrial Revolution, although less defined, refers to cyber-physical systems and renewable energy [9]. Throughout all these eras, fossil fuels like coal, oil, and gas, have literally skyrocketed mankind forwards in numerous fields, acting as an energy source for heat and electricity, as well as a feedstock for chemicals and fuels.

Alas, the use of fossil fuels is not without disadvantages: extracting them induces land degradation while consuming or burning them emits harmful pollutants into the earth's water reserves and atmosphere. These emissions consist of air pollutants such as organic, metal, and particulate matter, as well as toxic greenhouse gases such as sulphur, nitrogen, and carbon oxides. Air pollutants cause serious harm to the environment and human health, [11] whereas greenhouse gases contribute to the warming of the earth's atmosphere, [11–13] resulting in rising sea levels and floods, increased droughts and extreme weather, and mass extinction [14–17]. Unfortunately, today the world is still largely dependent on fossil fuels for energy and the synthesis of chemicals (figure 1.2).

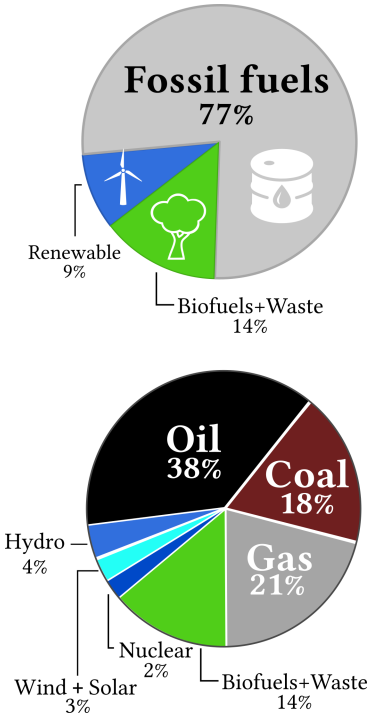

Figure 1.2: Gross world energy consumption (2020) per fuel including fossil fuels (coal, oil, and gas), biofuels and waste, and renewable sources (nuclear, hydro, wind, solar) [10].

These effects are not new as researchers in 1968 [18] already predicted a rise in atmospheric carbon dioxide (CO_2) levels to 400 ppm

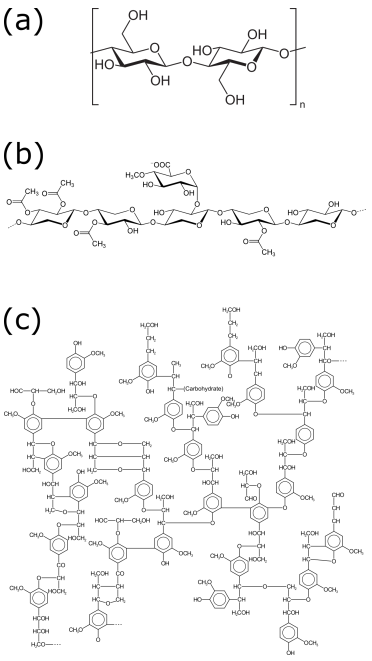

Figure 1.3: Complex molecules present in biomass including cellulose (a), hemicellulose (b), and lignin (c).

by the year 2000, accompanied by an increase in global temperature. Currently, CO_2 levels have passed 420 ppm and mean global temperature has risen by 1.08 °C since 1968, [19, 20] or by 0.8 °C compared to the 20th-century average [21].

Following these predictions, albeit several years later in 1987, the first global efforts were made to introduce sustainable energy development on the global, political agenda [22]. Since then, there have been both gradual and rapid approaches to increase political, economic and technological interest in renewable energy sources such as solar, wind, marine, hydro, geothermal, and biomass-derived energy [23–25]. This process is stimulated by international agreements like the Paris Agreement in 2015 and the more recent Glasgow climate pact in 2021 [26, 27]. Renewable energy comes from natural, abundant sources which are generally replenished quicker than they are consumed [28]. By contrast, fossil fuels are formed by the slow, geological compression of prehistoric organic matter, a process that takes millions of years, and are therefore exhaustible on a human timescale [29, 30]. Moreover, renewable energy sources result in the emission of fewer harmful pollutants, reducing global warming and other negative effects associated with fossil fuels, such as smog, acid precipitation, and stratospheric ozone depletion [23].

Besides using renewable sources, such as biomass or recycled plastics, for energy in the form of electricity or heat, they can also be used to produce chemicals and materials sustainably. When referring to biomass, all biological matter on earth is included, such as plants, trees, and food crops, as well as agricultural and municipal waste. During its lifetime, the organic matter has sequestered carbon from the air as CO_2 through photosynthesis, which can subsequently be used as feedstock for chemicals. When burning biomass as fuel, this carbon is released similarly to when burning fossil fuels, which means that it can only be sustainable if a few conditions are met.[1] In contrast, if biomass is used as a feedstock for chemicals, its carbon atoms are captured and reused instead of emitted as pollutants.

Over the last few decades, new processes have been developed in which biomass is converted either via new synthesis routes or via existing routes that are currently used to convert fossil fuels. However, these processes are not always net-zero or net-negative regarding CO_2 emissions, nor are they compatible with existing technical and economical infrastructure. That is why continued funding, efforts, and research into this field are essential.

As for this licentiate thesis, one route of converting biomass will be explored in more detail. Biomass is not simply one molecule but has many different components, built up of complex molecules

1: Conditions for sustainable burning of biomass:

- New biomass must be replenished at a higher rate than or similar rate as its use.
- Biodiversity must be maintained.
- Biomass may not compete with food supply.

such as cellulose, hemicellulose and lignin (figure 1.3). As a result, their conversion into chemicals is also complex and often requires an external component to enhance the reaction rate and selectivity, such as a catalyst (section 2.3). A catalyst is an additional material or molecule that enhances the reaction rate by allowing for a different pathway to occur which requires less activation energy.

Studying the role of the catalyst is vital to understand the reaction mechanisms and design the ideal catalyst: one that maximises conversion of reactants or selectivity towards products, or both. Unfortunately, the heterogeneous composition of biomass, as well as the presence of water, make it difficult to investigate the catalyst. Linking the observed catalytic performance to the properties of the catalyst may be hindered. This issue is solved by using pure, model compounds instead of raw biomass.

The model compounds used in this thesis are furans (figure 1.4) which can be derived from biomass in a few steps, as further described in section 2.2. Furans can subsequently be converted into more valuable, commodity chemicals, such as the aromatics benzene, toluene, and xylenes (BTX, figure 1.5).

These aromatics are chemical building blocks and can in turn be used in the synthesis of solvents, plastics, resins, dyes and pharmaceuticals [31, 32]. This reaction has been studied before using different experimental set-ups, such as batch or flow reactors, and using a multitude of different catalysts, often zeolites (section 2.4). Here, the conversion of one type of furans, 2,5-dimethylfuran (2,5-DMF), into aromatics is studied.

To elaborate, this licentiate thesis aims to contribute to the design and development of new catalysts for the conversion of 2,5-DMF, as well as contribute to a better understanding of the reaction pathways.

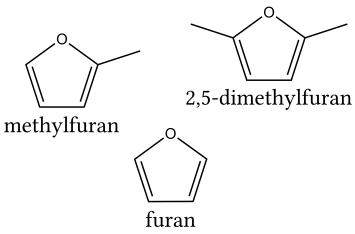

Figure 1.4: Furan-based molecules used as model compounds.

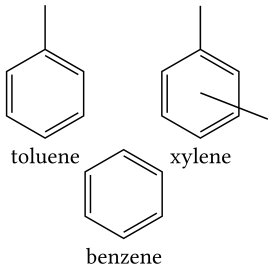

Figure 1.5: Benzene-based molecules as desired products.

Background 2

This section elaborates on the need for chemicals and the available feedstocks that can be used. Then the concept of catalysis is introduced, and the class of catalyst used in this study, zeolites, is described. Finally, the research objective and aiding questions of this thesis are stated.

2.1 BTX 5
2.2 Furans 6
2.3 Catalysis 6
2.4 Zeolites 8
2.4.1 Acidity 8
2.4.2 Framework 9
2.5 Objective thesis 11

2.1 Benzene, toluene, and xylenes

To demonstrate the demand for aromatics, its market size was valued at roughly 212 billion USD in 2023 and it is expected to grow by 5.6 % annually during the next ten years, up to a value of 328 billion by 2032 [33]. As mentioned before, BTX has applications varying from solvents, plastics, resins, dyes, paints, coatings, and rubbers, to pharmaceuticals. For example, benzene is involved in the manufacturing of e.g., polystyrene (PS) through ethylbenzene (figure 2.1), whereas para-xylene[1] is converted into terephthalic acid and further into polyethylene terephthalate (PET, figure 2.2).

Nowadays, over 95 % of BTX derives from crude oil, and is produced through steam cracking and catalytic reforming of naphtha, a liquid hydrocarbon mixture [34–36]. Research into the use of other sources to produce BTX, such as biomass, is emerging [32]. For example, biomass can be converted into syngas ($CO + H_2$) through gasification[2] which subsequently can be converted into fuels or BTX [37]. Moreover, catalytic pyrolysis[3] can convert biomass selectively into aromatics when using zeolites as catalysts [38, 39]. Although these processes have not been developed to the same degree as the fossil-fuel industry yet, they can offer a promising alternative to fossil fuels as a feedstock for chemicals.

Especially in the Nordic countries, which are rich in biomass, there is an uncovered potential for the conversion of biomass into—not only aromatics—but also fuels, fertiliser and gas [40, 41]. To illustrate, Sweden has the largest forest area in the EU, with nearly 17 % of all European forests in 2020, followed by Finland with more than 13 % [42].

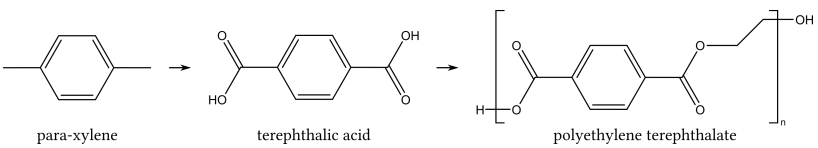

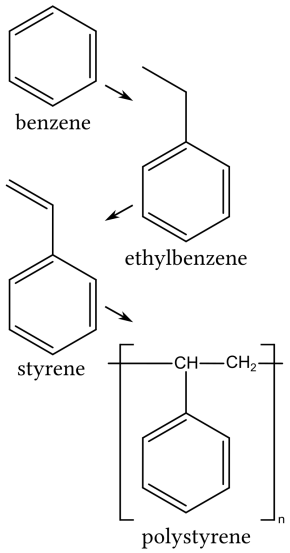

Figure 2.1: Schematic of the stepwise conversion of benzene to polystyrene

1: the two methyl groups in xylene can be bound to different carbon atoms of the ring, resulting in meta-, ortho-, and para-xylene.

2: gasification is high-temperature conversion under controlled atmosphere, such as oxygen or steam.

3: pyrolysis is decomposition in the absence of air.

Figure 2.2: Schematic of the stepwise conversion of para-xylene to polyethylene terephthalate.

2.2 Model compounds: furans

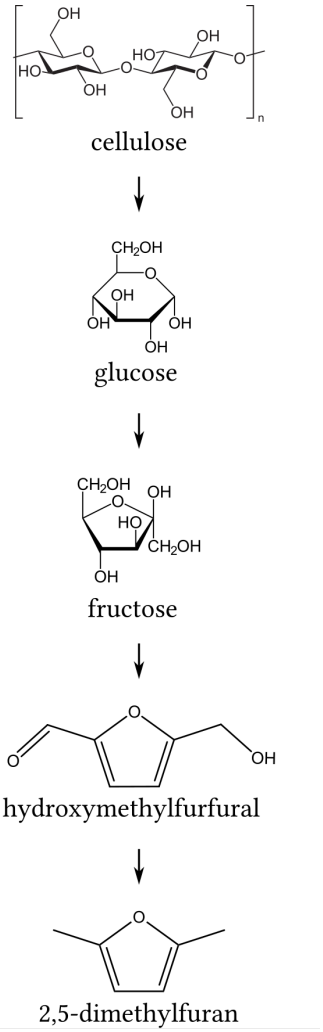

Figure 2.3: Schematic stepwise conversion of cellulose into 2,5-dimethylfuran.

As mentioned in the introduction, the three main components of lignocellulosic biomass are the polymers cellulose, hemicellulose, and lignin, which amount to 35 to 55 %, 20 to 35 %, and 10 to 30 % of biomass, respectively [43]. These components can be broken down into so-called platform molecules: bio-derived chemicals that serve as building blocks for the production of commodity chemicals [44]. Producing these platform molecules is not easy, since the three main biomass components should first be separated and then pretreated in which the largest polymers are broken down physically, chemically, or biochemically [45]. When pretreating with an acid, cellulose and hemicellulose are rapidly hydrolysed to glucose and xylose, respectively. Glucose can isomerise to fructose, which can then be converted into hydroxymethylfurfural (HMF) by an acidic catalyst. Finally, HMF can be converted into many high-value chemicals, such as 2,5-DMF and furan derivatives (figure 2.3).

In this thesis, 2,5-DMF is used as a model compound instead of raw biomass. This eliminates several problems that arise when using raw biomass, relating to its heterogeneity as well as the complexity of its composition. By using pure 2,5-DMF, the properties of the catalyst, such as its acidity, metal content, and morphology, can be linked to the catalytic activity. Moreover, investigation of this reaction may lead to new insights that can be translated into existing or developing biorefineries.

Other furanic compounds, such as furan and 2-methylfuran (2-MF), may also be of interest, as these can successfully be converted into aromatics [46–48]. However, when using 2,5-DMF and co-reagents such as ethene, para-xylene has been selectively synthesised in batch and flow reactors, one of the more valuable aromatics [49, 50]. Moreover, 2,5-DMF is the safest furan to handle since 2-MF is fatal when inhaled and furan may be carcinogenic, mutagenic, and reprotoxic (CMR).

2.3 Catalysis

As briefly mentioned before, a catalyst is a tertiary material or molecule that increases the reaction rate. It takes part in the reaction and may even change in structure but it may not undergo a net chemical change and must be regenerated at the end of the reaction [51]. To be more precise, the overall change in Gibbs energy the reaction is not changed, which is demonstrated in figure 2.4 [52]. In an uncatalysed reaction, reactants must overcome a large energy barrier before being converted into products, while addition of

a catalyst enables a different pathway that requires a smaller activation energy (E_a). As can be seen, the final energy of the products remains the same in both cases, following the second law of thermodynamics, which demonstrates that the catalyst does not change the net energy difference between reactants and products (ΔG).

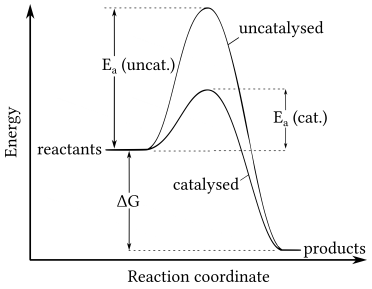

Figure 2.4: Schematic potential energy diagram of an uncatalysed and catalysed reaction

There are two main types of catalysis: homo- and heterogeneous catalysis [52]. Homogeneous catalysis refers to a system in which the catalyst and reactants are in the same phase, while in heterogeneous catalysis, the reaction takes place at or near an interface between different phases [52–54].

To elaborate on the latter, heterogeneous systems generally contain catalysts in their solid phase and reactants and products in their liquid or gaseous phase. As opposed to homogeneous catalysts, not every molecule or catalytic entity can act as an active site, making heterogeneous catalysts intrinsically less active and selective [55]. Instead, active sites, such as metals, are often supported by a porous supports which both allows for the stabilisation of the active catalytic sites, and maximises the accessible surface area. As a result, transport phenomena such as diffusion of the reagents play a large role, and catalysts must be designed accordingly [56].

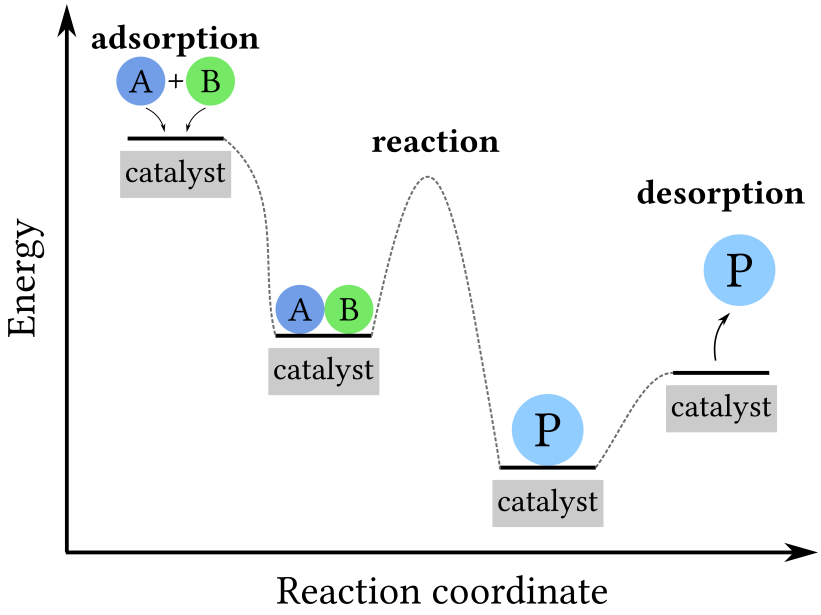

Figure 2.5: Simple schematic conversion of molecule A and B to product P over a heterogeneous catalyst via elementary steps.

As displayed in figure 2.5, heterogeneous catalysis involves several elementary steps: diffusion of reactants *A* and *B* to the catalytic surface followed by adsorption, after which they are converted into product *P*. This subsequently desorbs and diffuses away. In practice, reactions may occur via multiple competing pathways, potentially through several transition states, resulting in complex mechanisms and product mixtures.

Solid catalysts used in heterogeneous catalysis possess high robustness and thermal stability, and their properties are readily tuneable [57]. The separation between the products and catalysts is often facile and the catalysts can be recycled. For this reason, around 80 % of all catalysts used in industry are heterogeneous catalysts, and around 90 % of all chemical manufacturing processes involve the use of catalysts [58, 59].

2.4 Zeolites

One class of solid catalysts that has been extensively used and studied comprises zeolites. Zeolites are porous, crystalline materials that possess high surface areas, typically ranging from 500 to 800 $m^2\ g^{-1}$ [60]. They consist of silicon, oxygen, and aluminium, which can form tetrahedrons (TO_4 with T=Si or Al).[4] These tetrahedrons can combine into rings of different sizes, that subsequently form complex, three-dimensional structures. At the time of writing, 264 unique framework structures[5] exist [61], each with different morphologies and pore sizes[6] optimised for applications ranging from molecular sieves to acidic catalysts. For example, zeolites are used in the cracking of crude oil in fluid catalytic cracking (FCC) processes, in the conversion of methanol-to-hydrocarbons, and the direct conversion of methane-to-methanol [64–66].

They possess high thermal stability up to 700 °C, demonstrate shape selectivity due to their micropores, and have readily modifiable properties and acid sites.

4: or $TO_{4/2}$ since each oxygen is bonded to 2 T metals.

5: denoted with 3-letter codes, such as MFI, FAU, and MOR

6: micropores are < 2 nm, mesopores are between 2 and 50 nm, and macropores are > 50 nm [62, 63].

2.4.1 Acidity

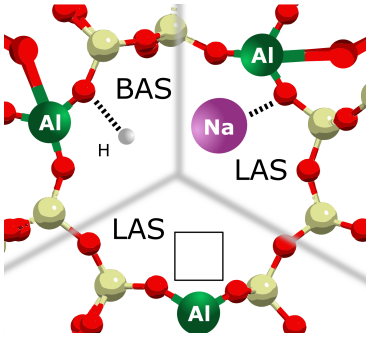

Figure 2.6: Schematic overview of three different acid sites in a zeolite. A proton in the cationic position creates a BAS while metals or empty orbitals create a LAS.

Zeolite acidity is introduced through the isomorphous substitution of a tetravalent silicon atom by a trivalent aluminium atom. Consequently, a negatively charged aluminium tetrahedron, $[AlO_4]^-$, is formed. In order to compensate for this negative charge, a positively charged counterion coordinates to the framework to maintain total framework electroneutrality. Examples include metal cations such as Na^+ and Cu^+, extra-framework aluminium species such as $[AlO]^+$ and $[Al(OH)_2]^+$, or protons, H^+ [67]. This proton creates a Brønsted acid site (BAS) and extra-framework metal species create Lewis acid sites (LAS), shown in figure 2.6. When framework defects are present or dehydration occurs, framework silicon or aluminium is not fully saturated and will have empty orbitals instead [68]. These coordinately unsaturated sites are able to accept electron pairs and thus function as Lewis acid sites.

The acidity of a zeolite plays an important role in their catalytic performance, and it is relatively easy to substitute framework silicon atoms with metals such as aluminium, or to induce acidity by adding promotors inside the pores of the zeolite through ion exchange or impregnation.

Increasing the number of acid sites can be done by increasing the amount of added metals. However, the strength of each acid site does not change if the same metal is used.[7] Fortunately, zeolites can also be made by substituting silicon with different trivalent or tetravalent metals, such as gallium, boron, iron, and titanium.[8] The degree of substitution and the success of the synthesis depends on factors such as the valency of the metal, its electronegativity, and its size (table 2.1).

7: at high contents or loading of aluminium, acid sites will be close enough to one another that they can interact and change the strength of the acid sites.

8: the term zeolite is officially reserved for materials containing silicon and aluminium and the term zeotype is used when no aluminium is present. For clarity, this thesis will refer to zeolites for each catalyst.

Both LAS and BAS play an important role in catalysis, promoting reactions like cracking, decarbonylation and dehydration; all involved in the conversion of furans to aromatics. When there are too many acid sites, or when the acid sites are too strong, unwanted reactions may take place. In biomass conversion, the formation of carbonaceous, polyaromatic, or graphite-like species can occur, named coke. These species can block acid sites, block active sites, or inhibit the reaction in general, leading to catalyst deactivation. Therefore, the acidity of the catalyst must be tuned accordingly.

Table 2.1: Overview the different effective ionic radii of metal cations at a certain oxidation state and hexacoordinated [69]. For Fe(III), the value in brackets is high-spin.

Metal	Ionic radius/ pm
Si(IV)	40
Al(III)	54
Ga(III)	62
B(III)	27
Fe(III)	55 (65)
Ti(IV)	75

2.4.2 Framework

The neutral $[SiO_4]$ and charged $[AlO_4]^-$ tetrahedrons are the primary building units (PBU) of a zeolite structure and can connect by sharing the oxygen atom. This leads to the formation of secondary building units (SBU) which can resemble both single or double 4- and 6-membered rings, as well as more complex shapes such as the pentasil unit (figure 2.7, B). The SBU can bond and form three-dimensional structures with large pores and cages at the intersection point of channels. Typical pore diameters are 3.8 Å for 6-membered rings in CHA-zeolite, 5.5 Å for 10-membered rings in MFI, or 7.4 Å for larger 12-membered rings in FAU [61]. The framework of the zeolite plays an important role since it controls which reactants are able to enter the porous structure and reach the active sites. Additionally, it puts constraints on the size of the formed products and can promote reactivity due to close proximity of the surface.

For the conversion of furans into monoaromatics, like BTX, zeolites with the MFI-framework are a suitable choice; commonly known as ZSM-5 if aluminium is in its framework.

The structure of the MFI-framework is shown in figure 2.7. The pentasil units orient in such a way that the MFI-framework is

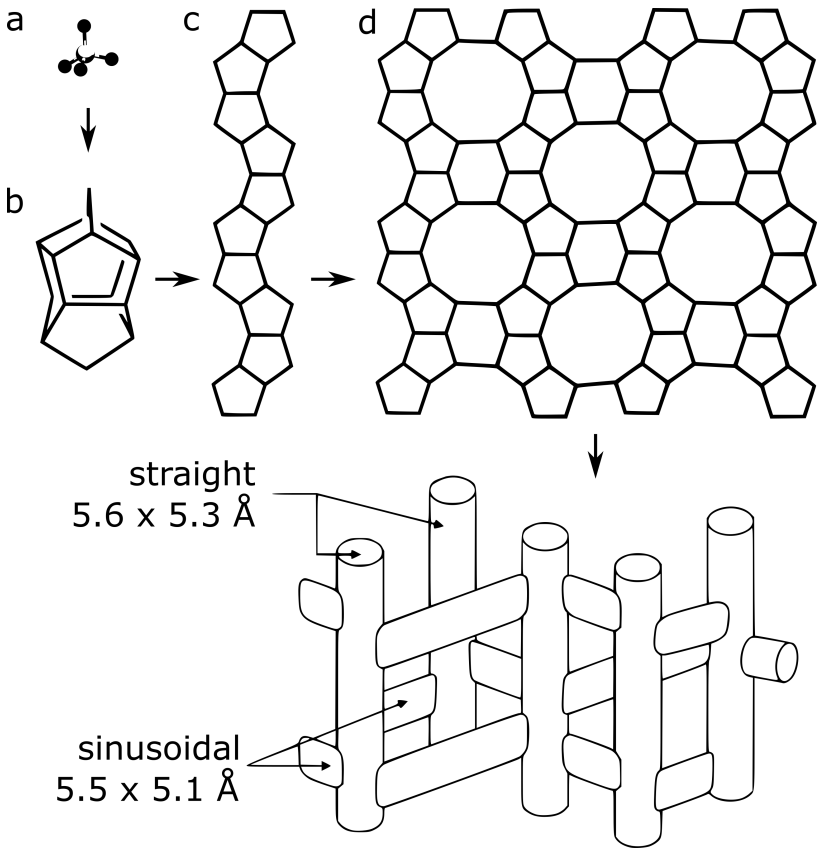

Figure 2.7: Schematic overview of the different building blocks of MFI-framework zeolite. Tetrahedrons (A), combing to form pentasil units (B), chains, and sheets with 10-membered rings. These combine to form a three-dimensional MFI structure with straight and sinusoidal pores. Adapted from [70].

formed with two 10-membered pores: straight channels of 5.6 by 5.3 Å and sinusoidal channels of 5.5 by 5.1 Å. As these dimensions are close to the kinetic diameters of furans and monoaromatics, table 2.2, MFI zeolite is able to selectively convert furans into BTX.[9]

Although it might seem that the reactants and products do not fit the MFI pores, their presence inside the pores has been experimentally observed [74, 75]. This can be explained by the erroneous use of atomic radii to calculate the pores, which actually underestimates their size [76]. At elevated reaction temperatures, such as 500 °C, the pores are dilated and their effective size is better described with the Norman radii of 6.2 and 6.3 Å [73, 77]. Pore flexibility has also been observed before for specific molecules [78, 79].

In this thesis, only MFI-framework catalysts will be discussed due to their superior selectivity towards BTX.

9: when aluminium is in the framework, the zeolite is commonly known as ZSM-5. Here, the term Al-MFI is used.

Table 2.2: Kinetic diameters of furans and BTX, demonstrating their narrow fit in the MFI-framework zeolite [71–73].

Molecule	Kinetic diameter/ Å
Furan	5.10
2-MF	5.30
2,5-DMF	5.70
Benzene	5.85
Toluene	5.85
Para-xylene	5.85
Meta-xylene	6.80
Ortho-xylene	6.80

2.5 Objective of this thesis

Now that the topic has been introduced and the background has been provided, the objective of this thesis can be defined as the following:

To understand the relationship between the properties of the catalyst, such as acidity, and its catalytic performance, regarding activity, selectivity, and stability in the conversion of 2,5-dimethylfuran into aromatics.

This objective will be explored by means of the following research questions:

1. What is the influence of metal substitution in MFI-framework catalysts, concerning aluminium and gallium?
2. What is the influence of changing the reaction conditions, such as the temperature?
3. What is the influence of changing the gallium content in MFI-framework catalysts?
4. How can the pore structure of the catalyst be influenced to enhance catalytic performance?

Methodology 3

This section starts by describing the synthesis methods of different catalysts. This is followed by a description of the characterisation methods and the catalytic experiments.

3.1 Catalyst synthesis . . . 13
3.1.1 Synthesis protocol . . . 13
3.1.2 Sol-gel reaction 16
3.2 Reaction set-up 18
3.2.1 MS 19
3.2.2 FTIR 20
3.3 Structural analysis . . 21
3.3.1 XRD 21
3.3.2 XRF 23
3.3.3 Physisorption 23
3.3.4 SEM and EDX 25
3.3.5 TGA and DSC 26
3.3.6 NH_3-TPD 27

3.1 Catalyst synthesis

The catalysts that have been studied for the conversion of 2,5-DMF into aromatics can be divided into four sets, each focusing on a specific part of the objective of this thesis. All sets consist of MFI-framework zeolites, either purely siliceous or substituted with gallium or aluminium. An overview of the catalysts is given in table 3.1.

Table 3.1: Overview sets of catalysts

	Set 1	Set 2	Set 3	Set 4
Aim	Effect metal	Effect gallium	Limit gallium	Effect mesopores
Catalysts	Si-MFI	Ga-MFI(238)	Ga-MFI(17)	Ga-MFI(95)-meso
	Al-MFI(11)*	Ga-MFI(95)	Ga-MFI(8)	Ga-MFI(34)-meso
	Al-MFI(41)	Ga-MFI(34)	Ga-MFI(7)	
	Ga-MFI(33)	Ga-MFI(13)		

* H-ZSM-5 (AkzoNobel, Si/Al=11)

The catalysts are named *X-Y(Z)-W*, in which *X* signifies the isomorphously substituted metal in the framework position, like gallium, aluminium, silicon, *Y* signifies the three-letter zeolite framework code which is MFI for all catalysts, *Z* signifies the Si/M ratio of the catalyst, determined experimentally.[1] *W* indicates any post-synthesis modification performed, such as the addition of mesopores in set 4, e.g., Ga-MFI(34)-meso.[2] Most of the catalysts reported in this thesis are in their protic form, H-Ga-MFI, and this prefix is omitted for clarity. Except for TPA-Ga-MFI, which still contains the template cations, tetrapropylammonium (TPA).

1: Example: Ga-MFI(17) is an MFI framework zeolite with gallium substituted in the framework, and Si/Ga=17.

2: in set 4, the Si/M ratio of the parent catalyst is used for clarity, even though slight differences were measured with elemental analysis.

3.1.1 Synthesis protocol

For the bottom-up synthesis of MFI-framework zeolites (set 1 to 3), a method by Creci et al. [80] was followed, which was based on an earlier method from Szostak et al. [81] to incorporate iron into MFI-framework zeolites.

In short, the synthesis consists of several steps, as illustrated in figure 3.1 and described below:

3: silicon source (tetraethyl orthosilicate, TEOS), aluminium or gallium source, structure directing agent (SDA, such as TPA), a mineraliser or pH control agent (NaOH), and a solvent (Mili-Q, H_2O)

4: 5 to 10 days at 170 °C

1. Mixing of precursors.[3] Through a sol-gel process, the precursors form a three-dimensional matrix (Si−M−SDA, with M=Al or Ga), which is the basis of the zeolite.
2. Crystallisation[4] of the precursor gel into the zeolite under high temperature and pressure. This is followed by filtration under vacuum over a Büchner funnel and washing with demineralised water to separate the formed zeolite from unreacted precursor material. A freeze-drying step removes the water from the pores without damaging the framework. The formed zeolite, structure A, contains (TPA^+) cations in the pores, as well as gallium or aluminium in the framework position, e.g., TPA-Ga-MFI.

5: 5 h at 500 °C or 550 °C (1 to 5 °C min^{-1} ramp)

3. Calcination[5] of the as-synthesized zeolite in air to remove the SDA present in the zeolite pores by oxidation. The negative framework charge induced by gallium or aluminium is compensated by other cations present, such as Na^+, which originate from the pH control agent, sodium hydroxide. Structure B, e.g., Na-Ga-MFI.

6: stirring in a 1 M NH_4NO_3 solution for 24 h

4. Ion exchange[6] of the zeolite was followed by filtration, washing with water and another cycle of ion exchange. Here, the Na^+ cations are replaced by $NH_4{}^+$+ cations, as shown in structure C, e.g., NH_4-Ga-MFI. Followed by freeze-drying overnight.

7: 5 h at 550 °C (1 to 4 °C min^{-1} ramp)

5. Calcination[7] converts the ammonium cation into a proton at the cationic position, releasing ammonia (NH_3). Structure D, e.g., H-Ga-MFI. Direct ion exchange of Na-Ga-MFI with a strong acid can also form protons but this treatment would degrade the zeolite framework by inducing defects and leaching of aluminium and gallium.

An overview of the chemicals used and their origins is shown in Appendix A (table A.1)

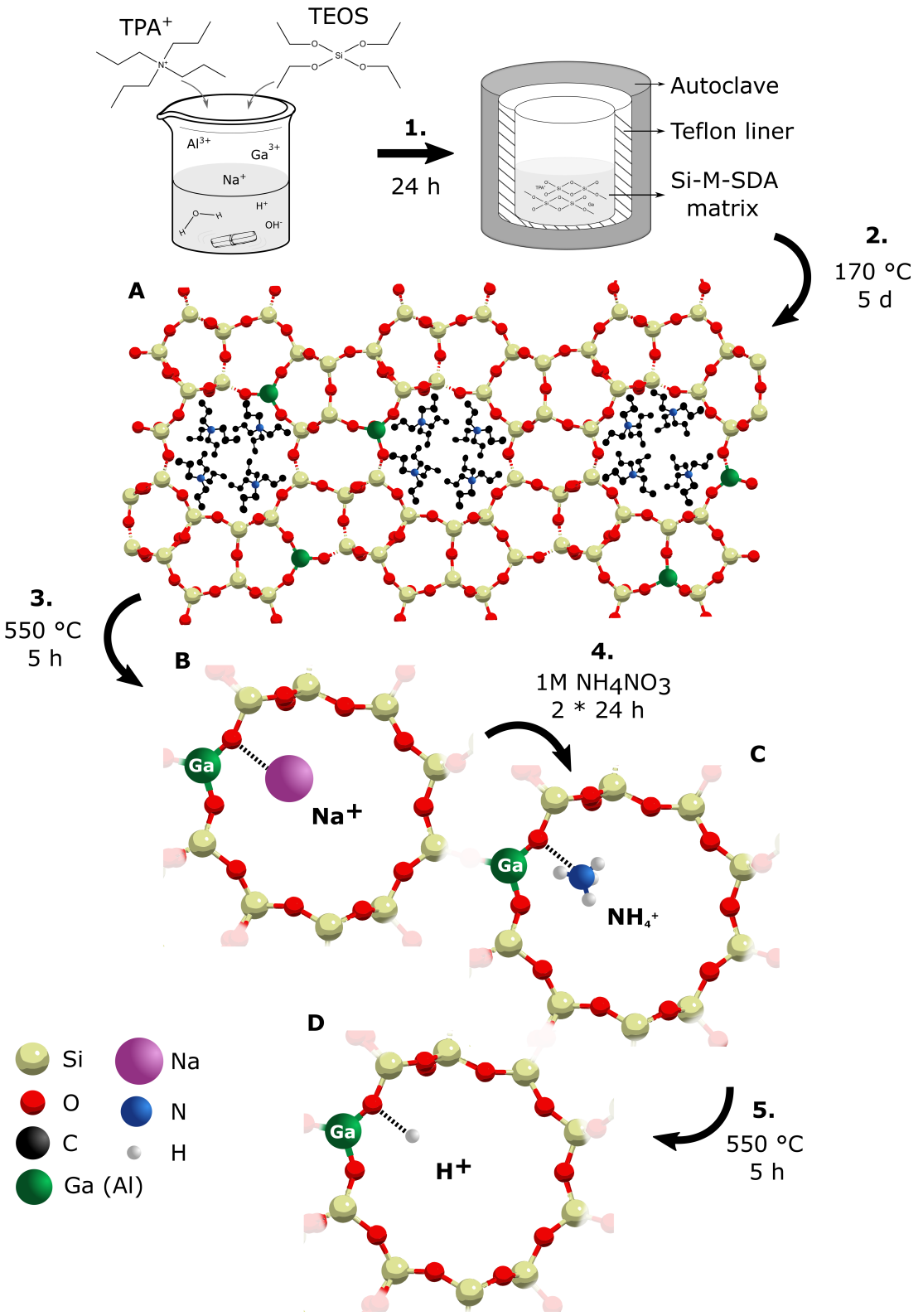

Figure 3.1: Schematic overview of the bottom-up synthesis of metal substituted MFI-framework zeolite. First, all precursors are mixed (1) and heated in an autoclave for 5 to 10 days (2). The formed TPA-MFI zeolite (A) is calcined (3) to remove the TPA^+ cations and replace them with sodium cations (B). ion exchange (4) replaces Na^+ by NH_4^+ (C) after which final calcination (5) results in the synthesis of the acidic, protic form of the zeolite, H-MFI (D). MFI framework (Si, O) was experimentally measured with single-crystal X-ray diffraction (scXRD) and visualised with Mercury. Other atoms are manually added, sizes not to scale.

The molar ratios between the precursors in the synthesis gels are given in table 3.2, and a full overview of the synthesis conditions is given in Appendix A (table A.2). There are some slight variations in synthesis gel compositions between and within sets, as well as differences in calcination and ion exchange procedures due to synthesis optimisations. Calcination temperatures were increased based on thermogravimetric analysis (TGA) and the temperature ramp was reduced to minimise metal migration and damage to the framework due to exothermic SDA oxidation. Variation in water and sodium content is caused by the different amount of acidic gallium precursor used.[8] A higher amount of sodium hydroxide was added at high Ga contents to ensure the basic conditions needed for crystallisation were met.

8: 50 g/L $Ga(NO_3)_3 \cdot H_2O$ in H_2O at 20 °C equals pH=2

Table 3.2: Molar compositions of synthesis gels

Set	Si	M (Al or Ga)	TPA^+	H_2O
1	1	0.02	0.3	25
2	1	0.006 to 0.1	0.3	25 to 37
3	1	0.05 to 0.08	0.3	20 to 37

The catalysts of set 4 were prepared according to a method from Zhang et al. [82] in which they introduced mesopores and macropores in Fe-MFI zeolite through a post-synthesis treatment consisting of a secondary dissolution-crystallisation step. Here, 1 g of parent zeolite (Ga-MFI(34) or Ga-MFI(95) from set 2) was mixed with Milli-Q water and TPAOH (0.2 M TPA^+) for 2 hours. Then the mixture was transferred to a Teflon-lined autoclave and heated to 170 °C for 24 hours. Afterwards, the mixture was filtered and washed with Milli-Q, followed by freeze-drying overnight and a final calcination step in air at 550 °C for 3 hours (2 °C/min).

3.1.2 Sol-gel reaction

The first step in the synthesis of the catalysts is the formation of the silicon-metal matrix. When using an organic silicate as a silicon source, such as TEOS, the zeolite precursor is formed through hydrolysis followed by condensation (figure 3.2). This results in a network of cross-linked silica material, with the metal homo- or heterogeneously dispersed throughout. TEOS hydrolysis can be catalysed by acid (pH<2) and basic (pH>2) conditions since the isoelectric points of silica compounds lie around pH=2 [83, 84].

In acidic medium, protonation of TEOS is followed by nucleophilic attack of water from the rear, forming an S_N2-type transition state (figure 3.2) [85–88]. The alcohol group, C_2H_5OH, gains a positive charge and becomes a better leaving group, resulting in the transformation of an alkoxysilyl group (Si–OR) into a hydroxylsilyl group, also named silanols[9] (Si–OH). Afterwards, condensation

9: or silinals

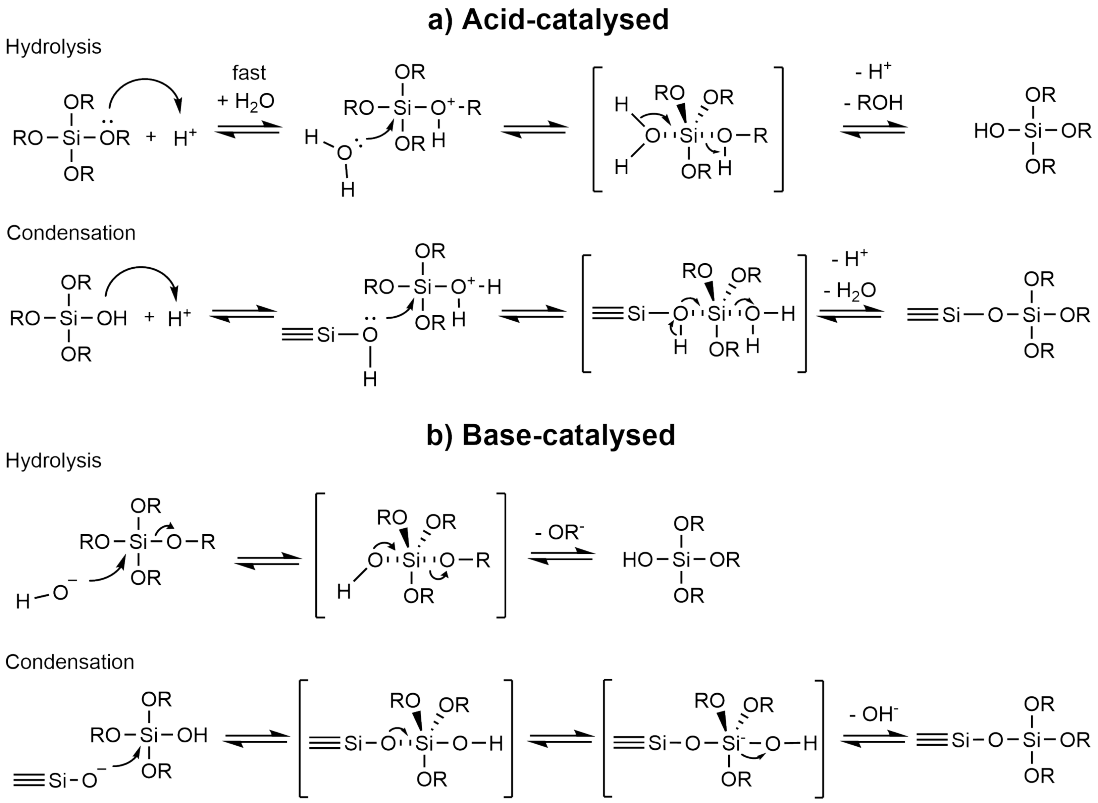

Figure 3.2: General mechanism of the hydrolysis and condensation of silicon alkoxides, both acid and base catalysed. For TEOS, R=C_2H_5. Condensation can release both alcohol and water when the monomer is hydrolysed, the latter shown here. Hashed lines indicate partial bonds and bond lengths and angles are schematically displayed. Adapted from [84].

occurs via two different S_N1-type pathways: Si−O−Si bond formation under the release of alcohol, −ROH named alkoxolation, or under the release of water when R=H, named oxolation. Because of the tetracoordinated silicon atom in TEOS, hydrolysis and condensation can occur at each of the equivalent ethoxy groups, leading to polymerisation into a heavily interconnected network of monomers that have each been hydrolysed to a different degree. This stable, three-dimensional matrix is the basis for the zeolitic building blocks that can crystallise later into a zeolite.

In a basic medium, a similar penta-coordinated silicon alkoxide is formed during hydrolysis, releasing $C_2H_5O^-$ which can subsequently form an alcohol and a hydroxide ion in an aqueous medium. Consecutive condensation of fully, partially, or unhydrolysed monomers results in the release of water or alcohol. Alcohols are known to affect zeolite crystallinity or even lead to different frameworks when using some ionic-liquid templates [89, 90], and are therefore often evaporated before crystallisation. However, this effect is beyond the scope of this thesis and thus the formed ethanol was kept as part of the synthesis mixture.

The extent and characteristics of the formed silica network depend on several factors including temperature, concentrations, pH, and

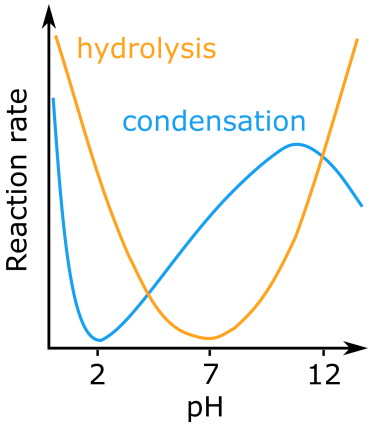

Figure 3.3: Reaction rates of the hydrolysis (orange curve) and condensation (blue curve) of TEOS as a function of pH. At pH > 12, rapid hydrolysis leads to depolymerisation and silica network collapse [92].

the presence of other metals or nucleophilic catalysts like fluoride (F^-) [91]. Figure 3.3 shows the influence of pH on the reaction rates of the hydrolysis and condensation of TEOS, displaying the high hydrolysis rate at low pH (pH=2) and high condensation rate at high pH (pH=11).

In this work, initial hydrolysis (and partial condensation) was performed at low pH, after which the pH was raised to basic conditions by adding NaOH to increase the rate of condensation, as well as provide the basic conditions necessary to promote crystallisation. The hydroxide ions are mineralising agents that enable the formation of hydroxidic or oxidic species of Si, Al and Ga, allowing for their dissolution and transport to the zeolite nuclei during crystallisation [93]. This enables the Al and Ga to isomorphously substitute Si in the framework position of the zeolite. Moreover, the now negatively charged precursor species coordinate around the positively charged SDA, e.g., TPA^+ cations [94].

In this thesis, the catalysts of set 1 were synthesised by first adding a dilute oxalic acid solution during the hydrolysis of TEOS (pH=2), followed by the addition of a concentrated NaOH solution (pH=12) to accelerate condensation. The addition of oxalic acid was initially developed to prevent precipitation of iron hydroxide species in other work [80] and was therefore omitted in later syntheses of catalyst sets 2 and 3. The acidic gallium precursor was sufficient to promote rapid hydrolysis.

3.2 Reaction set-up

The conversion reaction of 2,5-dimethylfuran to aromatics was performed and studied in a flow reactor, as shown in figure 3.4.

First, the catalyst powder was pressed into a pellet (5 tonnes, 1 min) using a manual hydraulic press (Specac). Then the pellet was crushed with a mortar and pestle and sieved to a fraction between 300 to 355 µm or 355 to 450 µm to promote gas flow and prevent a pressure drop. Between 50 and 100 mg of sample was loaded in a quartz glass tube (ID = 4 mm) and held in place by 50 mg glass fibre (silanized, VWR) on each side. The tube was surrounded by a metal coil and rock wool insulation for resistive heating. Two K-type thermocouples were inserted to measure the temperature: one in front of the catalyst bed to control the heating using a PID regulator (Eurotherm, Worthing, UK), and the other inside the catalyst bed to measure the actual, local temperature.

Heating of the connecting tubes was also regulated by thermocouples and set to a temperature of 191 °C to prevent condensation

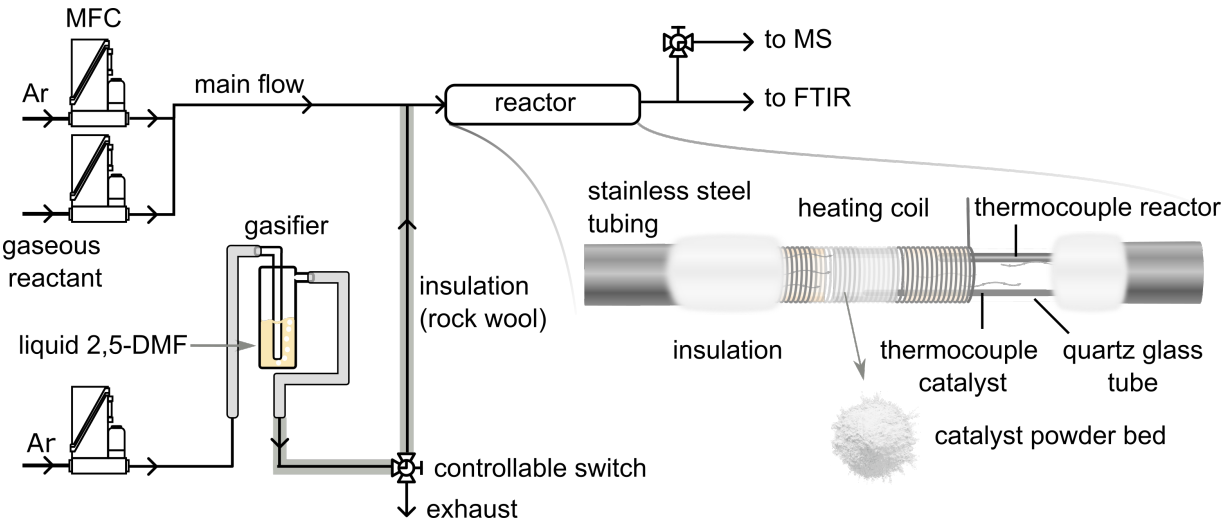

Figure 3.4: Schematic overview of the flow reactor set-up used in the catalytic study of 2,5-DMF into aromatics at high temperatures. The quartz tube is actually oriented vertically to promote equal flow over the catalyst bed. Adapted from [95].

in the lines. Inlet of gas was controlled via mass flow controllers (MFC, Bronkhorst Hi-TECH, Low-ΔΔ-flow), and gases used include argon (100 %), oxygen (100 %), and ammonia (4 % in Ar). The carrier gas argon was flown through a glass bubbler (Sigma Aldrich, 4 mL) which was filled halfway with liquid 2,5-DMF (Apollo scientific, 99 %) at room temperature, resulting in a saturated 2,5-DMF stream which was further diluted with Ar down to 300 to 1000 ppm [96].

Control of the MFCs and reactor temperatures was automated by Labview, and reactions were typically performed in 300 mL/min Ar flow (300 to 600 ppm 2,5-DMF) for 1 h up to 10 h. The reaction was performed at temperatures ranging from 200 to 600 °C but commonly at 500 °C. Before reaction, the catalyst was heated to 550 °C (20 °C min^{-1}) in 20% oxygen to remove any adsorbed species such as water. During the reaction, carbonaceous species (coke) are formed and deposited on the catalyst's surface. Therefore, the catalyst was reactivated after the reaction in 20 % O_2 (625 °C, 1 to 2 h). The effluent product stream was analysed and products were quantified using online ion-molecule-reaction mass spectrometry (IMR-MS) and Fourier transform infrared (FTIR) spectroscopy.

3.2.1 Mass spectrometry

Mass spectrometry (MS) is a useful tool to analyse complex streams and mixtures of gases. In conventional electron impact (EI) MS, an ionisation source such as an electron beam hits the analytes and this leads to dissociative ionisation by forming a radical cation (equation 3.1). This further fragments by elimination of a neutral radical (equation 3.2) or a molecule (equation 3.3), resulting in

$$M + e \longrightarrow M^{\bullet +} + 2e \quad (3.1)$$

$$M^{\bullet +} \longrightarrow A^{+} + B^{\bullet} \quad (3.2)$$

$$M^{\bullet +} \longrightarrow C^{\bullet +} + D \quad (3.3)$$

$$M + G^+ \longrightarrow M^+ + G \quad (3.4)$$

complex fragmentation patterns which are hard to deconvolute when dealing with a stream of many different analytes. One method to solve this issue is by using softer ionisation sources of lower energy, which is done in IMR-MS [97–99]. Primary atomic gases, such as xenon and mercury, are ionised by EI in a separate chamber, and subsequently directed onto the gas mixture (table 3.3). This leads to ionisation of the intact molecule and minimal fragmentation of the analytes, as shown in equation 3.4, allowing for quantitative measurements of e.g., benzene and toluene, of which the latter would fragment into benzene$^+$ when using EI.

Table 3.3: Ionisation potentials of different gases used in IMR-MS compared to electron impact (EI) ionisation [95].

Ioniser	ion. potential/eV
EI	70
Kr	14.00
Xe	12.12
Hg	10.44

Here, a quadrupole IMR-MS has been used (Airsense Compact, V&F) using EI, Hg (10.44 eV) and Xe (12.12 eV) as ionisation sources. Software version V&F analyser 1.4 was used and the method was previously developed by Sauer et al. [96]. An overview of the used m/z values, in which m=mass and z=charge of the fragment, is given in Appendix table A.3.

3.2.2 Fourier-transform infrared spectroscopy

Besides IMR-MS, another valuable technique to analyse the product stream makes use of FTIR spectroscopy. When a sample is illuminated with infrared (IR) radiation, some radiation is absorbed, and some is transmitted. If the frequency is equal to the vibrational frequency of the bonds in a molecule, the molecule can absorb the IR and start vibrating, stretching, bending, and more (figure 3.5).

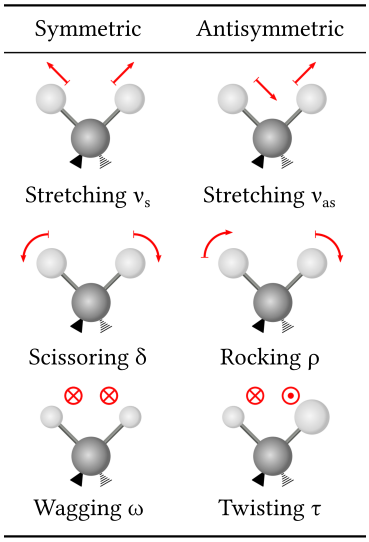

Figure 3.5: Schematic of vibrational modes for $-CH_2$ part in CH_2R_2 molecule. Adapted from [95].

Each specific bond or functional group in a molecule absorbs IR of a different frequency, resulting in a spectrum that functions as a molecular fingerprint of each compound [100]. However, not all species can be measured with IR, as the molecule will not absorb IR if it does not undergo a net change in dipole moment during vibration or rotation [101]. A full description of FTIR is provided in literature [50, 100, 101].

Here, the product, gas stream was analysed using an FTIR gas analyzer (MKS MultiGas 2030) operating at 191 °C. IR spectra were recorded every 3.75 s (4 scans) or 15 s (16 scans) between 4000 cm^{-1} to 600 cm^{-1} with a resolution of 0.5 cm^{-1}. Analysis was performed with MKS software suite MF2000 v.10.2 and FTIR-library v.R3, and a background spectrum was taken in Ar before measurements. The quantification of the different compounds was performed according to a method previously developed by Sauer et al. [96].

In short, the IR spectra of the complex, hydrocarbon product stream are compared to IR spectra of pure compounds, either from the FTIR library or from in-house calibrations. According to the

Beer-Lambert law, equation 3.5, the absorption of IR is linearly correlated to the concentration of the compound, which can be used to calculate the concentrations of the different compounds. Subsequently, the concentrations are used to calculate the carbon balance, conversion, and selectivity (see Appendix).

$$A = \epsilon l c \tag{3.5}$$

with A=absorbance, ϵ=molar absorptivity, l=optical path length c=concentration

Both detection techniques, FTIR and MS, complement one another in two ways: Firstly, more species can be detected since IR-inactive species are measured with MS, whereas FTIR is able to detect isomers that have the same m/z. Secondly, the robustness is increased as observed trends and concentrations can be confirmed by two methods. When comparing to other analysis techniques such as online gas chromatography (GC)-MS [46, 102], the used FTIR-MS set-up might have limitations in the number of species detected, since this depends on the available library and predetermined m/z values. However, similar carbon balances of around 90 % were found. One advantage of this technique is its high data acquisition, typically ranging from 15 min^{-1} to 4 min^{-1}, up to 1 spectrum per second;[10] much faster than once every few minutes in GC. An overview of the detected species and the settings used is shown in the Appendix, table A.3.

10: at the expense of a low signal-to-noise ratio (SNR)

3.3 Structural analysis

After synthesis of the catalyst, it is vital to perform a comprehensive structural analysis in order to understand and predict its catalytic performance. Below is a description of the techniques used in this thesis, the theory behind them and the used experimental parameters.

3.3.1 X-ray diffraction

One powerful method to study the catalyst structure is the use of X-ray diffraction (XRD). When a material is bombarded with X-rays, these incident X-rays undergo elastic scattering. Because they have wavelengths of molecular dimensions (Ångströms, Å), they can either be cancelled out due to destructive interference or amplified due to constructive interference. For crystalline materials, the coherent X-rays from ordered planes of atoms, result in diffraction at well-defined angles. The geometry of these diffraction events can be described using Bragg's law, equation 3.6 and figure 3.6 [103].

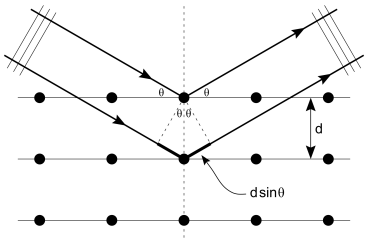

Figure 3.6: Schematic representation of Bragg's law [103], equation 3.6.

$$2dsin\theta = n\lambda \tag{3.6}$$

In which d = distance between two crystal planes, θ = diffraction angle (2θ is the angle between the incident and reflecting ray),

n = order of interference and λ = wavelength. The left-hand side of the equation is the path difference between two X-rays that undergo constructive interference and can be used to determine the crystal structure, including the unit cell parameters.

When plotting the angle between the incident and reflecting rays versus the intensity of scattered rays, peaks appear for angles corresponding to crystal lattice planes that show constructive interference, containing information in their position, size and shape. By comparing the peak positions to a database of well-known crystal structures, known crystalline phases present in the material, such as zeolite frameworks, can be identified. The intensity is mainly influenced by structure parameters such as crystal symmetry as well as the amount and absorption of the material, whereas the peak shape depends on lattice distortions caused by e.g., crystallite sizes. However, it must be noted that instrumental settings as well as experimental factors, such as sample preparation, can also influence peak position, intensity, and shape [104].

Other types of X-ray scattering techniques include single-crystal XRD (scXRD) and small-angle X-ray scattering (SAXS). scXRD measures discrete diffraction peaks of a single crystal, allowing for the determination of the atomic arrangement in unit cells which can be used to characterise new materials. SAXS measures diffraction of X-rays through a material and is not limited to crystalline, microscale materials. This allows for the measuring of scattering effects at very low angles which, according to equation 3.6, correspond to large crystalline spacing. Therefore, it provides the ability to measure mesopores, which are undetectable with powder XRD. Both techniques can offer valuable insights and will be explored in future research, but will not further be discussed in this thesis.

Here, powder XRD was measured on a Bruker AXS D8 Discover diffractometer with monochromatic Cu-Kα radiation (1.5406Å) from 5 to 50°. Sample holders include a plastic puck and a single silicon crystal background flat puck. Measurements were performed with a fixed sample illumination[11] or a fixed slit size.[12] Since the overall signal-to-noise ratio (SNR) was higher for fixed sample illumination, this was used for most XRD diffractograms. The air scatter knife was located 1 to 5 mm from the sample, with no rotation, increments of 0.01 to 0.02°, and acquisition times of 1 to 2 s were used. Diffractograms were plotted using DIFFRAC.EVA V6.0 software and normalised to their maximum intensity.

11: total illuminated area was held constant by varying the slit size, resulting in a low intensity at low incident 2θ angles as well as a low background signal.

12: total illuminated volume was held constant, resulting in a high intensity at low incident 2θ angles, as well as a high background signal.

3.3.2 X-ray fluorescence

To determine the elemental composition of the materials, another analysis technique involving X-rays was used, named X-ray fluorescence (XRF). In this technique, the material is bombarded with X-rays, exciting the atom by expelling an electron out of the inner shells. When this emission of an electron produces a vacancy in e.g., the innermost shell (K-shell), a higher-energy electron from the second or third shell (L- and M-shell) can fall back and take up the vacancy (figure 3.7). As the electrons in the outer shells are higher in energy, the difference in energy between the shells is released as an X-ray photon. Since each atom has distinct energies of its shells, the emitted X-rays are characteristic for the specific element and this can be used to quantify the elements present in the investigated material [104]. There are limitations to using XRF as lighter elements (atomic number < 18) emit fluorescent X-rays that are low in energy and cannot always penetrate and escape the sample matrix. Instead, the light elements are only measured at the sample surface whereas X-rays originating from heavier elements are measured from deeper within the sample. Adsorbed or occluded light-element species in the zeolite pores can not be measured but will influence the XRF measurement by absorbing and scattering X-ray radiation [105]. Therefore, samples must be dried before measuring.

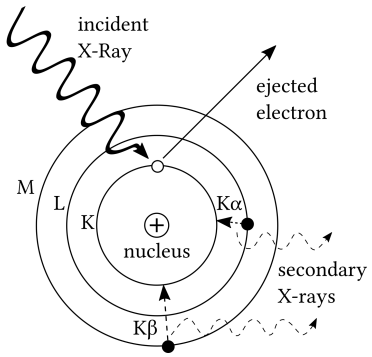

Figure 3.7: Primary mechanism of XRF in which an incident X-ray expels a core-shell electron. Afterwards, electrons from higher shells (L and M) fall back under emission of characteristic X-rays.

In this thesis, XRF was measured on a PANalytical AXIOS XRF spectrometer. Between 100 to 500 mg sample was prepared using a plastic sample cup holder and 6 µm polypropylene film (Chemplex Industries). The content of each element was quantified by comparison with a calibrated standard material, assuming elements to be present in their oxide form, and correcting for the water content (derived from TGA).

3.3.3 Physisorption

For microporous catalysts such as zeolites, it is crucial to investigate the textural properties including surface area, pore volume and pore size distribution. One method to study this involves nitrogen-physisorption, in which nitrogen physically adsorbs to the catalyst surface due to van der Waals attraction. The sample is cooled to cryogenic temperatures, 77 K (-196 °C) for N_2, after which nitrogen is dosed in a series of controlled pressures, leading to an increasing number of adsorbed molecules. After adsorption, the pressure is decreased causing the desorption of nitrogen, creating the full nitrogen-physisorption isotherm.

Analysis of the isotherms can be done using several different models and equations. One of the early models in 1916, the Langmuir adsorption model [106], assumes the adsorbed gas to behave ideally and each active site to be occupied by only one particle. Adsorption is independent of adsorption on neighbouring sites and continues until a monolayer is formed. In 1938, Brunauer, Emmett, and Teller (BET) extended this model to include adsorbate/adsorbate interactions, resulting in the adsorption of infinite layers [107, 108]. The BET-equation is used to determine the BET surface area from an adsorption isotherm and is shown in equation 3.7. [13]

$$\frac{p/p_0}{v(1-(p/p_0))} = \frac{c-1}{v_m c}\left(\frac{p}{p_0}\right) + \frac{1}{v_m c} \tag{3.7}$$

13: in which p and p_0 are the equilibrium and saturation pressure of the adsorbate, respectively; v = adsorbed gas quantity, v_m = monolayer adsorbed gas quantity, c = BET constant.

This equation is used to determine the quantity of the adsorbate needed to form a monolayer, which can then be used to determine the specific surface area (SSA), or rather the BET area, by selecting a linear region of the isotherm. To minimise erroneous use of the BET equation, Rouquerol et al. [109] have designed several criteria that guide researchers to select the correct range.[14]

14: Rouquerol critera:

- $v(1-(p/p_0))$ must increase continuously with p/p_0.
- The constant c must be positive.
- The p/p_0 value corresponding to v_m should be within the selected linear range.

Nonetheless, the use of the BET equation is still very limited, especially for materials that contain micropores, and care must be taken when evaluating isotherms [109–113]. Essentially, the monolayer is not formed homogeneously but micropore filling occurs first, resulting in an unreliable monolayer capacity v_m. Moreover, the structure of the monolayer is dependent on the surface properties [111, 114], and adsorbate molecules interact with multiple surfaces inside a micropore due to their molecular dimensions. For these reasons, the BET area does not signify an SSA but rather an apparent surface area, and should only be used for qualitative comparisons between samples within the same type of catalyst, like a fingerprint.

Besides surface area, the micropore volume of the catalyst was determined using the t-plot method. Here, the isotherm is compared to a reference sample which has a chemical composition and surface chemistry similar to the sample but is nonporous.

In this way, the average thickness of the adsorbed layer is plotted with the Harkins-Jura equation (3.8), which allows for the determination of the adsorbed volume on the micropores and the external surface [115–117]. Since it uses the BET area, and it does not take into account the increase of the size of the adsorbed layer when the pore size gets smaller,[15] it is also flawed in its use for microporous materials [119, 120].[16]

$$log\frac{p}{p_0} = B - \frac{A}{v^2} \tag{3.8}$$

with constants B and A

15: curvature effect derived with the Kelvin equation [118]

16: a corrected t-plot analysis for hierarchical materials that contain both micro- and mesopores has been developed and will be studied in future research [120, 121].

The most common adsorbate for physisorption studies is nitrogen, mainly because it is readily available and provides distinct isotherm

shapes for many materials [112]. However, due to its inherent quadrupole moment, the orientation of adsorbed nitrogen is dependent on the surface of the material and this can lead to uncertainties of up to 20 % in the molecular cross-sectional area occupied on the surface [122]. A superior alternative is argon [123], which does not have a quadrupole moment, is less reactive, and is less sensitive to the surface of the adsorbent material. Ideally, argon physisorption should be performed at its boiling point 87.3 K (−185.8 °C), which is roughly 4 K above its triple point of 83.7 K. Even though argon physisorption at 77 K, below its triple point, has appeared insightful for meso- and macroporous materials [124–127], their use for microporous materials is limited. At 77 K, the adsorbed argon molecules can re-sublimate[17] into the solid state when increasing the pressure, resulting in an incorrect calculation of their size and thus occupied area on the material [112, 128].

17: re-sublimation = deposition (from gas to solid)

In this thesis, nitrogen and argon sorption isotherms were measured on a Micrometrics Tristar 3000 instrument at 77 K (−196 °C). Pre-treatment of the sample was performed under nitrogen flow at 90 °C for 1 h followed by 250 °C for 16 h (10 °C/min). Specific surface areas were determined using the BET method by manually selecting the best pressure range that follows all Rouquerol criteria, often between $p/p_0 = 0.002 - 0.03$. Microporous volume and external surface areas have been determined using the t-plot method, choosing a thickness range after micropore filling was complete, as suggested by Galarneau et al. [120]. The thickness ranges used are 3.5 to 5.0 Å or 5.0 to 8.0 Å.

3.3.4 Scanning electron microscopy and energy dispersive X-Ray analysis

The crystalline catalysts can also be studied and visualised by scanning electron microscopy (SEM) to obtain information on the size, shape and morphology of the crystals. Here, an electron beam is focused onto the sample surface, resulting in elastic and inelastic scattering of electrons from the material (figure 3.8). The inelastically scattered, secondary electrons are detected and form a grey-scale image of the surface topography.

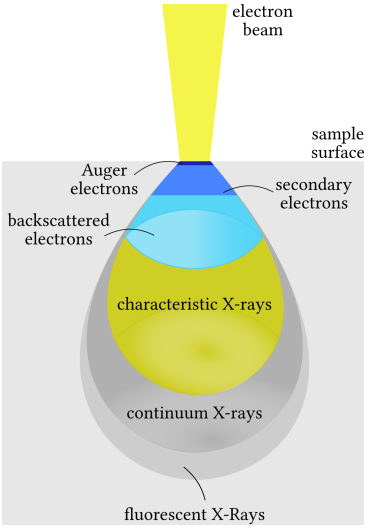

Figure 3.8: Schematic overview of the interaction volume of SEM.

Simultaneously, the elemental composition can be determined by measuring energy-dispersive X-ray spectroscopy (EDX). As shown in figure 3.8, besides electrons, X-rays are also emitted upon excitation with an electron beam. Similar to XRF, element-specific X-rays may be detected allowing for analysis of the spatial elemental distribution throughout the particle.[18]

18: both SEM and EDX may suffer from selection bias through manual selection of particles.

In SEM, the sample needs to be conductive to prevent a buildup of electrons that could lead to charging effects, which reduce both

image quality and resolution. Non-conductive materials can be covered in a few nanometers of conductive material like gold, to ensure successful imaging while still maintaining the high resolution of SEM (up to 10 nm).

In this thesis, SEM images were taken under vacuum ($1.2{\cdot}10^{-5}$ mbar) with a LEO Ultra 55 FEG SEM using an accelerating voltage of 1 kV. For EDX analysis, SEM images were taken under vacuum on a FEI Quanta 200 FEG ESEM using an accelerating voltage of 20 kV, equipped with an Oxford Inca EDX. Powder samples were loaded on conductive carbon tape stuck to an aluminium sample holder. For SEM measurements, coating was optional but for EDX analysis, samples were coated with 1.67 nm to 4 nm Au with a Leica EM ACE600 sputter coater ($3.4{\cdot}10^{-5}$ mbar).

3.3.5 Thermogravimetric analysis and differential scanning calorimetry

Testing the thermal stability of the catalyst is a crucial step that is taken during synthesis of the catalyst to improve e.g., calcination steps, and before designing reactor tests that involve high temperatures. Thermogravimetric analysis (TGA) coupled with differential scanning calorimetry (DSC) measures the thermal stability and simultaneously detects volatile or organic materials that are adsorbed or present in the pores of the catalyst.

First, a small amount of the sample is placed into an inert crucible after which this is placed on a balance in a furnace. The sample is then slowly heated under a controlled gas flow, commonly air or nitrogen, resulting in the loss of weight due to desorption or decomposition of volatile species. By comparing to an empty reference crucible, heat changes can be observed and endothermic processes, like desorption, and exothermic processes, like the oxidation of organic compounds, can be observed.

Here, TGA/DSC was carried out on a Mettler Toledo TGA/DSC 3+ STARe system over a range of 30 °C to 800 °C (10 °C/min) in 60 mL/min air flow. Alumina crucibles (70 µl) were filled with 10-20 mg sample and after measurements, they were cleaned in concentrated nitric acid (69 %, Merck) for 6 h followed by rinsing with demineralised water and ethanol and dried in an oven (80 °C).

3.3.6 NH_3-temperature programmed desorption

The acidity of a catalyst is a crucial characteristic involved in its catalytic performance and must be measured before and after the reaction to understand which acid sites have played a role in the reaction. Acidity encompasses both the strength of the acid site, as well as the number of acid sites.

One way to measure the acidity is by probing with a basic molecule that can bind to an acid site, and subsequently desorb when conditions such as the temperature are changed. A common probe molecule is ammonia, NH_3, which is able to bind to both Lewis and Brønsted acid sites. In Brønsted acid sites it can either coordinate to the BAS through hydrogen bonding[19] or through proton transfer.[20] The NH_4^+ vibration can be measured with diffuse reflectance infrared Fourier transform spectroscopy (DRIFTS) or solid-state nuclear magnetic resonance (ssNMR) [129, 130], or ammonia can be desorbed and measured with MS [131], FTIR [132–134], and gas chromatography sensors such as a thermal conductivity detector (TCD) [135] or flame ionisation detector (FID) [136]. The binding to Lewis acid sites results in more complex interaction due to the different types of LAS ([137]). The advantages of NH_3 are that it is cheap, binds to all acid sites, and is able to access micropores due to its small kinetic diameter (2.6 Å) [138, 139]. Disadvantages include its inability to distinguish BAS from LAS, especially since linking acid site strength to specific sites is complex, or its stickiness to reactor set-ups such as stainless-steel tubing, and its ability to readsorb to the catalyst on different acid sites after desorption [140].

19: $ZOH\cdots NH_3$ with Z=zeolite

20: $ZO^- - NH_4^+$

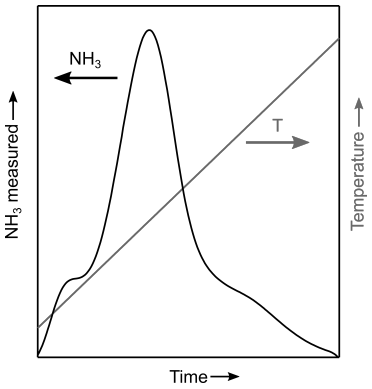

Figure 3.9: Schematic example of an NH_3-TPD profile in which a linear ramp in temperature (grey, right axis) results in desorption and detection of NH_3 (black, left axis) over time.

In this thesis, ammonia TPD was performed in the flow reactor set-up before and after catalytic testing. The catalyst was first pretreated in 20 % O_2 in Ar at 550 °C for 30 min to 1 h (20 °C/min) to remove adsorbed species such as water. Then, the acid sites were saturated with 200 ppm to 400 ppm NH_3 in Ar for 30 min to 1 h at in 100 °C. This was followed by purging with Ar for 1.5 h to 2 h to remove the weakly bound physisorbed ammonia from the catalyst surface (total flow of 300 mL/min). This was followed by a temperature ramp to 600 °C (10 °C/min),[21] leading to the release of ammonia when the bonds are broken: the stronger the acid site, the higher the temperature of desorption. Ammonia concentrations were determined by FTIR and converted into the acid site density (mmol / g catalyst).

21: 550 °C was used at first but this was too low to desorb all ammonia. 5 °C/min and 20 °C/min were also explored but 10 °C/min was optimal.

Efforts have been made to minimise the drawbacks of NH_3-TPD, mentioned above, including operating at a high flow rate to minimise diffusion and readsorption, as well as decrease the ammonia concentrations to reduce the effect of sticky NH_3 lagging in the system.

Results and discussion 4

This section describes the structural characterisation of the studied catalysts followed by the analysis of their catalytic performance in the conversion of 2,5-dimethylfuran into aromatics. First, set 1 will be discussed which investigates the influence of the incorporated metal in MFI-framework zeolite, as shown in more detail in Paper I [134]. The influence of temperature and the conversion of 2,5-DMF into 2,4-DMF will be discussed (Paper II). Afterwards, sets 2 and 3 will investigate the influence of the gallium content. This is followed by set 4, exploring the influence of mesopores.

4.1 Influence metals 29
4.1.1 Structural analysis . . . 29
4.1.2 Catalytic tests 33
4.2 Influence temperature 39
4.3 Influence gallium content 42
4.3.1 Structural analysis . . . 42
4.3.2 Limit gallium content . 48
4.3.3 Catalytic tests 52
4.4 Influence mesopores . 56
4.4.1 Catalytic tests 58

4.1 Influence of incorporated metals

In set 1, acidity has been introduced by isomorphously substituting silicon with aluminium or gallium. A siliceous zeolite, Si-MFI, is compared with two aluminium-containing MFI catalysts (Al-MFI) and one gallium-containing catalyst (Ga-MFI).

4.1.1 Structural analysis

XRF

To study the effect and extent of gallium and aluminium incorporation, elemental analysis has been performed using XRF. The chemical compositions of the catalysts are shown in Table 4.1 which were used to determine the Si/M ratios, as well as identify the presence of any impurities (residual).

Sample	Ga	Al	Si	O	Na	H_2O	Residual
				/wt%			
Si_∞	0	0	45.9	53.6	0.31	0.88	0.1 *
Ga_{33}	3.2	0.04	43.5	52.9	0	0.27	0.01†
Al_{41}	0	1.0	44.2	54.3	0	3.4	0
Al_{11}	0	3.5	39.3	56.1	0	7.2	0.09‡

* K
† Ca
‡ Fe, S, Ti, Zr

Table 4.1: XRF Elemental analysis of set 1. Oxygen wt% is derived by assuming metals to be present as oxides. H_2O determined by TGA at 200 °C. Normalised to a total weight percentage of 100 wt%.

Light elements such as carbon and hydrogen cannot be measured and must be added manually. For example, water has been manually added to the calculation and the water content was determined by TGA by using the sample weight at 200 °C. All catalysts consist

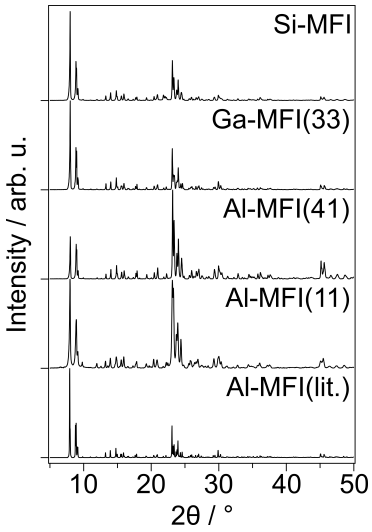

Figure 4.1: XRD patterns of set 1 catalysts. A calculated XRD pattern of Al-MFI from literature is shown (Al-MFI (lit.)) for reference, assuming pseudo-Voigt peak shapes [61, 141]. Background subtracted, normalised to the highest intensity, and vertically displaced for clarity.

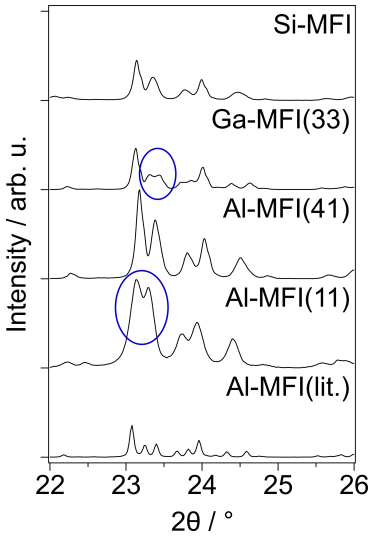

Figure 4.2: Close-up of XRD patterns of set 1 catalysts from figure 4.1.

mainly of silicon and oxygen, and their respective incorporated metal, Al or Ga. The commercial Al-MFI(11) catalyst contains the most impurities and Ga-MFI(33) contains some aluminium, possibly originating from the gallium precursor or aluminium foil used in handling the catalyst.

XRD

To confirm the successful synthesis of crystalline zeolites and identify the framework structure of the catalysts, XRD has been measured, and the patterns are shown in figure 4.1. All samples exhibit diffraction peaks associated with the crystal lattice planes that are characteristic of the MFI framework structure: a calculated Al-MFI pattern from literature is shown as reference [61, 141].The absence of other peaks indicates that no other crystalline phases of long-range order, like Ga_2O_3, have formed. Although some differences in peak shapes, such as their sharpness, can be seen. Peak broadening and overlap can be observed for Al-MFI(11), around 8.9°, 23.3°, and 23.8°, and for Ga-MFI(33) around 23.3°and 23.8°, shown in figure 4.2. This indicates the presence of crystal lattice imperfections such as defects, or the presence of nanosized crystallites [142]. Peaks of Al-MFI(41) are located at slightly higher angles which is caused by a difference in sample bed height, due to different sample holders. Future calibrations using known compounds, such as alumina, can be used to correct this systematic error.

Defects are places of the zeolite crystal lattice where the repeating structure is disrupted, e.g., where the Si−O−Si bond is changed to an internal silanol Si−OH group [143]. This can be caused by many factors including microstrain, stacking faults, and dislocations, which can all be caused by the substitution of a framework silicon atom by a larger gallium atom. Previous studies have shown that incorporation of gallium into the MFI framework is found to be disruptive since it leads to a greater lattice distortion [144]. The influence of the gallium content will be further explored in section 4.3.

Physisorption: N_2

The porosity of the catalysts plays an important role in the mass transport of reagents and products, as well as in the density of active sites for reactions. Analysing the textural properties such as specific surface area and pore volume, allows for studying the influence of the substituted metal. The N_2-isotherms of set 1 are shown in figure 4.3.

All zeolites show a steep N_2-uptake at low relative pressures (p/p_0 < 0.01), indicating the filling of micropores. This happens due to the interacting forces between N_2 and the surface in narrow micropores of molecular dimensions [112]. The shape of the isotherms can be considered a composite of type I and type IV [112]. Type I is associated with microporous adsorbents and nitrogen uptake reaches a plateau after initial micropore filling, due to the limited micropore access. Type IV is associated with adsorbents containing large micro- or mesopores which can be present within crystals or between zeolite crystals.

The isotherm of Si-MFI displays a remarkable second uptake step at p/p_0=0.2. This step can be attributed to the non-inert N_2-molecules, which undergo reorientation to permit a more favourable quadrupole-quadrupole interaction [62, 114, 145]. Subsequently, when nitrogen molecules desorb, they undergo the reverse reorientation leading to a hysteresis step [122]. This phase transition of nitrogen is associated with the formation of a solid-like dense structure which means that the zeolites channels and intersections can be occupied by more N_2-molecules. This is not seen for Ga-MFI and the Al-MFI catalysts, due to the preferential adsorption of nitrogen to the gallium and aluminium sites. Therefore, initial adsorption does not result in a disordered mobile phase but instead already involves a localised state (lattice fluid-like phase) which slowly transitions into the denser solid-like phase [146].

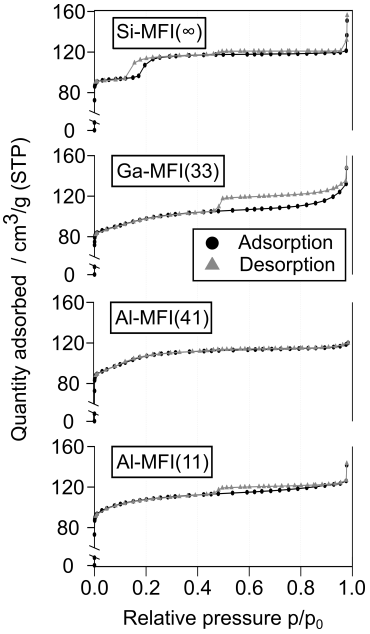

Figure 4.3: N_2-physisorption isotherms at 77K of the catalyst set 1. Nitrogen adsorption (circles, black) and desorption (triangles, grey).

Sample	SA* / $m^2\ g^{-1}$	$S^{\dagger}_{micro}$ / $m^2\ g^{-1}$	$S^{\dagger}_{ext}$ / $m^2\ g^{-1}$	$V^{\dagger}_{micro}$ / $m^3\ g^{-1}$
Si_{∞}	395	386	9	0.175
Ga_{33}	365	338	27	0.145
Al_{41}	390	374	16	0.164
Al_{11}	412	386	26	0.158

Table 4.2: Textural properties of catalyst set 1, derived from nitrogen isotherms. Samples are named after their Si/M ratio with M=metal incorporated.

* Apparent surface areas by BET method, p/p_0 = 0.002-0.03 for Si-MFI and p/p_0 = 0.002-0.05 for other catalysts, following consistency criteria [109]
† by t-plot method (Harkins and Jura equation, t= 5.0 - 8.0 Å)

Besides Al-MFI(41),[1] all isotherms display hysteresis loops of type H1 and H4 between p/p_0=0.5 and p/p_0=1.0, associated with capillary condensation. Type H1 is associated with materials possessing uniform mesopores or ink-bottle pore shapes, whereas type H4 is associated with zeolites containing micro- and mesopores. This combination suggests that the samples possess mesopores in between zeolite crystal aggregates [112].

An overview of the apparent surface area and microporous volume of catalysts from set 1 is shown in table 4.2. Both catalysts with aluminium and the catalyst with gallium possess high apparent surface areas, microporous areas, and microporous volume, similar to pure siliceous Si-MFI.

1: the absence of hysteresis suggests reversible adsorption and desorption of nitrogen in the micropores, supporting its type I isotherm character.

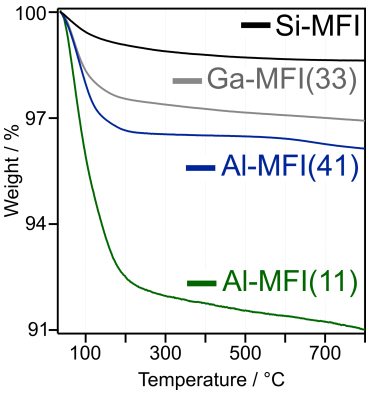

Figure 4.4: TGA profiles set 1 from 30 to to 800 °C in 60 mL min^{-1} air (10 °C min^{-1}).

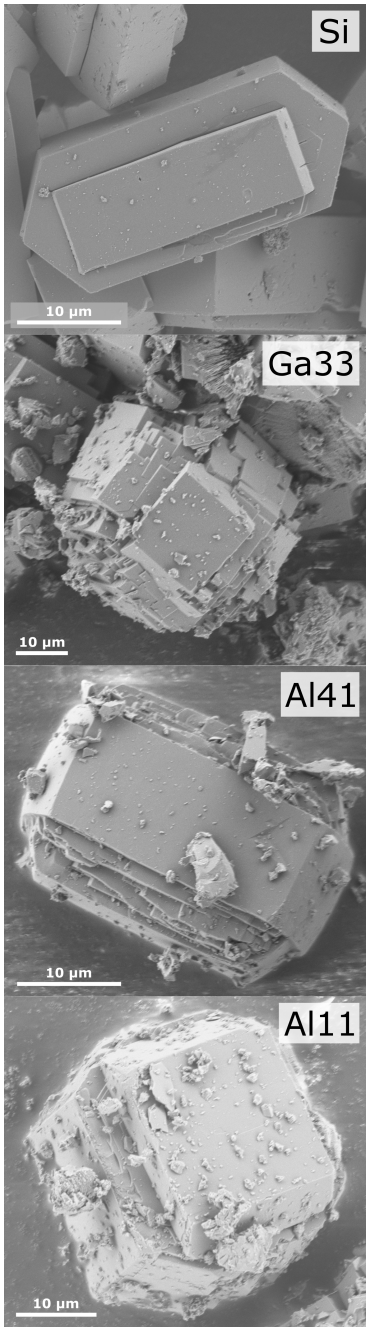

Figure 4.5: SEM images of catalyst set 1, taken with an SE2 detector at an accelerating voltage of 1.5 kV.

TGA

The thermal stability of catalyst set 1 has been tested by performing TGA in air, shown in figure 4.4. The total weight losses of 1.2 %, 3.3 %, 4.0 %, and 8.7 % for Si-MFI, Ga-MFI(33), Al-MFI(41), and Al-MFI(11), respectively, indicate high thermal stability for all samples over this temperature range. Most of the weight loss occurred between 50 °C and 200 °C, indicating the loss of water adsorbed from the air [147]. This weight loss appears to increase with the content of the substituted metal in the catalysts, suggesting a contribution of the Si(OH)–M groups, with M=Al or Ga, to the adsorption of water [147].

SEM

Visualising the crystalline catalysts with SEM provides information on their size, shape, and regularity or homogeneousity.

Figure 4.5 shows the SEM images of selected catalyst particles, displaying the morphological features and confirming their crystallinity. Si-MFI and Al-MFI(41) are coffin-shaped whereas Al-MFI(11) contains both coffin-shaped and cubic-shaped crystals. Ga-MFI(33) crystals are cubic-shaped and have formed larger, connected intergrowths, suggesting the presence of mesopores [148]. In all samples, irregular structures were identified on the external facets, suggesting the presence of impurities or the potential migration of Al or Ga species during calcination [148]. In previous work, it was concluded that Ga was still inside the framework of Ga-silicate using DRIFTS [148]. The vibration at 3616 cm^{-1} confirms the presence of Brønsted acid sites caused by the OH stretch vibration in the –Ga–O(H)–Si– species. Compared to Al-MFI (ZSM-5) the vibration is shifted from 3610 cm^{-1} to higher wavenumbers confirming the weaker Brønsted acid strength of the Ga sample [80, 149].

Take-home message
Silicon in MFI-framework zeolite can successfully be substituted by metals such as aluminium and gallium. The MFI framework, porosity, and thermal stability are preserved and crystalline particles are formed.

4.1.2 Catalytic tests

After structural analysis, the catalytic performance of the zeolites was tested in the conversion of 2,5-dimethylfuran to aromatics. FTIR and MS were measured in an on-line flow reactor and the product concentrations, selectivities, and conversions were calculated.

Figure 4.7 displays the conversion of 2,5-DMF over Ga-MFI(33) as well as the selectivities of the seven main products, including aromatics, olefins, and isomers of 2,5-DMF, over a period of 10 h at 500 °C, of which the first 2 h are enlarged. Besides the seven main products shown in figure 4.6, 13 other compounds, such as para-xylene, are measured in low concentrations, only a few ppm, resulting in a low signal-to-noise ratio (SNR). Therefore, they are omitted from figure 4.7 and further analysis.

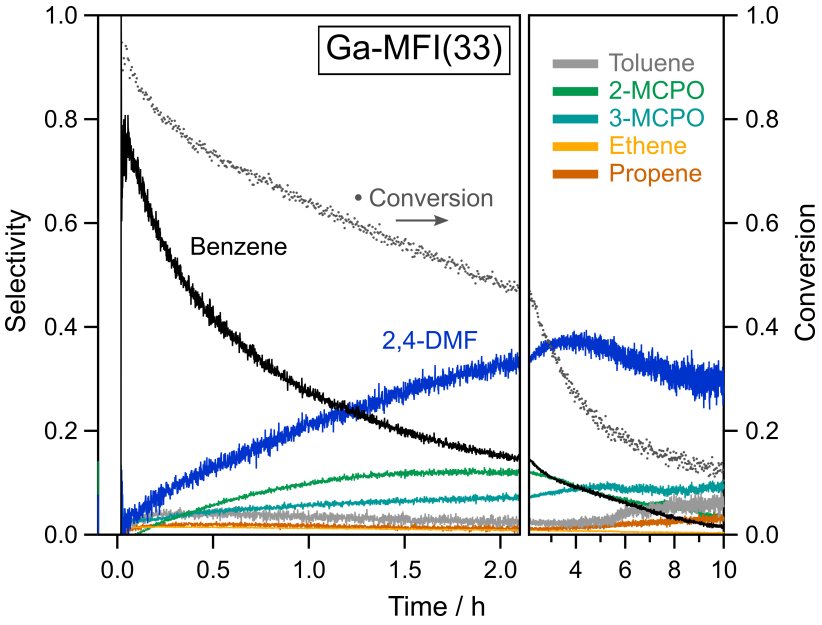

At the start of the reaction, 2,5-DMF is fully converted into mainly benzene, with an initial selectivity of roughly 75 %. After 5 h, benzene selectivity drops to 10 % down to 2 % after 10 h. Remarkably, selectivity has shifted towards isomers such as 2,4-DMF, 2-MCPO and 3-MCPO with increasing time-on-stream (TOS). Their production is still notable after 10 h of TOS.

To compare, similar experiments have been performed using Al-containing zeolites, shown in figure 4.8. Si-MFI is not shown due to its low conversion.

Al-MFI(41) demonstrates a high initial conversion with an initial benzene selectivity of 44 % that gradually decreases to 5 % after 100 min and to 0 % after 3.5 h, while toluene selectivity decreases from 14 % to 5 % after 80 min.

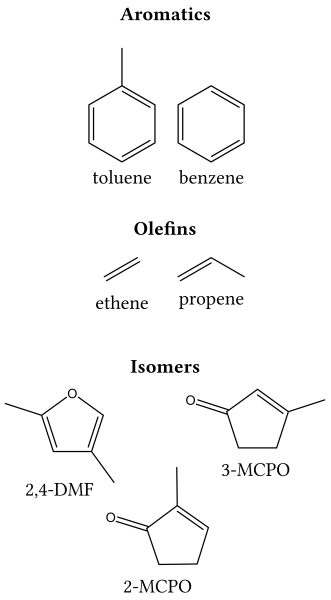

Figure 4.6: (upper figure) Molecular formulas of the main products measured with FTIR-MS, including the isomers 2,4-dimethylfuran (2,4-DMF), 2-methyl-2-cyclopentenone (2-MCPO), and 3-methyl-2-cyclopentenone (3-MCPO).

Figure 4.7: (left figure)Conversion of 2,5-DMF and selectivities towards the main products during a 10 h conversion reaction of 600 ppm 2,5-dimethylfuran at 500 °C. Selectivities from 2 h to 10 h (right pane) are smoothed for clarity (binomial, bounce, factor 20).

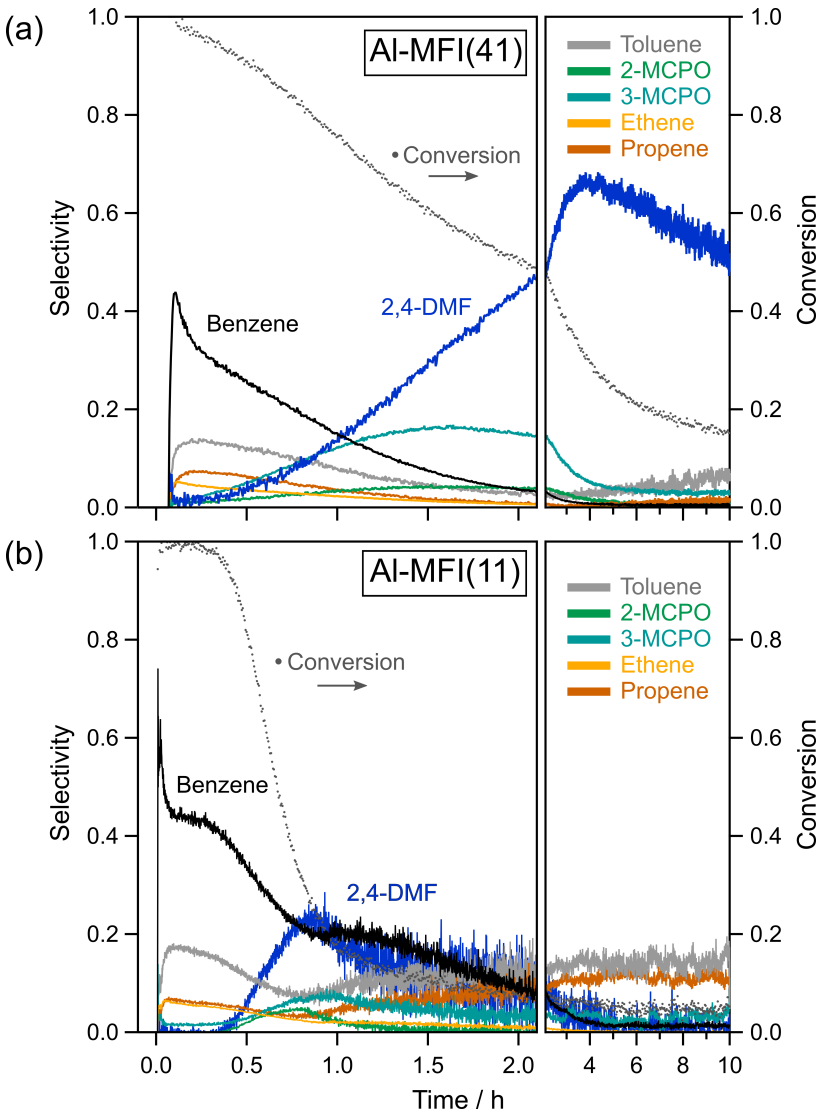

Figure 4.8: Conversion of 2,5-DMF over Al-MFI(41) (a) and Al-MFI(11) (b) and selectivities towards the main products over Ga-MFI(33) during a 10 h conversion reaction of 600 ppm 2,5-DMF at 500 °C. Selectivities from 2 h to 10 h over Al-MFI(11) (b, right pane) are smoothed for clarity (binomial, bounce, factor 20).

Ga-MFI(33) demonstrated minimal conversion to toluene with only max. 4 %, but it has a superior production of benzene, as well as a superior catalyst lifetime towards the production of aromatics. With increasing TOS, the selectivity over Al-MFI(41) shifts from aromatics to isomers, as was seen for Ga-MFI(33). The main product becomes 2,4-DMF, reaching a maximum selectivity of 68 % after 3.75 h and a final selectivity of 50 % after 10 h.

When the amount of incorporated aluminium is increased, like in Al-MFI(11), 2,5-DMF conversion follows a somewhat similar pattern (4.8, b). First, 2,5-DMF is converted with 100 % conversion into benzene (58 %) and toluene (17 %), after which the selectivities shift towards 2,4-DMF, 2-MCPO, and 3-MCPO after 45 min. In contrast to the other two catalysts, Al-MFI(11) rapidly deactivates and only displays 16 % conversion and 20 % benzene selectively after 1 hour, down to 5 % conversion and 4 % benzene selectivity after 3 h. Catalyst deactivation can be caused by the coking of the active sites and the microporous structure, due to further reactions

of monoaromatics into bulkier polyaromatics or graphite. Because of the increased aluminium content, its acidity is also increased which results in the continued conversion of monoaromatics before they leave the catalyst framework. When comparing Al-MFI(11) with Al-MFI(41), it becomes evident that the lifetime of the catalyst can be increased by reducing the aluminium content. Moreover, incorporating gallium instead of aluminium also seems to reduce catalyst deactivation and thus increase the catalyst's lifetime, even though similar or higher amounts of aromatics are produced. Further analysis of the acid sites can confirm these postulations and explore the influence of acidity.

The lifetime and stability of Ga-MFI(33) were tested by performing 4 more cycles of conversion (not shown).[2] During these four cycles, initial conversion remained 100 %, final conversion dropped by 4 % and the benzene selectivity also dropped by 4 %, confirming that Ga-MFI(33) can be readily regenerated and remains active after several cycles for 2,5-DMF conversion.[3]

Unfortunately, the selectivities shown in figures 4.7 and 4.8 do not account for the coke that is formed on the catalyst surface, and should therefore be slightly lower. The amount of coke cannot be determined until after the reaction, when a temperature-programmed oxidation (TPO) is performed.[4] As a result, the coke decomposes into CO and CO_2 which is quantified with FTIR. Typically, catalysts collect between 5 and 10 % carbon equivalents[5] as coke after 10 h.

The total amount of aromatics produced is measured with MS and shown in table 4.3. The observed signals support the observations from FTIR that Ga-MFI(33) demonstrates superior production of aromatics.

Take-home message
Aromatisation of 2,5-DMF occurs in both aluminium and gallium-containing MFI-catalysts, mainly to benzene, in the order of Ga-MFI(33)>Al-MFI(11)>Al-MFI(41). Selectivity shifts towards isomerisation products such as 2,4-DMF with increasing TOS, and Ga-MFI(33) demonstrates the highest lifetime towards aromatic production.

2: 2 h at 500 °C with oxidation in between (1 h at 608 °C in 20 % O_2)

3: conversion from 43 % after 2 h in cycle 1 down to 39 % in cycle 4. Initial benzene selectivity from 63 to 59 % and final selectivity from 7 to 5 %

4: 1 to 2 h at elevated temperatures up to 625 °C in 20 % oxygen

5: 1 molecule of 2,5-DMF (6 carbons) is equivalent to 6 molecules of CO or CO_2 (1 carbon).

Table 4.3: Total BTX production for catalyst set 1 over 10 h, detected by MS (counts) and normalised to the amount of catalyst.

Ga-MFI(33)	10^6 counts/ gram cat.
benzene	41094
toluene	589
xylenes	24
Al-MFI(41)	
benzene	4887
toluene	531
xylenes	26
Al-MFI(11)	
benzene	19587
toluene	760
xylenes	9

NH_3-TPD

Besides structural analysis of the catalysts, it is also essential to acquire knowledge about the active sites, which is in this case, the acid sites. Therefore, NH_3-TPD has been measured in a flow reactor, before and after the reaction.

Figure 4.9 shows an overview of the ammonia desorption profiles during two subsequent NH_3-TPDs before the reaction, and one directly after 10 h conversion of 2,5-DMF at 500 °C. The two initial TPDs were performed to measure the reproducibility of the procedure, as well as detect any changes in acidity induced by the TPD itself. For Si-MFI and Al-MFI(41), both TPD profiles of

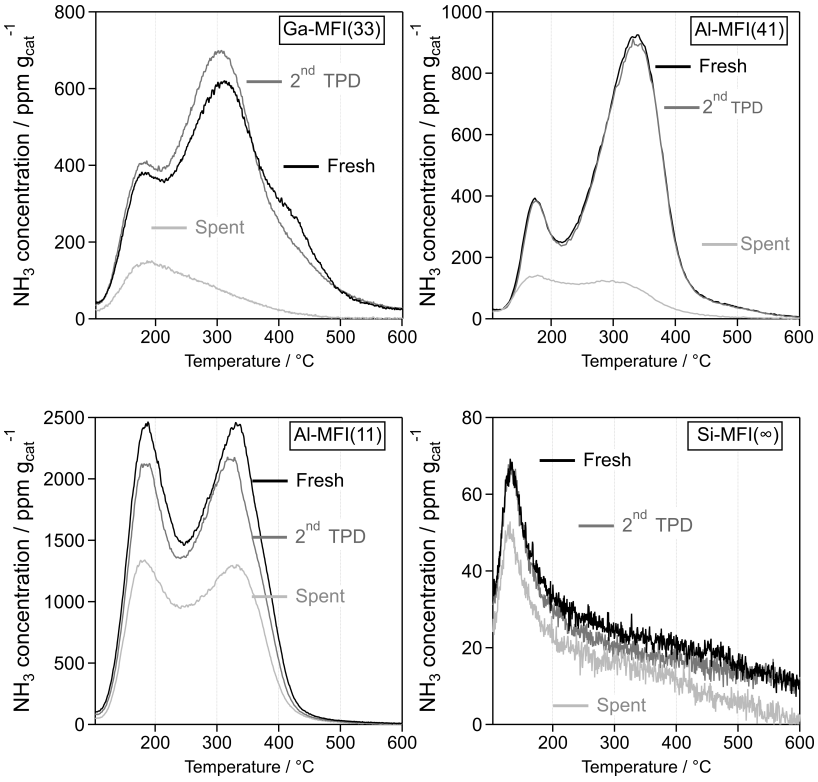

Figure 4.9: NH_3-TPD profiles of set 1 catalysts before the reaction (fresh, black), followed by a 2nd ammonia-TPD (dark grey), and a third ammonia-TPD of spent catalyst after the reaction (light grey). After saturating the catalyst with ammonia and purging with Ar at 100 °C temperature was raised to 600 °C (10 °C/min). Ammonia signal is normalised to the amount of catalyst.

the fresh catalyst are similar, but for Al-MFI(11) and Ga-MFI(33), some changes are visible. In Al-MFI(11), less ammonia is desorbed during the 2nd NH_3-TPD, indicating the availability of fewer acid sites, suggesting that the heat treatment to 600 °C resulted in the loss of acid sites.[6] This can be caused by metal migration or the formation of nanoparticles and clusters.

The 2nd TPD profile of Ga-MFI(33) has a different shape than its 1st TPD: the contribution of the high-temperature peak, which is associated with strong acid sites, has decreased. Si-MFI possesses some weak acid sites even though there are no metals introduced in the framework. These sites can be induced by defects resulting in external, acidic silanol groups (Si−OH). After 10 h conversion, all catalysts possess fewer acid sites but these do not directly

6: For further calculations, the acidity determined with the 2nd-TPD has been used. This was the initial amount of acid sites when starting the conversion reaction.

correlate to the observed catalytic behaviour in figures 4.7 and 4.8. Al-MFI(11) has conserved most of its acid sites, even though it was the first catalyst to become deactivated. The ammonia-TPD profiles are further explored by deconvolution, as shown in figure 4.10.

Here, experimental data (dark grey) has been fitted (black) in which a linear background (light grey) was subtracted. The fit can be divided into several different Gaussian-shaped peaks (blue); the higher the desorption temperature, the stronger the acid site. The peaks can be grouped based on the temperature of maximum desorption, resulting in weak (w, ≤200 °C), medium (m, 200 °C to 250 °C), strong (s, 250 °C to 350 °C) and extra-framework (ex, ≥350 °C) acid sites [134, 150]. Each peak area is converted into the number of acid sites, normalised to the sample weight, and the results are summarised in table 4.4. Fresh Ga-MFI(33) and Al-MFI(41) catalysts possess a relatively similar number of acid sites of 0.179 and 0.173 mmol g^{-1} respectively, while Al-MFI(11) has around 3 times as many acid sites with 0.538 mmol g^{-1}.

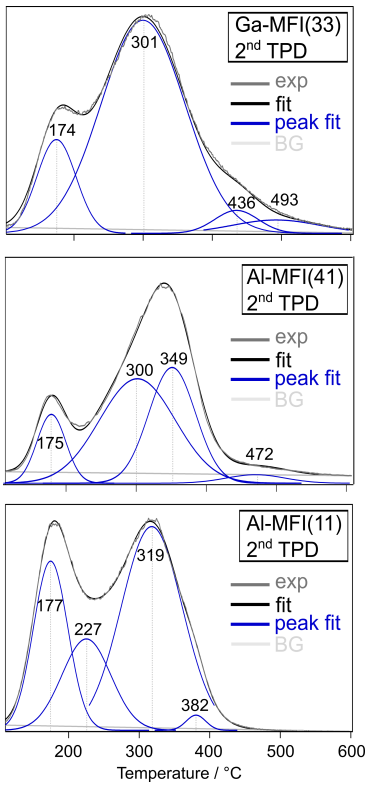

Figure 4.10: Analysis of experimentally determined ammonia-TPD profiles (dark grey) by fitting a curve (black) and deconvoluted peaks (blue) with Gaussian peak shape (Igor Pro 8, multipeak fitting 2).

After 10 h conversion of 2,5-DMF, Ga-MFI(33) and Al-MFI(41) have lost nearly all of their acid sites, possessing only 0.029 and 0.033 mmol g^{-1}; a loss of 84 and 81 % respectively. Even though all types of acid sites were affected, the weak and medium sites were affected the least, whereas the strong and extra-framework acid sites disappeared considerably or completely. During the reaction, the selectivities shifted from aromatics like benzene to isomerisation products like 2,4-DMF, which were still produced after 10 h for Ga-MFI(33) and Al-MFI(41). Hence, it can be suggested that the strong and extra-framework acid sites are involved in aromatics formation, whereas the weak and medium sites are responsible for the isomerisation reactions. Since 2,4-DMF was not detected at the start of the reaction, this is most likely an intermediate that is rapidly converted into benzene over the strong and extra-framework acid sites. Subsequent formation of coke species deactivates these sites, resulting in the detection of 2,4-DMF with increasing TOS.

To elaborate, the extra-framework peaks are thought to be located in the ion exchange site and synergistically interact with framework gallium to form a strong acid site [151]. Pyridine adsorption IR performed in this work determined that the site was a Lewis acid site [151]. This peak was not observed when gallium was impregnated into Si-MFI indicating that the strong Lewis acid sites only form in the presence of Brønsted acid sites [152]. When gallium isomorphously substitutes silicon in the zeolite framework, the tetrahedral (T) sites, interaction with extra-framework species like gallium creates Lewis acid sites that are energetically favourable for reaction pathways leading to aromatisation [153]. However, one should be careful when assigning Lewis acidity to extra-framework

Table 4.4: Analysis of the NH_3-TPD profiles right before and after the reaction. Desorption peaks are grouped into weak (w, ≤200 °C), medium (m, 200 °C to 250 °C), strong (s, 250 °C to 350 °C) and extra-framework (ex, ≥350 °C) acid sites.

Sample		Ga-MFI(33)			Al-MFI(41)			Al-MFI(11)		
Status	Peak #	T /°C	C / mmol g^{-1}		T /°C	C / mmol g^{-1}		T /°C	C / mmol g^{-1}	
Fresh (2nd TPD)	1	174	0.028	w	175	0.022	w	177	0.139	w
	2	301	0.136	s	300	0.087	s	227	0.107	m
	3	436	0.008	ex	349	0.059	s	319	0.285	s
	4	493	0.008	ex	472	0.005	ex	382	0.007	ex
	total		**0.179**			**0.173**			**0.538**	
Spent	1	170	0.006	w	161	0.005	w	171	0.081	w
	2	216	0.008	m	198	0.007	w	235	0.119	m
	3	283	0.014	s	300	0.021	s	332	0.160	s
	total		**0.029**			**0.033**			**0.359**	

species since another work has established that the amount of extra-framework aluminium does not always correlate with the total number of Lewis sites in several zeolites [154].

Besides extra-framework sites, strong acid sites are also lost during the reaction. These sites are associated with Brønsted acid sites caused by gallium or aluminium in T sites [155], supporting the interplay of Lewis acidic extra-framework sites with Brønsted acidic framework sites [153]. The formed coke is assumed to only reduce the acid site concentration, but not the acid site strength and the acid sites can often be regenerated under oxidative high-temperature conditions [156].

In contrast to the other 2 catalysts, Al-MFI(11) only lost 33 % of its acid sites, from 0.538 to 0.359 mmol g^{-1} even though it was completely inactive for both BTX production and isomerisation after several hours. Moreover, all acid sites appear to be reduced equally, except for the extra-framework peak at 382 °C which completely disappeared. This could indicate that not all of its medium and strong acid sites are involved in the reaction. However, this opposes the trend that was observed in Ga-MFI(33) and Al-MFI(41) between deactivation towards aromatics and near complete deactivation of strong acid sites. Another reason could be that formed coke species obstruct the reagents and formed products to respectively reach and leave the microporous structure of the catalyst. Some of the measured acid sites might only be accessible to the small NH_3 molecule and not to 2,5-DMF.

If table 4.3 is reproduced but normalised to the number of initial acid sites, table 4.5 is produced. Here, the superior production of aromatics by Ga-MFI(33) is highlighted, as it possesses fewer acid sites than Al-MFI(11), so the BTX signal is much higher in counts per mmol acid sites.

Table 4.5: BTX production for catalyst set 1, detected by MS (counts) and normalised to the number of initial acid sites (2nd NH_3-TPD).

Ga-MFI(33)	10^6 counts / mmol sites
benzene	229578
toluene	3288
xylenes	132
Al-MFI(41)	
benzene	28251
toluene	3071
xylenes	148
Al-MFI(11)	
benzene	36408
toluene	1412
xylenes	17

Take-home message
Aromatisation reactions are catalysed by strong and extra-framework acid sites whereas isomerisation reactions are catalysed by weak acid sites. Catalyst deactivation is caused by the coking of strong and extra-framework acid sites, or inhibition of access to the acid sites, like in Al-MFI(11). At the start of the reaction, 2,4-DMF is further converted into benzene on strong and extra-framework acid sites and thus only detected after these sites have become deactivated.

4.2 Influence of temperature

Due to the complex nature of the reaction, changing the reaction temperature not only changes the reaction rate but also the product distribution. Therefore, the reaction was performed over Ga-MFI(34) (set 2, different sample than Ga-MFI(33)) for 1 h at different temperatures, including 400 °C, 500 °C, and 600 °C. The conversions and the selectivities towards main aromatic products, benzene, toluene, and 2,5-DMF, are shown in figure 4.11; no para-xylene was formed. At 600 °C, the conversion rapidly reaches 100 % after which it gradually decreases to 65 % after one hour, with an initial benzene selectivity of 73 % decreasing to 29 %. Even though the initial benzene selectivity at 500 °C reaches 82 %, this rapidly falls off and is surpassed by 600 °C after five minutes TOS. It becomes clear that a reduction in temperature to 500 °C and 400 °C is accompanied by a reduction in conversion, as well as selectivity towards the aromatics benzene and toluene. On the contrary, by lowering the reaction temperature, the selectivity towards 2,4-DMF is increased to an initial value of 47 % increasing up to 65 % at the end of the hour. For further experiments, 500 °C has been chosen as the reaction temperature, even though more aromatics are formed at 600 °C. This is done to prevent catalyst degradation due to high-temperature reaction, which could lead to framework damage as well as migration of the metal, like gallium, from framework positions to extra-framework positions. Moreover, besides the amplified formation of monoaromatics, formation of polyaromatics such as coke precursors is also stimulated at high temperatures, resulting in irreversible coking of the catalyst. However, catalyst deactivation behaves differently at 500 °C than at 600 °C, possibly because light coke species are oxidised at 600 °C into CO and CO_2 in the presence of oxygen originating from 2,5-DMF. Catalyst deactivation towards aromatics with increasing TOS was observed for Ga-MFI(33) and Al-MFI(41) before, as well as an increase in 2,4-DMF selectivity, but now an additional influencing parameter has been identified: reaction temperature.

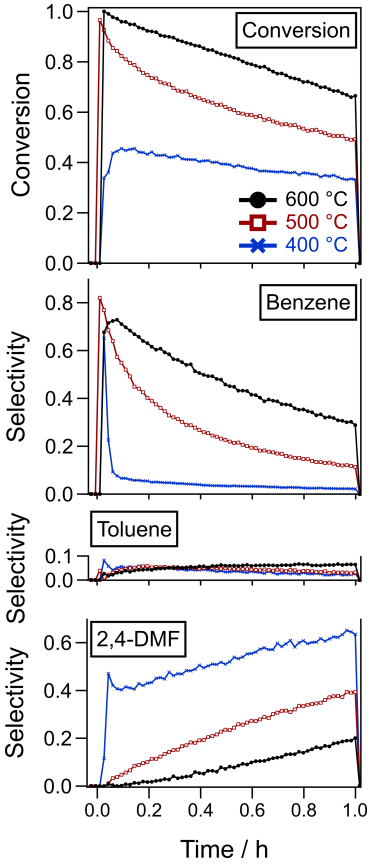

Figure 4.11: Conversion of 2,5-DMF and selectivities towards benzene, toluene, and 2,4-DMF over Ga-MFI(34) at different temperatures including 600 °C (black, sphere), 500 °C (red, square), and 400 °C (blue, cross). Reaction time of 1 h.

Take-home message
2,5-DMF can be converted into aromatics over a broad temperature range from 400 °C to 600 °C, with the highest benzene production at 600 °C. However, high temperatures may damage the catalyst and further studies were performed at 500 °C or below.

Valorisation of 2,5-DMF is not restricted to the production of aromatics, but can also be extended to the production of other products. One such product is the isomer 2,4-DMF, whose rare disubstitution pattern can be used for the synthesis of stereoselective organics [157, 158]. However, it is generally difficult to access [159] synthetically and not produced commercially on a large scale, despite the development of several successful synthesis routes [159–161]. The isomerisation of 2,5-DMF to 2,4-DMF has been investigated in paper II, including both experimental optimisation and mechanistic understanding.

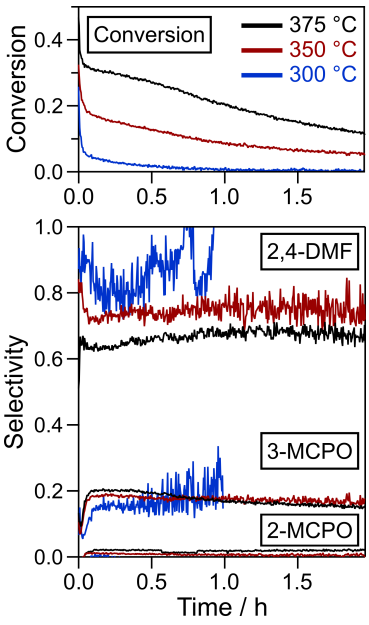

Figure 4.12: Conversion of 2,5-DMF and selectivities towards 2,4-DMF, 3-MCPO, and 2-MCPO over Ga-MFI(33) at different temperatures including 375 °C (black), 350 °C (red), and 300 °C (blue).

Accordingly, conversion of 2,5-DMF over Ga-MFI(33) (set 1) has been investigated at 300 °C, 350 °C, and 375 °C, as shown in figure 4.12. An initial temperature screening (not shown) determined that no conversion of 2,5-DMF occurs at 200 °C. Further experiments involving low-temperature adsorption of 2,5-DMF followed by a gradual increase in temperature, allow for determining the optimal formation temperatures of individual products. However, the catalytic, chemical environment is presumed to be different than under constant flow of 2,5-DMF and thus care must be taken when comparing the methods. An optimum for 2,4-DMF production has been identified between 330 °C and 380 °C.

Initial conversion of 2,5-DMF at 375 °C was 47 %, decreasing to 11 % after 2 h TOS, the conversion at 350 °C dropped from 32 % to 5 %, and the conversion at 300 °C rapidly dropped from 26 % to 6 % after 2 minutes, and further down to zero after 1 hour. Lower temperatures favour selectivity towards 2,4-DMF, with average selectivities of 85 %, 75 %, and 65 % for reaction temperatures of 300 °C, 350 °C, and 375 °C respectively, over 2 hours. Due to the low conversion at 300 °C, all measured product concentrations are so low that background noise prevents accurate calculations of the selectivities. Therefore, the selectivities at 300 °C have been smoothed (binomial, bounce, factor 20) and only selectivities up to 1 hour TOS are shown in figure 4.12 (blue line). Other isomerisation products, such as 3-MCPO and 2-MCPO, are also measured and a subtle trend can be seen that their formation is favoured by high temperature, in contrast to 2,4-DMF, which suggests that their formation follows a different mechanism, possibly over different active sites.

To test the consistency and reliability of the observed conversion, the experiment was repeated at 350 °C for 3 more cycles, as shown in figure 4.13. Both selectivity and conversion remain stable throughout the four cycles, suggesting an intact catalyst framework hosting active sites that can be regenerated without significant permanent deactivation. This also validates the methodology of performing multiple experiments in series such as in figure 4.12, although ideally, each experiment should be performed on a fresh, pristine catalyst.

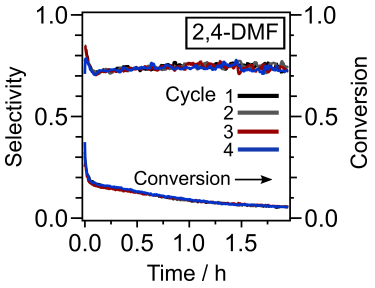

Figure 4.13: Conversion of 2,5-DMF and selectivities towards 2,4-DMF of 4 successive cycles of 2 h at 350 °C over Ga-MFI(33). The catalyst was oxidised in 20 % O_2 at 625 °C between each cycle.

As shown before in section 4.1.2, Al-MFI(41) with low acidity behaves similarly to Ga-MFI(33) at 500 °C, in the way that after deactivation of the strong acid sites after roughly 2 hours, 2,4-DMF is still produced as the main product. Reference materials such as pure siliceous Si-MFI and Ga_2O_3 have been studied as well, but both were not active for 2,5-DMF conversion. Based on these observations, it is proposed that isomerisation of 2,5-DMF requires both a confined microporous framework structure and catalytically active (acid) sites. In MFI-framework zeolites, incorporation of both gallium or aluminium results in catalytic active sites, and further research can determine the role of the substituted metal in more detail.

Previous work has shown that Al-MFI catalysts are more efficient in producing 2,4-DMF than Al-BEA catalysts, and future testing of Ga-BEA catalysts will determine if a similar trend holds for gallium. The difference in performance between the two frameworks could be due to the difference in pore sizes: MFI has a pore width similar to the kinetic diameter of the furan ring (5.5 Å) whereas BEA has slightly bigger pores (7.0 Å). As a result, there are fewer steric interactions between the BEA framework and 2,5-DMF molecules, which indicates that pore confinement promotes 2,4-DMF formation.

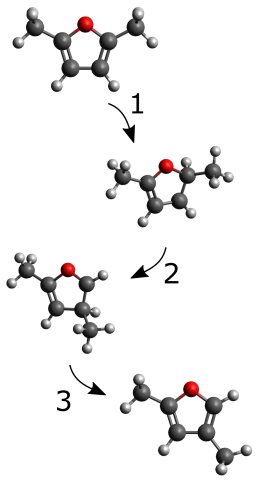

Figure 4.14: Schematic overview of the different transition states in the isomerisation of 2,5-DMF to 2,4-DMF in Ga-MFI zeolite, including proton transfer (step 1), followed by methyl migration (step 2), and a final proton back transfer (step 3). Determined with DFT and transition states are not shown (paper II).

Based on the observations above, it is suggested that isomerisation of 2,5-DMF to 2,4-DMF occurs through an acid-catalysed methyl-migration that is supported by steric confinement in the MFI structure (paper II). The reaction landscape is calculated with density functional theory (DFT) calculations and the elementary steps are as follows. After 2,5-DMF adsorption on Ga-MFI, proton transfer to one of the carbons next to the oxygen in 2,5-DMF (position 2 or 5) occurs, changing the sp^2 hybridisation to sp^3 hybridisation. This is followed by the transfer of the $-CH_3$, and consequently, the sp^3 hybridisation, from site 5 to site 4. Once the $-CH_3$ is at site 4, the proton will be transferred back to the Brønsted acid site, thereby forming the 2,4-DMF. Finally, the 2,4-DMF will desorb and leave the zeolite. All proton transfers occur with relatively low energy barriers and the $-CH_3$ transfer is shown to be the rate-controlling step.

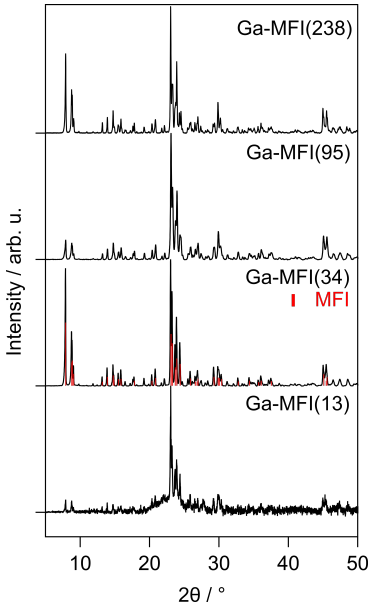

Figure 4.15: XRD patterns of MFI-zeolite with different Si/Ga ratios. Background subtracted, normalised to the highest intensity, and vertically displaced for clarity. Ga-MFI(238) and Ga-MFI(95) horizontally displaced with x=-0.19 to account for the different sample heights. Reference MFI peaks (red sticks) are silicalite-1 [162].

Take-home message
2,5-DMF can be selectively isomerised into 2,4-DMF (and 3-MCPO) at relatively low temperatures between 300 °C to 400 °C, using either Al-MFI or Ga-MFI catalysts. DFT calculations support the proposed mechanism of a proton transfer followed by a methyl migration.

4.3 Influence of the gallium content

After determining the positive effect of gallium incorporation, the influence of changing the gallium content has been explored by catalyst set 2. This set comprises Ga-MFI catalysts with different Si/Ga ratios: 13, 34, 95, and 238.

4.3.1 Structural analysis

XRF

XRF results shown in table 4.6 show a slight discrepancy between the Si/Ga ratios of the synthesis gel and the final zeolites, which can be explained by the disruptive role that gallium plays in the formation of the zeolite. The charged gallium-containing tetrahedrons need counterions to balance their negative charge, and the large size of the gallium ion[7] also places strain on the Si–O–Ga bonds in the unit cell. Due to these reasons, not all gallium was incorporated into the MFI-framework.

The Ga-MFI catalysts are mostly made up of silicon, oxygen and gallium. They also contain water adsorbed from the air (determined by TGA) and sodium originating from the precursor material NaOH.

7: reminder: Ga(III) ionic radius (62 pm) > Si(IV) ionic radius (40 pm)

Table 4.6: Elemental compositions of catalyst set 2, Ga-MFI(Si/Ga). Samples are named after their Si/Ga ratio, Si/Ga of the synthesis gel shown in column 2. Oxygen wt% is derived by assuming metals to be present as oxides. H_2O determined by TGA at 200 °C. Normalised to a total weight percentage of 100 wt%.

Sample	Si/Ga	Ga	Si	O	Na	H_2O
	gel			/wt%		
238	155	0.5	45.9	53.5	0	5.5
95	60*	1.2	45.5	53.2	0	5.5
34	22	3.2	43.5	52.9	0.11	1.0
13	10	7.6	39.0	52.2	0	1.2

* weighing error, inaccurate gallium mass

XRD

XRD was measured and the patterns are shown in 4.15, together with the calculated peak positions of pure Si-MFI [162].

All catalysts demonstrate peaks at the positions associated with the MFI framework. However, Ga-MFI(13) demonstrates a large, broad peak from 2θ=20 to 2θ=30, which is ascribed to an amorphous fraction of the sample. The low peak intensities and the noisy shape of the XRD pattern or caused by this amorphous phase, which also resulted in a large background (not shown). Due to the use of two different sample holders and thus different sample heights, there is a systematic peak shift for the same experiments which is corrected by shifting the graph by 0.19° to lower angles.

The experimental settings were slightly different between the samples resulting in increased intensity at low angles for Ga-MFI(34), since this was measured with a fixed slit width instead of a fixed sample illumination area. Therefore, relative peak intensities will not be analysed further.

SEM and EDX

The size, shape and morphology of the catalyst crystals have been investigated by measuring SEM. When combined with EDX, elemental mapping can be performed, as shown in figure 4.16. Here, a catalyst particle, Ga-MFI(34) was applied to carbon tape on a sample holder and then coated with a thin layer of gold (4 nm) to increase conductivity. SEM was measured at low voltage (1 kV, top), illustrating a catalyst particle of roughly 40 by 60 µm. This particle is an agglomerate of smaller, crystalline particles of different sizes, ranging from a few µm down to 500 nm.

EDX was measured on the same particle at high voltage (20 kV) to excite the atoms leading to the emission of their characteristic X-rays. Kα X-rays of silicon, oxygen, gallium and carbon are measured, and the resulting elemental maps are shown in figure 4.16. Silicon and oxygen are measured with the highest intensity on the particles since they are the main components, and gallium with lower intensity. Gallium is distributed homogeneously throughout the catalyst particle, which indicates successful incorporation in the zeolite framework.

Besides elemental mapping, EDX can also be measured for point and line spectra, as has been done on Ga-MFI(34). Spectrum 2 & 3 are located on the catalyst particle and gallium contents of 3.3 wt% and 2.9 wt% have been measured, respectively, when ignoring carbon and gold. This corresponds to Si/Ga ratios of

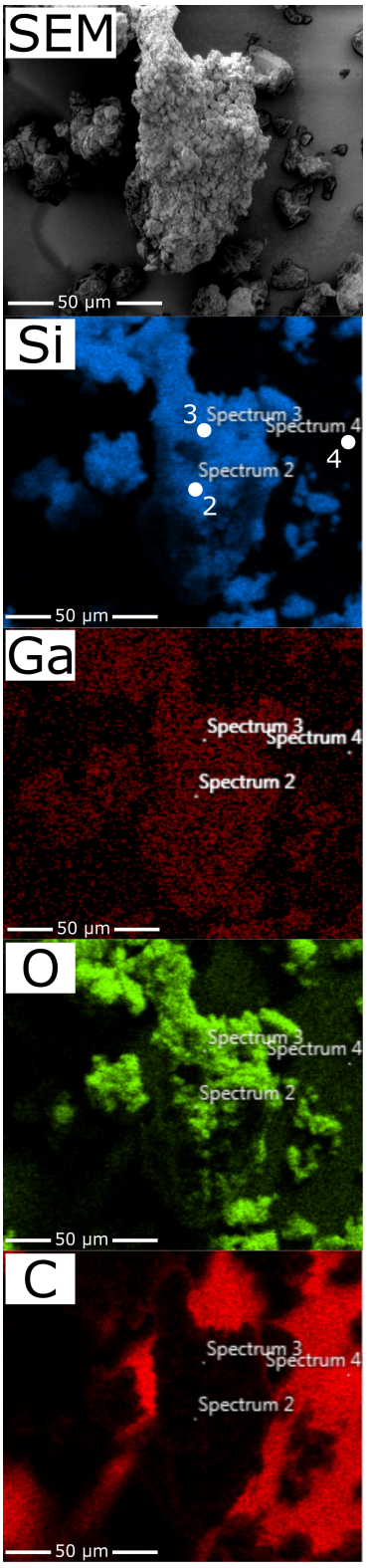

Figure 4.16: SEM image (top) of a Ga-MFI(34) particle coated with 4 nm Au, recorded at 1.0 kV. EDX maps recorded at 20 kV, illustrating Si (blue), Ga (dark red), O (green), and C (light red). The brightness (+40 %) and contrast (-40 %) are corrected for Ga to increase visibility.

Si/Ga=36 and 35, which is in reasonable accordance with the bulk Si/Ga ratio of 34 as determined with XRF. The slightly lower measured content might suggest that the majority of the gallium is situated deeper inside catalyst particles, or that gallium species are clustered but not visible for this particular particle. Spectrum 4 on the background measured 99.5 % carbon and 0.5 % silicon, illustrating the credibility of this technique.

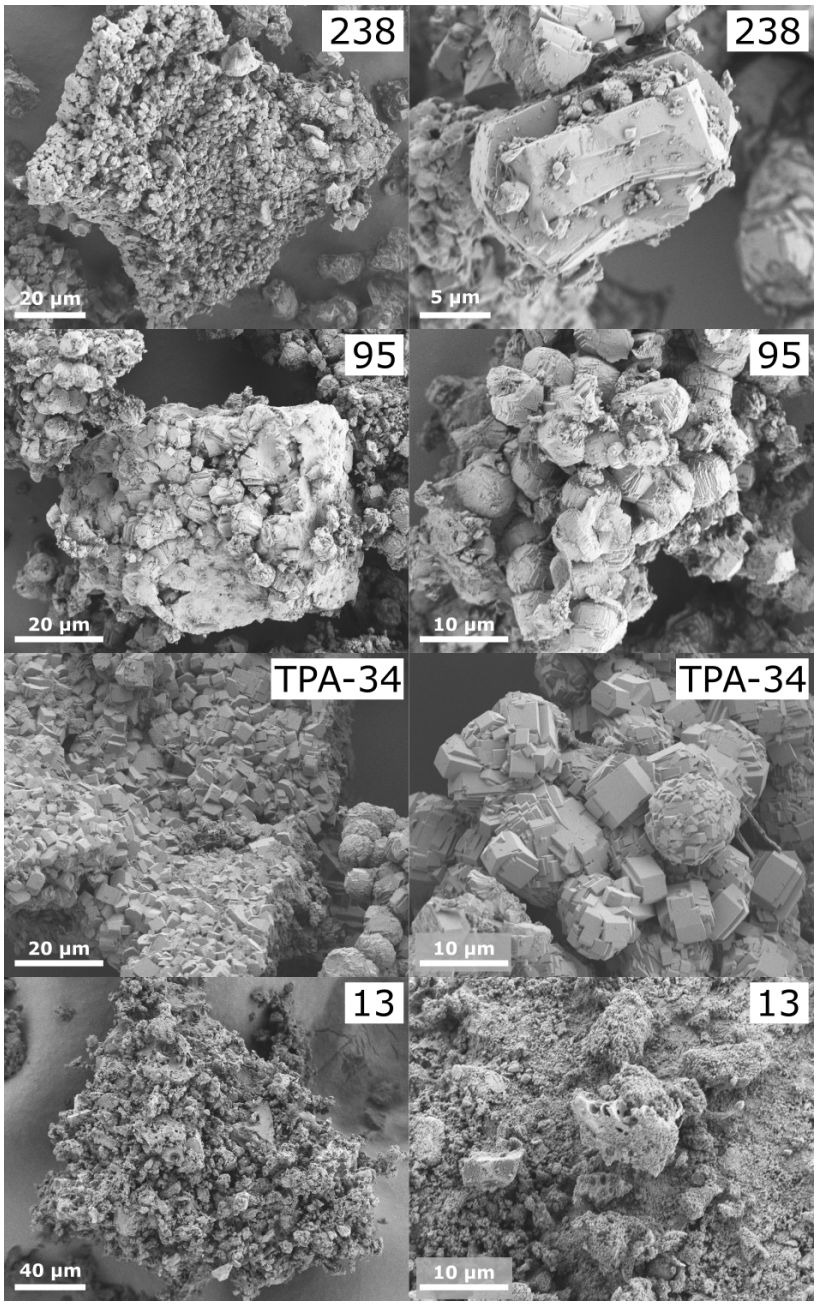

Figure 4.17: SEM images of Ga-MFI zeolites (set 2) with different Si/Ga ratios of 238, 95, 34, and 13, displaying the crystalline particles (left) and a close-up (right). All samples are in the protic form, H-Ga-MFI, and are not coated, except for TPA-Ga-MFI(34) which is in the as-synthesized form and is coated with 4 nm Au. Recorded at 1 kV.

SEM images of the Ga-MFI catalysts in set 2 are shown in figure 4.17. All samples are in the final protic form, H-Ga-MFI, except for Ga-MFI(34) which is in the as-synthesized form including the organic template TPA, TPA-Ga-MFI(34). All catalysts consist of particles of different sizes, ranging from small crystallites of

1 µm^2 to large agglomerates that can reach dimensions up to 100 µm by 100 µm. Typical Ga-MFI(238) particles consist of clusters of crystallites that are cubic-shaped or coffin-shaped, i.e., two parallelepiped embedded in one another orthogonally. This latter shape is characteristic of MFI-framework zeolites as can be seen for pure Si-MFI (figure 4.5), which is in line with the low gallium content of this sample.

When more gallium is incorporated, and thus when the Si/Ga ratio goes down, only cubic-shaped crystallites are formed. The small, irregular structures on the external facets of the crystals (238, right side) were also seen for catalyst set 1, and could potentially be caused by phase impurities or migrated gallium during the calcination steps [148]. However, TPA-Ga-MFI(34), which has not been exposed to any heat treatment yet, also possesses similar irregularities. Even though they are present in smaller quantities, this cannot be gallium that migrated during post-synthesis treatment.

Other factors that influence the crystal shape are the reaction conditions themself, including temperature and duration of the hydrothermal step. Moreover, supersaturation, nutrient mobility, and kinetics also play a role. The small irregularities on the crystal facets can be crystal nuclei that have not fully grown and this can be further examined by altering the zeolite synthesis. For example, a two-step temperature ramp can first favour rapid crystal nucleation followed by slower crystal growth, resulting in a more homogeneous size distribution of catalyst particles. When the gallium content is increased up to Si/Ga=13, no regular crystalline shapes can be detected, and the catalyst particles resemble amorphous intergrowths. This supports the amorphous character of this sample previously observed with XRD in figure 4.15.

Physisorption

Textural properties have been analysed by N_2-physisorption and the isotherms are shown in figure 4.18. All adsorption isotherms can be considered composites between type I and type IV [112]. Type I demonstrates a steep uptake at relative pressures near 0, ascribed to micropore filling, followed by a plateau of uptake due to the limited micropore access. Type IV is associated with material containing large micro- or mesopores which can be present within crystals or between zeolite crystals.

The isotherm of Ga-MFI(238) displays a second uptake step between p/p_0=0.2 and p/p_0=0.3, resembling the isotherm of Si-MFI in figure 4.3. This was attributed to the reorientation of nitrogen to favour quadrupole-quadrupole interactions and is not seen for the

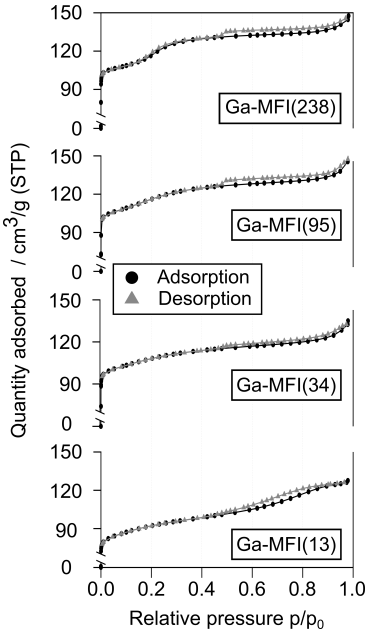

Figure 4.18: N_2-physisorption isotherms at 77K of the catalyst set 2. Nitrogen adsorption (circles, black) and desorption (triangles, grey).

other samples because the gallium content is much higher, leading to preferential adsorption [114, 122, 145].

All isotherms display hysteresis loops of type H4 between p/p_0=0.5 and p/p_0=1.0, associated with capillary condensation. This is indicative of zeolites containing micro- and mesopores, as well as meso- and macropores between zeolite crystal aggregates [112]. The small hysteresis visible on Ga-MFI(238) between p/p_0=0.2 and p/p_0=0.3 is not due to capillary condensation, but due to the molecular rearrangement of adsorbed nitrogen which requires an increased energy barrier to desorb [122]. Argon physisorption was also performed and an overview of the textural properties is shown in table 4.7. All samples possess a high SA and microporous volume, with a decreasing surface area when the gallium content is increased. For Ga-MFI(13), two fractions were collected and tested: the first fraction was collected from the synthesis liquor and the powder that was formed. By contrast, the second fraction was stuck to the inside of the synthesis vessel and was collected after soaking a few days in water and using mechanical force to remove the powder; this appeared to have a low surface area. Further investigation by XRD can determine the crystallinity of this fraction and lead to insights into the synthesis.

Table 4.7: Textural properties of catalyst set 2, Ga-MFI(Si/Ga), derived from nitrogen and argon isotherms.

Sample	Ads.	SA* / $m^2\ g^{-1}$	$S^{\dagger}_{micro}$ / $m^2\ g^{-1}$	$S^{\dagger}_{ext}$ / $m^2\ g^{-1}$	$V^{\dagger}_{micro}$ / $m^3\ g^{-1}$
238	N_2	445	418	27	0.185
	Ar	467	448	19	0.157
95	N_2	435 ± 9	404 ± 7	31 ± 1	0.175 ± 0.001
	Ar	475	462	12	0.161
34	N_2	420 ± 1	393 ± 1	28 ± 2	0.162 ± 0.003
	Ar	464 ± 2	456 ± 2	9 ± 1	0.160 ± 0.001
13	N_2	349	288	60	0.118
13‡	N_2	66	33	34	0.015

* Apparent surface areas by BET method, p/p_0 = 0.002-0.03 following consistency criteria.[109]
† by t-plot method (Harkins and Jura equation, t= 5.0 - 8.0 Å)
‡ residual fraction grown on liner and dissolved in water

Argon physisorption yielded slightly higher SA than with nitrogen, which will be explained in later sections.

TGA and DSC

The hydrothermal stability of the set 2 H-Ga-MFI catalyst is tested by TGA and DSC in air, and the results are shown in figure 4.19, A. The total weight losses are 1.3 %, 1.5 %, 3.0 %, and 8.0 % for catalysts with Si/Ga ratios of 238, 96, 34, and 13, respectively. Most

of the weight loss occurs between 100 and 200 °C, caused by the desorption of water.

To investigate and optimise the synthesis conditions of the catalysts, figure 4.19, B, displays the TGA and DSC profiles of dried, as-synthesised catalysts, TPA-Ga-MFI. Besides Ga-MFI(13), minor weight loss associated with water occurs at low temperatures, suggesting low water contents. However, all catalysts undergo a major weight loss step between 430 and 500 °C, ranging from 11.3 % to 9.8 %, 8.4 %, and 4.8 % for Si/Ga= 238, 96, 34, and 13, respectively.

This weight loss is ascribed to the decomposition of the organic template cations, TPA^+, into amines, aromatics, and finally carbon oxides [163]. In fact, the decomposition itself results in the formation of Brønsted acid site, allowing for further acid-catalysed decomposition [164]. However, most counterions present are still Na^+ and need to be ion exchanged and further transformed into H^+. The decomposition into amines, oligomers and aromatics is proposed to occur through a Hofmann elimination followed by β-elimination [165, 166], after which they are oxidised under air flow. The oxidation is supported by the negative peak in the heat flow, which signifies that less heat is needed to increase the sample temperature with e.g., 1 °C, compared to an empty reference crucible. In other words, the negative peak is associated with an exothermic event.

A trend can be identified between the size of the weight loss and the gallium content of the catalyst: more gallium equals less incorporated TPA^+.[8]The theoretical limit of the total pore filling amounts to four quaternary ammonium cations, four hydroxides, and at least four water molecules per unit cell [167]. This adds up to 13.3 %, which is close to the total weight losses of 13.2 %, 12.4 %, 11.5 % and 11.1 % of Ga-MFI catalysts with Si/Ga ratios of 238, 96, 34, and 13, respectively. The slight variations in temperature of the weight loss step and size of the DSC peak can be caused by the different binding interactions between gallium and TPA^+.

TGA/DSC experiments under inert nitrogen flow (not shown) result in similar weight losses but a different DSC profile, due to endothermic pyrolysis reactions shown to occur for quaternary ammonium SDAs [163].

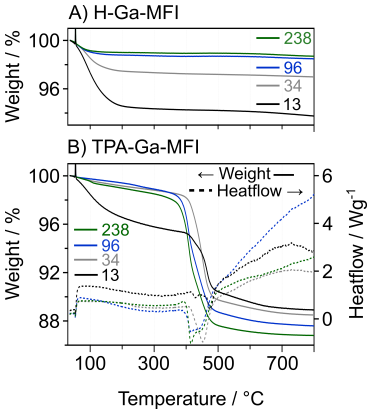

Figure 4.19: TGA and DSC profiles of catalysts from set 3 over a temperature range of 30 °C to 800 °C in 60 mL min^{-1} air (heating ramp of 10 °C min^{-1}). Samples are in their final protic form, H-Ga-MFI (A), or in their as-synthesised form, TPA-Ga-MFI (B).

8: Reasons could be

- Ga is heavier than Si so a smaller loss in sample wt% could equal a similar number of TPA molecules for high Ga catalysts.
- Ga is present as extra-framework gallium species, obstructing TPA occlusion in pore channels and intersections.
- presence of amorphous or other crystalline phases

Take-home message
A series of Ga-MFI with different Si/Ga ratios has been successfully synthesised. XRD and SEM have identified crystalline, MFI-framework structures. XRF and EDX were used to analyse elemental compositions. TGA and DSC identified high thermal stability and physisorption identified a microporous structure with a high apparent surface area for all catalysts.

4.3.2 Limit of the gallium content

After the initial screening of catalyst set 2, the optimal gallium content is explored by synthesising three more Ga-MFI catalysts: set 3.

In the XRD patterns of set 2 (figure 4.15), Ga-MFI(13) appears to contain amorphous material whereas Ga-MFI(34) contained phase-pure MFI-zeolite. This suggests that the limit of the maximum gallium lies between Si/Ga=13 and Si/Ga=34. To approach this limit and prevent the synthesis of amorphous material, another synthesis was performed with twice the amount of crystallisation time: 10 days instead of 5 days. This provides enough time for crystal nucleation and growth, and three Ga-MFI catalysts with a high gallium content have been synthesised. Their elemental compositions are measured with XRF and shown in table 4.8.

XRF

Table 4.8: Elemental compositions of catalyst set 3. Samples are named after their Si/Ga ratio, Si/Ga of the synthesis gel shown in column 2. Oxygen wt% is derived by assuming metals to be present as oxides. H_2O determined by TGA at 200 °C. Normalised to a total weight percentage of 100 wt%.

Sample	Si/Ga	Ga	Si	O	Na	H_2O	Res.
	gel			/wt%			
17	20	6.1	41.9	51.7	0.09	2.1	0
8	15	12.2	38.1	48.8	0.81	1.1	0.02*
7	12.5	13.9	36.9	47.8	1.34	0.7	0.07†

* Br, S
† Br, Fe, Pt

XRF results indicate that silicon-to-gallium ratios are lower in the final zeolites than the synthesis gels, meaning that the gallium content is higher than was aimed for. This suggests that for long crystallisation times of 10 days, gallium incorporation in the zeolite framework is favoured. However, it can also indicate that different (crystalline) phases and species of gallium have formed.[9]

9: traces of Br originate from the template (TPABr) whereas Fe might originate from the gallium source or impurities caused by the glassware and instruments.

XRD

To test if the MFI-framework was still formed with these high gallium contents, as well as to test for the presence of other phases, XRD has been performed. Figure 4.20 shows the XRD patterns of Ga-MFI(7), Ga-MFI(8), and Ga-MFI(17) and figure 4.21 zooms in on a region of interest.

Besides the peaks characteristic to the MFI-framework, other peaks have been identified as well for Ga-MFI(8) and Ga-MFI(7), of which the most intense are labelled with a $*$ or $+$ in figure 4.20. Peak fitting ascribed the peak at 26.6°to hexagonal α-quartz (SiO_2, COD-9005018 [169]) and the two broad peaks at 21.9°and 27.7°to gallium albite ($GaNaSi_3O_8$, COD-9001313 [168]). $\alpha-$Quartz is the most common polymorph of crystalline silica and thermodynamically favoured at low temperatures while gallium albite can be synthesized through annealing at high temperatures and pressures. Under the used synthesis conditions[10] high pressures can be reached inside the vessel. However, for Ga-MFI(17), these different crystalline phases are not observed even though the crystallisation conditions were similar. This can be due to the lower amount of gallium, but also due to the lower amount of sodium present in the synthesis gel.[11] Further syntheses could use the basic version of the template, TPAOH, instead of TPABr which requires less NaOH to be added.

As the Ga-MFI(7) and Ga-MFI(8) samples are not phase pure, it is difficult to ascribe any catalytic performance to the MFI-fraction of the sample. Moreover, specific quantities such as surface area and acidity are determined per gram catalyst, and will therefore be incorrect for these samples. The mentioned gallium ratio might not be the actual Si/Ga ratio of the zeolite fraction, and finally, the mass of the loaded MFI-fraction of the catalyst will differ. These problems can be corrected for if the different phases are quantified, for example by adding a known amount of pure $\alpha-$quartz and gallium albite to the sample and performing XRD.

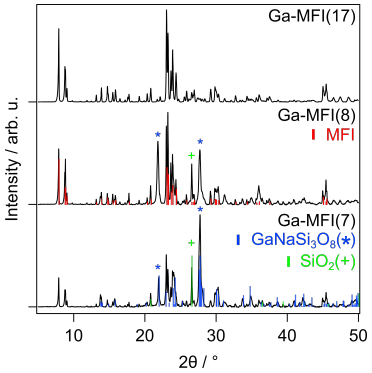

Figure 4.20: XRD patterns of MFI-zeolite with different Si/Ga ratios including Si/Ga=17, 8, and 7. Background subtracted, normalised to highest intensity, and vertically displaced for clarity. Reference peak patterns (peaks higher than 5 % relative intensity shown) include silicalite-1 [162], (SiO_2, red), albite [168] ($GaNaO_8Si_3$, blue), and α-quartz [169] (SiO_2, green).

10: an autoclave filled with liquid reagents up to a third of its volume, 175 °C for 10 days

11: reminder: the strong base NaOH was used to increase the pH of the synthesis gel, and more NaOH was added when more acidic gallium precursor was used, like for Ga-MFI(7) and Ga-MFI(8).

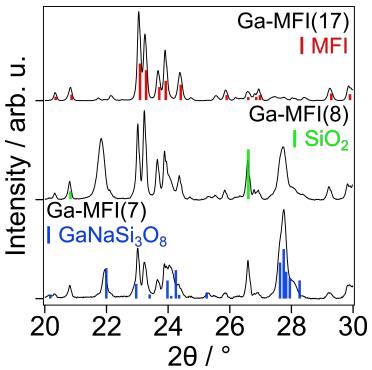

Figure 4.21: Close-up of XRD patterns of set 3 catalysts from figure 4.20.

TGA and DSC

The thermal stability has been analysed by TGA and DSC in air, which is shown in figure 4.22. All three catalysts show high thermal stability in their final protic form (A), with Ga-MFI(7) and Ga-MFI(8) losing around 1 wt% and Ga-MFI(17) around 2 wt% up to 200 °C, associated with water, up to 3 wt%. TGA and DSC of the as-synthesised catalysts (B) reveals a weight loss step around 450 °C, attributed to the exothermic decomposition of the organic template TPA^+.

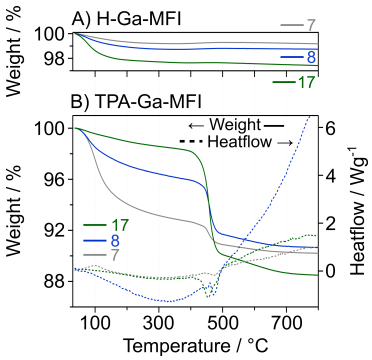

Figure 4.22: TGA and DSC profiles of catalysts from set 3 over a temperature range of 30 °C to 800 °C in 60 mL min^{-1} air (10 °C min^{-1}). H-Ga-MFI (A) and TPA-Ga-MFI (B).

Ga-MFI with Si/Ga ratios of 17, 8, and 7 lose 8.0, 4.2, and 1.2 wt%, respectively. This indicates that an increase in Ga loading follows a decrease in the amount of incorporated TPA^+ molecules, as was observed for catalyst set 2 as well, most likely due to the other phases that were formed.

SEM

Figure 4.23 displays the SEM images of Ga-MFI catalysts (set 3) with higher gallium content and longer synthesis durations.

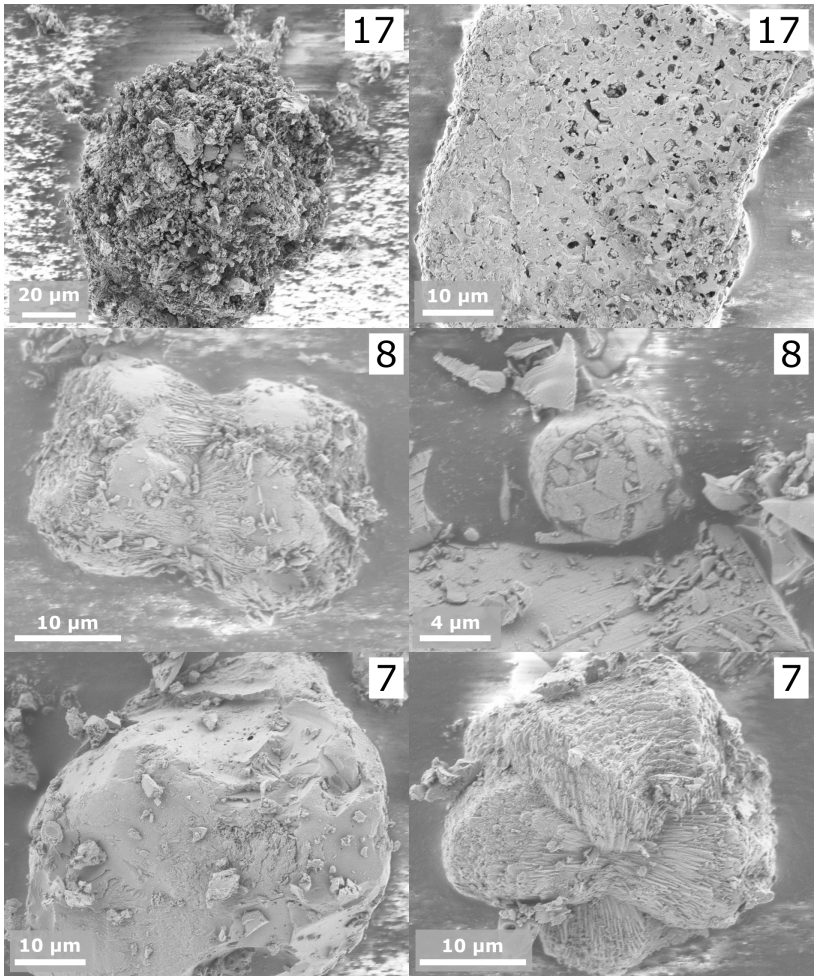

Figure 4.23: SEM images of Ga-MFI zeolites (set 3) with different Si/Ga ratios of 17, 8, and 7, displaying the crystalline particles (left) and a close-up (right). All samples are in the protic form, H-Ga-MFI, and are not coated. Recorded at 1.5 kV.

Similar as observed in Ga-MFI(13), many different irregular, particle shapes are observed. For Ga-MFI(17), besides irregularly shaped agglomerates, plate-shaped agglomerates are also detected (right side). These particles appear to contain macropores with diameters of 1 µm down to 100 nm, which could affect its catalytic performance due to facilitating the mass transfer of reagents and products deeper into the particle. When the gallium content was further increased, different types of particles were formed: crystalline particles consisting of layers or sharp needles, combining to form

larger particles (Si/Ga=8, left, and Si/Ga=7, right), as well as smooth particles.[12]

12: these particles could partially or fully exist out of α-quartz and gallium albite

Physisorption

Textural properties of catalyst set 3 have been analysed by N_2- and Ar-physisorption at 77 K, shown in figure 4.24.

All three isotherms resemble isotherm type I and type IV [112]. The filling of the micropores at low relative pressures for Ga-MFI(8) and Ga-MFI(7) requires much less nitrogen than for Ga-MFI(17), confirming the former low surface areas. Argon physisorption is also performed for Ga-MFI(17), as indicated by the blue curves, and this resembles a pure type I isotherm. Here, the hysteresis loop between p/p_0 =0.5 and p/p_0 =1.0 caused by capillary condensation, is only pronounced for nitrogen but not for argon. Since argon is 6.5 K below its triple point, capillary condensation can not occur in mesopores larger than 12 nm [170, 171]. The absolute amount of adsorbed argon in mmol is higher due to the smaller size of the argon molecule [125]. The apparent surface areas have been determined with nitrogen and argon and are shown in table 4.9.

Sample Si/Ga	Ads.	SA* / $m^2\ g^{-1}$	$S^{\dagger}_{micro}$ / $m^2\ g^{-1}$	$S^{\dagger}_{ext}$ / $m^2\ g^{-1}$	$V^{\dagger}_{micro}$ / $m^3\ g^{-1}$
17	N_2	390 ± 4	348 ± 7	43±11	0.142 ± 0.005
	Ar	435 ± 5	422 ± 6	14 ± 1	0.149 ± 0.002
8	N_2	163	152	11	0.062
7	N_2	83	68	13	0.029

Table 4.9: Textural properties of catalyst set 3, Ga-MFI(Si/Ga).

* Apparent surface areas by BET method, p/p_0 = 0.002-0.03 for Ga-MFI(17;8) and p/p_0 = 0.003-0.05 for Ga-MFI(7), following consistency criteria [109]
† by t-plot method (Harkins and Jura equation, t= 5.0 - 8.0 Å)

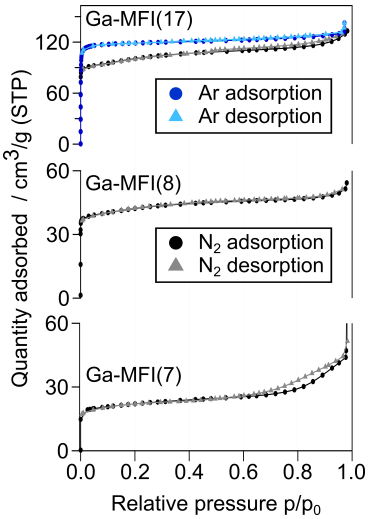

Figure 4.24: N_2 and Ar-physisorption isotherms at 77K of the catalyst set 3. Nitrogen adsorption (circles, black) and desorption (triangles, grey), Ar adsorption (circles, dark blue) and desorption (triangles, light blue).

Both Ga-MFI(8) and Ga-MFI(7) show low SA of 163 and 83 $m^2\ g^{-1}$, respectively, as well as low microporous volume. This demonstrates the disruptive influence of adding too much gallium, as well as the influence of the additional crystalline phases. Ga-MFI(17) is formed with high surface areas, suggesting phase-pure MFI formation. Analysis using argon yielded a higher SA and microporous volume, similarly to catalyst set 2. However, for pores of the sizes between 3.7 and 6.3 Å, which is the case for the MFI micropores, the SA determined with nitrogen and the BET-model is shown to underestimate the monolayer coverage [121]. The quadrupole moment of the nitrogen strengthens its interaction with the acidic zeolite framework, effectively increasing the number of adsorbed nitrogen molecules. However, the BET model assumes hard spheres to simulate nitrogen, thus the calculated surface packing will be lower than the actual packing [172], so perhaps the BET area

determined with Ar is closer to the true surface area. Further experiments at 87 K would be enlightening [112].

Take-home message
Ga-MFI catalysts with high gallium contents have been synthesised by increasing the crystallisation times. However, other crystalline phases such as α-quartz and gallium albite are formed as well. This leads to disadvantageous textural properties and a lower fraction of actual Ga-MFI zeolite.

4.3.3 Catalytic tests

The effect of gallium loading has been explored by performing 2,5-DMF conversion at 500 °C. NH_3-TPD has been performed before and after the reaction to measure the acid site density.

As seen previously in figure 4.7, Ga-MFI zeolites are initially selective to benzene production, which shifts to 2,4-DMF production with increasing TOS (not shown). To compare, the measured benzene concentrations over Ga-MFI with different Si/Ga ratios are shown in figure 4.25 during 1 h of 2,5-DMF conversion. Si-MFI from set 1 has been added as a reference (light grey). Except for Ga-MFI(13), all catalysts produce benzene and Ga-MFI(17) demonstrates superior performance. The production of benzene seems to follow a trend with the gallium content: more gallium equals more benzene produced. This holds up for Si/Ga=17, 34, 95, and 238, but not for Si/Ga=13. Perhaps a large fraction of the loaded catalyst sample is an inactive, amorphous phase.[13] The total amount of benzene produced over 1 h is displayed in table 4.10. This demonstrates that Ga-MFI(17) produces over three times as much benzene as Ga-MFI(34), even though it only has twice the amount of incorporated gallium.

The superior benzene production of Ga-MFI(17) has been explored further in a 10 h 2,5-DMF conversion experiment at 500 °C, as shown in figure 4.26. High conversion was detected of 100 % initially, down to 42 % after 2 h and 11 % after 10 h. Meanwhile, the catalyst is mainly selective to benzene during the first hour, with an initial benzene selectivity of up to 95 %, down to 25 % after 1 h, 5 % after 2 h, down to 1 % after 4 h. As seen in the other Ga-MFI samples, selectivity to isomerisation products such as 2,4-DMF, 2-MCPO, and 3-MCPO increases slowly, with a 2,4-DMF selectivity of 18 % after 1 h, up to 43 % after 3.5 h, and eventually down to 30 % after 10 h.

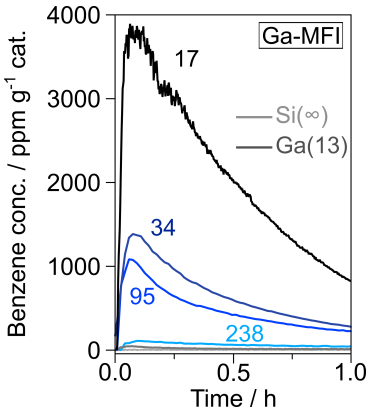

Figure 4.25: Overview of benzene production by Ga-MFI catalysts with different Si/Ga ratios from sets 2 and 3. Si-MFI from set 1 shown as reference (light grey), 600 ppm 2,5-DMF conversion at 500 °C for 1 h.

13: XRD uses up to a few grams of catalyst whereas only 50 to 100 mg are loaded in the reactor set-up. This could result in exclusively loading the amorphous fraction, especially when the sample is not homogeneous.

Table 4.10: Overview of benzene production in molecules over Ga-MFI catalysts with different Si/Ga ratios. 600 ppm 2,5-DMF conversion at 500 °C for 1 h.

Sample Si/Ga	Benz. produced / mmol/(g·h)
∞_{Si}	0.001
238	0.049
95	0.387
34	0.533
17	1.678
13	0.013

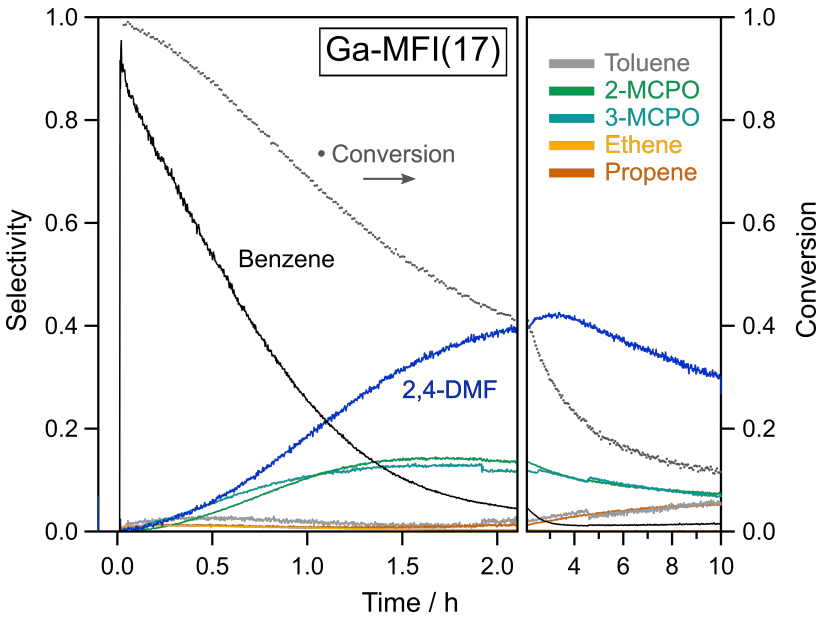

14: 1 h at 400, 500, and 600 °C with 1 h regeneration in between each step in 20 % O_2 at 625 °C.

Figure 4.26: Conversion of 2,5-DMF and selectivities towards the main products during a 10 h conversion reaction of 600 ppm 2,5-dimethylfuran at 500 °C. Selectivities from 2 h to 10 h (right pane) are smoothed for clarity (binomial, bounce, factor 20) Sudden drop for 3-MCPO (teal) at 1.9 h is ascribed to the calculation of the concentrations by FTIR, which switches the reference concentration.

NH_3-TPD

The acidity of the Ga-MFI catalysts has been investigated with NH_3-TPD and the measured ammonia concentrations for Ga-MFI(34) are shown in figure 4.27 and the acidity in table 4.11. NH_3-TPD on a fresh catalyst involved an incomplete linear desorption up to 550 °C (red curve) instead of 600 °C. This was followed by a conversion experiment[14] after which NH_3-TPD was performed twice in a row (black and dark grey) to 600 °C, and after 10 h conversion another time (spent catalyst, light grey).

Clear differences can be observed between the fresh catalyst in experiment 1 and experiment 2, as in the second experiment, the weak and strong peaks before 400 °C are smaller whereas the extra-framework peak around 500 °C is larger. This suggests that strong Lewis acid sites have formed, possibly connected to a Brønsted acid site, resulting from gallium migration during the high-temperature

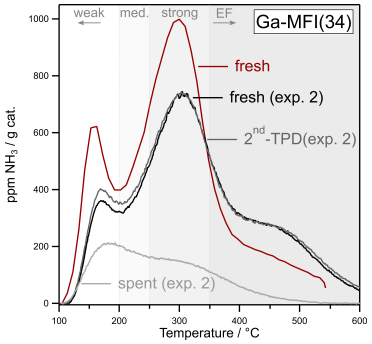

Figure 4.27: NH_3-TPD profiles of fresh Ga-MFI(34) (red curve, to 550 °C), after 3 h 2,5-DMF conversion (black curve, to 600 °C), second NH_3-TPD (dark grey curve, to 600 °C), and spent catalyst after 10 h 2,5-DMF conversion at 500 °C (light grey).

Table 4.11: Analysis of the NH_3-TPD profiles right before and after the reaction. Desorption peaks are grouped into weak (w, ≤200 °C), medium (m, 200 °C to 250 °C), strong (s, 250 °C to 350 °C) and extra-framework (ex, ≥350 °C) acid sites.

Status	Fresh exp. 1		Fresh exp. 2		2^{nd}-TPD exp. 2		Spent exp. 2	
Curve in 4.27	Red		Black		Dark grey		Light grey	
	T/ °C	C/ mmol g^{-1}	T/ °C	C/ mmol g^{-1}	T/ °C	C/ mmol g^{-1}	T/ °C	C/ mmol g^{-1}
	159 w	0.031	172 w	0.024	171 w	0.025	164 w	0.008
	218 m	0.051	300 s	0.142	299 s	0.145	205 m	0.010
	303 s	0.121	453 ef	0.032	452 ef	0.031	294 s	0.039
	432 ef	0.066	523 ef	0.028	527 ef	0.026		
total		**0.268**		**0.225**		**0.227**		**0.057**

conversion and regeneration steps in the experiment described in sidenote 14. In table 4.11 is shown that the pristine catalyst has lost acid sites from at least 0.268 to 0.225 mmol g^{-1}.

15: Ga-MFI(8) and Ga-MFI(7) not measured yet

16: Please note that Ga-MFI(238), Ga-MFI(95), and Ga-MFI(34) were not pristine but exposed to a previous conversion experiment as described in sidenote 14. Ga-MFI(13) was pristine and an additional NH_3-TPD to 600 °C was not performed due to its low catalytic activity.

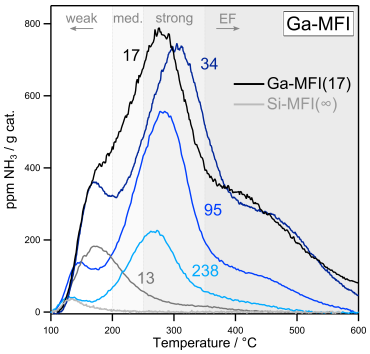

Figure 4.28: Overview of NH_3-TPD profiles of Ga-MFI catalysts with different Si/Ga ratios from sets 2 and 3. Si-MFI from set 1 shown as reference (light grey).

Different catalysts from sets 2 and 3 are compared and their NH_3-TPD profiles are shown in figure 4.28. All catalysts possess different strengths of acid sites,[15] ranging from weak acid sites with desorption temperatures below 200 °C to extra-framework acid sites with desorption temperatures above 350 °C. An overview of the sizes and desorption temperatures of the deconvoluted peaks is shown in table 4.12.[16]

At first glance, the acidity of the catalysts appears to align with their gallium content: higher Ga content equals lower Si/Ga equals higher acid site density. However, Ga-MFI(13) which has a large amorphous fraction only has an acid site density of 0.027 mmol g^{-1}. This explains why it was not active towards the aromatisation of 2,5-DMF. Furthermore, Ga-MFI(34) with an acidity of between 0.225 and 0.268 mmol g^{-1}, has more acid sites than Ga-MFI(238) and Ga-MFI(95), comprising 0.039 and 0.119 mmol g^{-1}, respectively. Unexpectedly, it also has more acid sites (on average) than Ga-MFI(17), which has 0.227 mmol g^{-1}. Potential reasons include the following:

1. Not all gallium atoms in Ga-MFI(17) result in an acid site. They could be present as different (extra-framework) species, potentially having synergy with other framework gallium atoms creating one strong acid site.
2. Different synthesis conditions of Ga-MFI(17), such as increased duration of the hydrothermal crystallisation step, resulted in different properties.
3. Gallium is part of different crystalline phases, such as gallium albite, albeit in small amounts since this was not detected with XRD.

Table 4.12: Analysis of the NH_3-TPD profiles right before and after the reaction of Ga-MFI with different Si/Ga ratios. Desorption peaks are grouped into weak (w, ≤200 °C), medium (m, 200 °C to 250 °C), strong (s, 250 °C to 350 °C) and extra-framework (ex, ≥350 °C) acid sites.

Sample Curve in 4.28	Ga-MFI(238) Light blue		Ga-MFI(95) Dark blue		Ga-MFI(17) Black		Ga-MFI(13) Dark grey	
	T/ °C	C/ mmol g^{-1}	T/ °C	C/ mmol g^{-1}	T/ °C	C/ mmol g^{-1}	T/ °C	C/ mmol g^{-1}
	135 w	0.004	154 w	0.013	174 w	0.029	164 w	0.010
	264 s	0.028	278 s	0.081	271 s	0.107	203 m	0.006
	383 ef	0.009	420 ef	0.026	403 ef	0.066	292 s	0.011
					549 ef	0.025		
total		**0.039**		**0.119**		**0.227**		**0.027**

4. Acid sites are not detected by ammonia molecules, perhaps there are inaccessible parts due to the catalyst's morphology.

Further acidity measurements could elucidate the different sites and explain the unequal role of gallium in the different catalysts. An example involves FTIR analysis after pyridine dosing, a probe molecule that shows a characteristic vibration when bound to a LAS or BAS.

The amount of benzene produced per acid site is displayed in table 4.13. Similar to what was previously observed, Ga-MFI(17) produces the maximum amount of benzene per acid site, with 7.4 molecules produced per acid site per hour. However, catalysts with relatively low acidity, such as Ga-MFI(238) and Ga-MFI(95), produce a correspondingly high amount of benzene per acid site. In other words, each acid site has a high turnover frequency and is active towards benzene production. The acid sites of a catalyst that has a high acid site density, like Ga-MFI(34), convert fewer benzene molecules per site.

Table 4.13: Overview of benzene production (in molecules per acid site per hour) over Ga-MFI catalysts with different Si/Ga ratios, normalised to acid site density. Si-MFI (∞_{Si}) is added as reference. For Ga-MFI(34), acid site density of 0.259 mmol g^{-1} is used. 600 ppm 2,5-DMF conversion at 500 °C for 1 h.

Sample Si/Ga	Benz. produced/ mole./(site·h)
∞_{Si}	0.621
238	1.079
95	3.248
34	2.057
17	7.401
13	0.497

This prompted the following question:
Why is each acid site able to produce more benzene in Ga-MFI(17) than in Ga-MFI(34)?

Besides the points mentioned before, one can focus on the environment of the acid sites. One influence that can play a major role in catalytic systems, especially in microporous catalysts, is the transfer of reagents and products to and from the active sites. Especially in this system, where most chemicals involved are of the same dimensions as the MFI-pores and thus diffusion-limited. Moreover, interacting forces between the surface and 2,5-DMF can slow down its transport and increase the time it takes to reach an active site and subsequently undergo conversion. This drawback can be overcome by the introduction of larger channels or pores, like mesopores, that aid mass transport and prevent mass transfer limitations.

reminder:
micro = ø < 2 nm
meso =2 nm ≤ ø≤ 50 nm
macro = ø > 50 nm

Therefore, two catalysts have been modified post-synthesis to implement mesopores: Ga-MFI(34)-meso and Ga-MFI(95)-meso.

Take-home message
Ga-MFI catalysts selectively convert 2,5-DMF to benzene at 500 °C and catalysts with a high gallium content produce more benzene (except for Ga-MFI(13)). Higher gallium content generally leads to an increased number of acid sites but not all acid sites are equally active for benzene production.

4.4 Influence of mesopores

The following section explores the degree of mesopore introduction and its influence on the catalytic properties and performance.

XRF

The following section explores the degree of mesopore introduction and its influence on the catalytic properties and performance. XRF results shown in table 4.14 reveal that the Si/Ga ratios are actually lower than in the parent catalysts: 81 and 27 compared to 95 and 34. This could be caused by catalyst desilication, induced by NaOH in the post-synthesis modification step.[17]

17: please note the nomenclature, Si/Ga ratios of the parent zeolites are used for clarity

Table 4.14: Elemental compositions of catalyst set 4, Ga-MFI(Si/Ga)-meso, measured with XRF. Oxygen wt% is derived by assuming metals to be present as oxides. H_2O determined by TGA at 200 °C. Normalised to a total weight percentage of 100 wt%

Sample	Si/Ga	Ga	Si	O	H_2O	Res.
				/wt%		
95-meso	81	1.4	45.1	53.2	1.5	0.18*
34-meso	27	3.9	42.8	52.4	2.4	0.61†

* K
* Al, K

XRD

XRD patterns (figure 4.29) confirm the preservation of the MFI-framework upon mesopore introduction.

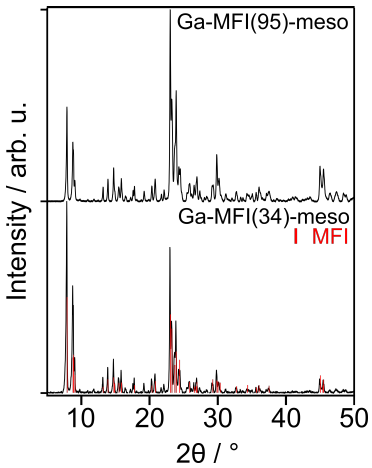

Figure 4.29: XRD patterns of set 4 catalysts, Ga-MFI(95)-meso and Ga-MFI(34)-meso. Background subtracted, normalised to highest intensity, and vertically displaced for clarity. Horizontally displaced with x=-0.19 to account for the sample height. Reference peak pattern of silicalite-1[162] (SiO_2, red, peaks higher than 5 % relative intensity shown).

As the introduction of mesopores depends on a dissolution-recrystallisation mechanism, Ga and Si species are mobilised in basic medium and then oriented around template molecules, TPA^+. Successive calcination of the template results in the formation of larger (meso) pores within and in between zeolite crystallites. It is paramount to know how much TPA^+ has been removed from the sample, as this indicates the added pore volume.

TGA and DSC

TGA and DSC were measured in air (figure 4.30) to measure the thermal stability of the final catalysts, H-Ga-MFI-meso (A), as well as measure the amount of removed TPA^+. TPA-Ga-MFI(34)-meso displays two small exothermic weight losses around 330 and 450 °C, the latter of around 1 wt%. Conversely, TPA-Ga-MFI(95)-meso displays a much larger weight loss of 3.5 wt% around 400 °C. This indicates a different and higher degree of dissolution and recrystallisation than in TPA-Ga-MFI(34)-meso since more TPA^+

is incorporated. The broad temperature range of the weight loss step indicates that TPA^+ is bound to the catalyst with different interaction strengths, possibly in different positions such as within and between particles.

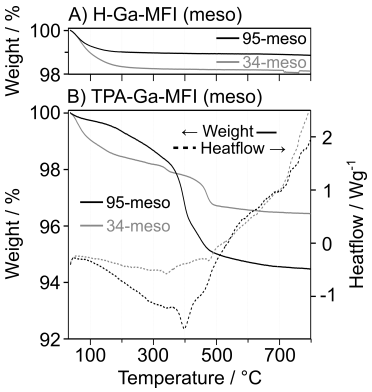

Figure 4.30: TGA and DSC profiles of catalysts from set 4 over a temperature range of 30 °C to 800 °C in 60 mL min^{-1} air (10 °C min^{-1}). H-Ga-MFI (A) and TPA-Ga-MFI (B).

Physisorption

Nitrogen and argon physisorption was performed to determine the textural properties of the catalyst including the surface area and pore volume (figure 4.31). The nitrogen isotherms ((black and grey curves) resemble a composite of type I and type IV, as was seen for their microporous counterparts.[18] However, clear differences can be seen with the microporous catalysts (figure 4.18) in the size of the hysteresis loops (type H1 and H4) between p/p_0=0.5 and p/p_0=1.0: the size of the desorbed nitrogen is 2 to 5 times as large in the mesoporous samples. Introduction of the mesopores only increases the size of the hysteresis loops but not the shape of the isotherms, which suggests that mesopores have been formed in between crystallites or crystal aggregates.

18: Type I and IV are typical for microporous materials with large micro- or mesopores between zeolites [112].

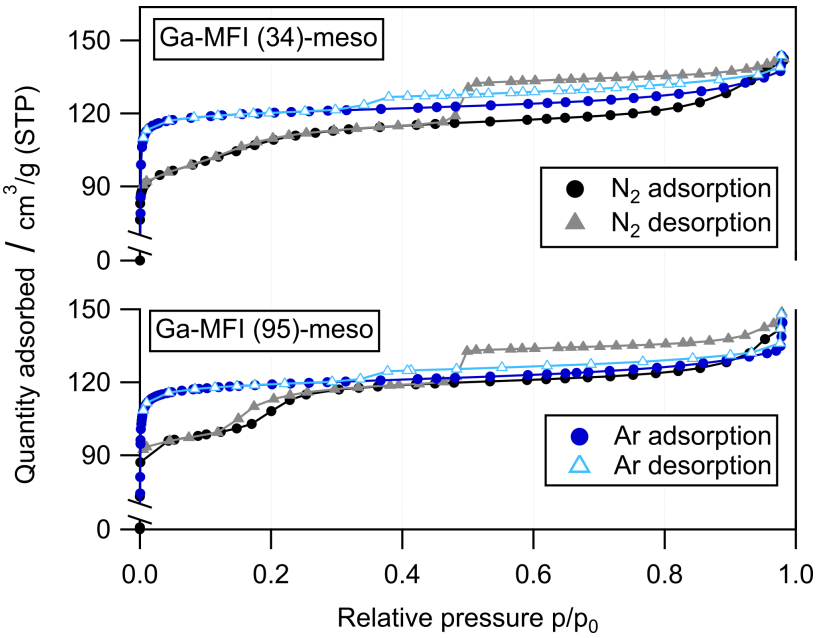

Figure 4.31: N_2-physisorption isotherms at 77K of the catalyst set 4. Nitrogen adsorption (circles, black) and desorption (triangles, grey).

Similarly, the argon physisorption isotherms (blue curves) of the mesoporous samples show larger hysteresis loops as well, confirming the difference in pore size and structure.[19]

The textural properties are shown in table 4.15 and when comparing mesoporous samples with their microporous counterparts (table 4.9), the apparent surface areas of the mesoporous samples are smaller: 398 and 435 $m^2\ g^{-1}$ for Ga-MFI(95)-meso and -micro, respectively, and 401 and 420 $m^2\ g^{-1}$ for Ga-MFI(34)-meso and -micro. No trends were observed for the microporous volume, as

19: argon physisorption was measured on the microporous samples as well (set 2) but this is not displayed.

it increased for Ga-MFI(95)-meso and decreased for Ga-MFI(34)-meso. The decrease in SA can be explained by the post-synthesis modification of implementing mesopores,[20] which are created by dissolution of existing microporous sections.

20: mesopores contain more empty, connected space than micropores so less SA per volume catalyst

Table 4.15: Textural properties of catalyst set 4, Ga-MFI(Si/Ga)-meso, derived from nitrogen and argon isotherms.

Sample	Ads.	SA* / $m^2\ g^{-1}$	$S^{\dagger}_{micro}$ / $m^2\ g^{-1}$	$S^{\dagger}_{ext}$ / $m^2\ g^{-1}$	$V^{\dagger}_{micro}$ / $m^3\ g^{-1}$
95-meso	N_2	398	375	23	0.170
	Ar	429	414	15	0.146
34-meso	N_2	401	377	26	0.164
	Ar	436	421	15	0.148

* apparent surface areas by BET method, p/p_0 = 0.002-0.05, following consistency criteria [109]
† by t-plot method (Harkins and Jura equation, t= 5.0 - 8.0 Å)

Take-home message
Mesopores have been successfully introduced into Ga-MFI catalysts, presumably in between crystals as was determined by Ar and N_2-physisorption. TGA and DSC identified some differences among the samples, although both the MFI framework and their microporous character were preserved.

4.4.1 Catalytic tests

The catalytic performance of the mesoporous catalysts has been tested and the conversion of 2,5-DMF and the selectivities of the main products over Ga-MFI(34)-meso are shown in figure 4.32, together with (microporous) Ga-MFI(34) for reference.

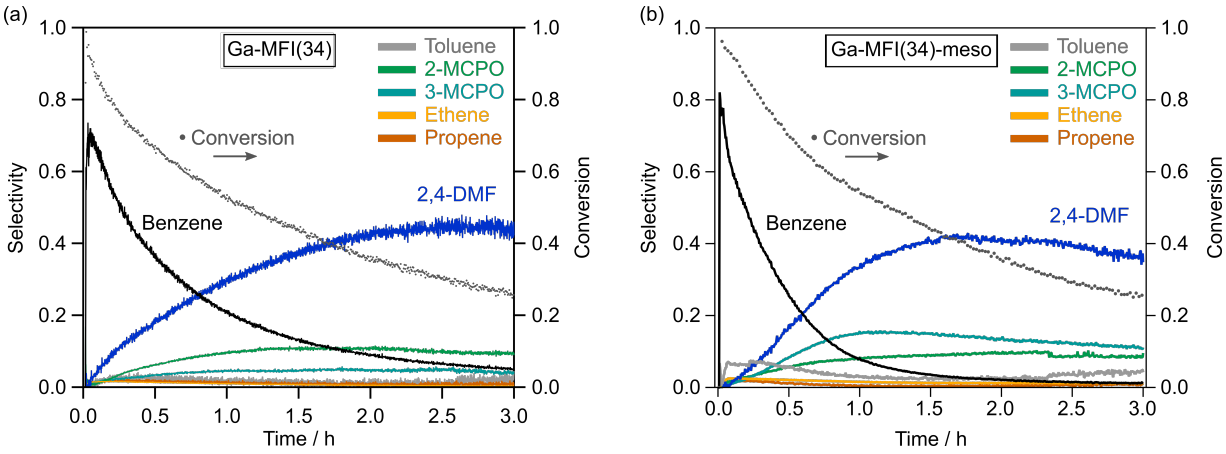

Figure 4.32: Conversion of 2,5-DMF and selectivities towards the main products during a 3 h conversion reaction of 600 ppm 2,5-dimethylfuran over Ga-MFI(34) and Ga-MFI(34)-meso at 500 °C.

The mesoporous sample displays a slightly higher initial selectivity towards benzene of nearly 80 %, as well as an increased conversion. Moreover, toluene has been formed in low amounts which could mean that the bigger pores allow for the production of larger aromatics. Contrary to what was expected, the mesoporous catalyst produced benzene for only 1.5 h, even though the induced mesopores are thought to assist with the transfer of reagents and products, which effectively could increase catalyst lifetime. This reduction in catalyst lifetime can be caused by the following reasons:

- The mesopore introduction was not successful
  - Physisorption measurements dispute this but further sorption experiments performed on vacuum-dried catalysts can allow for the determination of the pore size distribution. Moreover, large meso- and macropores may be visible with SEM or transmission electron microscopy (TEM).
- The mesopore introduction adversely affects the structure of the catalysts including the micropores and active sites.
  - This can be tested by performing NH_3-TPD, as shown in the section below.
- The mesopores allow for the formation of different carbonaceous species that deactivate the active sites.
  - Analysis of the formed coke, e.g., through TPO, TGA, or extraction with HF, can identify different sizes of formed hydrocarbons [173].

On the contrary, the production of the isomerisation products seems to follow a similar behaviour in both mesoporous samples as in their microporous counterparts. After roughly 1 h, the selectivity shifts 2,4-DMF, 2-MCPO, and 3-MCPO and these are still formed after 3 h TOS.

Ga-MFI(95)-meso showed a similar product distribution (not shown), with slightly lower conversion and selectivities towards aromatics. The measured benzene concentrations are shown in figure 4.33, where they are compared to the microporous samples. Both mesoporous samples (black and grey curves) demonstrate increased benzene production during the first 30 minutes after which the benzene signal drops slightly below their respective microporous counterparts. This initial increase can be caused by the increase in gallium content, as XRF results determined Si/Ga ratios of 27 and 81 instead of 34 and 95 for Ga-MFI(34)-meso and Ga-MFI(95)-meso, respectively. An increase in gallium content correlated to an increase in the acid site density in catalyst set 2, for Ga-MFI: More acid sites are able to produce more benzene. To

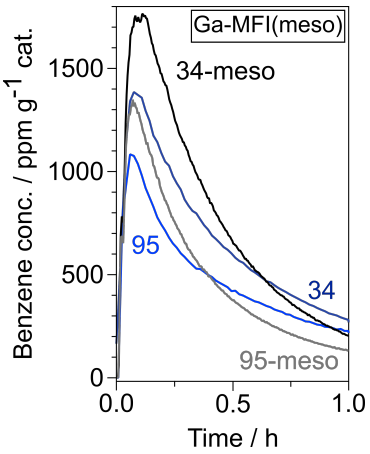

Figure 4.33: Overview of benzene production by Ga-MFI catalysts with mesopores from set 4 (black and grey curves), and micropores from set 2 (dark and light blue curves).

Table 4.16: Analysis of the NH_3-TPD profiles right before and after 3 h reaction at 500 °C of Ga-MFI-meso with different Si/Ga ratios. Desorption peaks are grouped into weak (w, ≤200 °C), medium (m, 200 °C to 250 °C), strong (s, 250 °C to 350 °C) and extra-framework (ex, ≥350 °C) acid sites.

Sample	Ga-MFI(95)-meso		Ga-MFI(34)-meso	
	T/ °C	C/ mmol g^{-1}	T/ °C	C/ mmol g^{-1}
Fresh	153 w	0.006	159 w	0.025
	257 s	0.026	218 m	0.060
	332 s	0.024	303 s	0.042
total		**0.056**		**0.127**
Spent	138 w	0.001	148 w	0.005
	173 w	0.004	183 w	0.008
	261 s	0.003	262 s	0.013
total		**0.007**		**0.026**

test if this holds up for Ga-MFI-meso as well, NH_3-TPD has been performed.

An overview of the desorption peaks is shown in table 4.16. The measured number of acid sites of the fresh mesoporous samples is substantially lower than their microporous counterparts, with 0.056 vs 0.119 mmol g^{-1} for Ga-MFI(95)-meso and -micro, respectively, and 0.127 vs 0.268* mmol g^{-1} for Ga-MFI(34). Although the mesoporous samples have a higher gallium content, they have lost more than half of their acid sites. This indicates that the environment of the gallium atoms changed during the modification step; framework gallium atoms may potentially migrate and form extra-framework gallium clusters or other gallium species. These species may not be involved in forming an acid site or they may synergistically interact with e.g., framework gallium, forming strong acid sites that promote benzene formation [151].

*potentially even higher since the NH_3-TPD was performed up to 550 °C

Even though the production of benzene becomes lower in the mesoporous samples than the microporous samples after 1 h, the total amount of benzene produced in this hour is slightly higher. To illustrate, the benzene produced in the first hour TOS is 0.395 mmol for Ga-MFI(95)-meso and 0.387 mmol for Ga-MFI(95), and 0.625 vs 0.533 mmol for Ga-MFI(34)-meso and -micro, respectively (table 4.17). Future experiments and calculations can focus on the long-term production of aromatics.

The superior performance of the mesoporous catalysts is further highlighted when the benzene production is normalised to the number of acid sites (table 4.17, column 3). Ga-MFI(95)-meso displays an average production of 7.047 molecules benzene per acid site during 1 h compared to 3.248 molecules benzene for Ga-MFI(95); an increase of 117 %. Likewise, the conversion of Ga-MFI(34)-meso of 4.904 molecules has increased by 138 % from 2.057 molecules benzene. In other words, the acid sites of the mesoporous catalysts are more active in the conversion of 2,5-DMF

Sample Si/Ga	Benz. prod./ mmol/(g·h)	Benz. prod./ molecules/(acid site·h)
95-meso	0.395	7.047
34-meso	0.625	4.904

Table 4.17: Overview of benzene production over Ga-MFI-meso catalysts with different Si/Ga ratios, normalised to catalyst amount and acid site density. 600 ppm 2,5-DMF conversion at 500 °C for 1 h.

to aromatics, such as benzene. This confirms the hypothesis of an increased activity of each acid site due to improvements in mass transport.

When reconsidering the potential reasons for a decreased lifetime of the mesoporous catalysts, the post-synthesis modification of mesopore introduction appears to have severely afflicted the number of acid sites present. Further studies can optimise mesopore introduction by using lower temperatures, shorter recrystallisation times, and more dilute solutions. Moreover, ideal catalyst design involves a one-step bottom-up synthesis of mesoporous Ga-MFI catalysts with a high acid site density.

Take-home message
Mesoporous catalysts display a slightly increased short-term benzene selectivity and production compared to their microporous counterpart. The introduction of mesopores resulted in a decrease in acid site density of more than twofold, whereas the activity of each acid site increased by more than twofold.

Conclusions and future work 5

To summarise, this thesis has investigated the performance of different zeolitic catalysts in the conversion of 2,5-dimethylfuran into aromatics. Besides the influence of temperature, several properties of the catalysts have been identified to influence their catalytic behaviour, such as the choice of the incorporated metal, the amount of incorporated gallium, and the influence of additional mesopores.

Starting with the choice of incorporated metal, MFI-framework catalysts have been synthesised with incorporated aluminium and gallium. Catalytic testing of Al-MFI catalysts revealed an initial complete conversion of 2,5-DMF and high initial selectivities towards benzene (≥40 %) and toluene (≥10 %), but the production of the aromatic rapidly decreased with increasing TOS. On the contrary, Ga-MFI catalysts demonstrated superior initial benzene selectivity (≥70 %) as well as an increased catalyst lifetime, maintaining 10 % benzene selectivity after 5 h at 500 °C. With increasing TOS, the selectivities shift from aromatics to isomerisation products such as 2,4-DMF, 2-MCPO, and 3-MCPO, suggesting that the latter initially act as intermediates for aromatics. Acid site analysis determined that strong and extra-framework acid sites are responsible for aromatisation reactions, which are deactivated by coking, whereas weak acid sites catalyse isomerisation reactions.

The reaction can be tuned towards the selective production of 2,4-DMF over Ga-MFI when the operating temperatures are decreased to between 300 and 400 °C. Conversions of 30 and 20 % have been observed for 375 and 350 °C, respectively. At 350 °C, initial 2,4-DMF selectivities reach 80 % down to 75 % after 2 h TOS.

The influence of the gallium content has been tested through analysis of a series of Ga-MFI catalysts with different Ga contents. Increasing the gallium content also was proven to increase the conversion of 2,5-DMF and selectivity towards aromatics, such as benzene. However, the amount of Ga that can be successfully incorporated is limited to a Si/Ga ratio of 13, at which the catalyst has become partially amorphous and lost its catalytic activity. Tuning the synthesis conditions by increasing the crystallisation duration may improve the formation of MFI but phase impurities may also be formed.

The amount of incorporated gallium is positively correlated to its number of acid sites and its catalytic performance. However, Ga-MFI(17), which has twice as much gallium as Ga-MFI(34), possessed a lower number of acid sites which suggests that gallium is not

only present in the MFI framework but also as extra-framework species, such as gallium oxides, nanoparticles, or clusters.

The morphology and pore size of the catalysts have successfully been altered by the post-synthesis introduction of mesopores in two Ga-MFI catalysts. Structural analysis determined an increase in the amount of interparticle mesopores while retaining the MFI-framework, at the expense of more than half of its number of acid sites.

The mesoporous catalysts demonstrated an increased short-term benzene selectivity and production but similar deactivation behaviour, suggesting that its lifetime has not been improved. However, since only half of the acid sites were left compared to the microporous catalysts, each active site was more than twice as active for benzene production in the mesoporous samples. This advocates that the mass transport of reactants and products is facilitated by the mesopores.

5.1 Future directions

After demonstrating the superior performance of Ga-MFI in the aromatisation of 2,5-DMF, future studies can focus on understanding the role of gallium in more detail, as well as focus on the design of different catalysts.

The synthesis of the catalysts can be optimised to prevent the formation of additional phases such as quartz and gallium albite, for example by lowering the crystallisation temperature or duration. The introduction of mesopores can be performed under milder conditions to preserve as many acid sites as possible.

The catalysts that were presented in this thesis can also be studied in more detail. For example, argon physisorption at 83 K could provide more reliable sorption data than Ar at 77 K, and pretreatment of the catalyst at elevated temperatures under vacuum could assure the complete removal of water from the pores. In-depth analysis of the crystallinity of the samples by measuring a standard will allow for the quantification of different phases present and performing scXRD will allow derivation of the unit cell. SAXS will provide more information on the size of the mesopores.

Regarding the nature of the gallium species, X-ray absorption spectroscopy (XAS) can provide insights regarding the local environment of the gallium species, e.g., coordination number and oxidation state, leading to the determination of the structure of the active sites.

ssNMR spectroscopy of gallium or silicon can provide insights into unit cell expansions and confirm incorporation of gallium in the framework. Under certain conditions, tetrahedrally and octahedrally bound gallium may be discriminated.

Besides studying Ga-MFI, other porous materials may be investigated such as large-pore zeolites with the BEA or FAU framework. This will allow to ascertain the importance of the pore confinement in MFI, or perhaps enhance aromatisation reactions due to an increased lifetime of the catalyst.

Although the groundwork of this catalytic system has been laid in this thesis, much is yet to be discovered. Elucidating the reaction mechanism and identifying the relevant catalytic descriptors will aid future catalyst design.

Acknowledgements

The work presented in this thesis was carried out at the Division of Applied Chemistry at the Department of Chemistry and Chemical Engineering at Chalmers University of Technology.

Analysis of the catalysts was also carried out at the Chalmers Materials Analysis Laboratory (CMAL). The access to instrumentation and assistance is gratefully acknowledged.

This work was funded by the Swedish Energy Agency via the project Green commodity chemicals (Project No 48569-1). The financial support is gratefully acknowledged.

I want to express my sincere gratitude to my main supervisor Per-Anders Carlsson. The freedom I have to explore different research directions within the project is much appreciated, as well as the support and guidance you provide.

I also would like to thank my co-supervisors Andreas Schaefer and Anders Hellman. Andreas, your daily supervision and expertise are much appreciated, as well as your personal and academic tutoring. Anders, thank you for joining the team and I look forward to our future collaborations.

I would like to thank the following people,

My examiner Hanna Härelind for evaluating my research progress and leading our department.

Jerker Mårtensson for joining my licentiate defence as a discussion leader.

Christopher Sauer for his guidance and support, especially your help with many practicalities when I first started the project. I thoroughly enjoyed working together, and wish you the best on your new adventure.

Felix Hemmingsson for his helpful demeanour and his contributions to our scientific discussions, as well as current and former group members Oscar Hellgren, Alexander Nellessen, Yanyue Feng, and Mengqiao Di.

Simone Creci for providing catalyst samples.

All members of Applied Chemistry for the great working environment. I am grateful to consider many of you not only my colleagues but also my friends.

Last but not least, I would like to thank my family and friends abroad. The hardest part of this project has been missing you. Special thanks to Karlijn for your love and support ♥

Guido J.L. de Reijer, Göteborg, September 2023

Bibliography

(1) United Nations, *World Population Prospects*, 2017, https://population.un.org/wpp/ (cit. on p. 1).

(2) Macrotrends, *World Population Growth Rate 1950-2023*, https://www.macrotrends.net/countries/WLD/world/population-growth-rate (cit. on p. 1).

(3) P. A. Owusu and S. Asumadu-Sarkodie, *Cogent Engineering*, 2016, **3** (cit. on p. 1).

(4) Gapminder, *World population: UN future forecast*, 2017, https://www.gapminder.org/topics/population-forecasts/ (cit. on p. 1).

(5) P. P. Groumpos, *IFAC-PapersOnLine*, 2021, **54**, 464–471 (cit. on p. 1).

(6) C. N. Daggett, *The Birth of Energy*, Duke University Press, 2019, p. 280 (cit. on p. 1).

(7) D. Bodansky, *Nuclear energy: Principles, practices, and prospects*, Springer, 2nd edn., 2004 (cit. on p. 1).

(8) M. Xu, J. M. David and S. H. Kim, *International Journal of Financial Research*, 2018, **9**, 90–95 (cit. on p. 1).

(9) L. Dogaru, 13th International Conference Interdisciplinarity in Engineering (INTER-ENG 2019), Elsevier, 2020, vol. 46, pp. 397–401 (cit. on p. 1).

(10) International Energy Agency (IEA), *World Energy Balances 2022 Edition - Database Documentation*, tech. rep., 2022 (cit. on p. 1).

(11) M. Kampa and E. Castanas, *Environmental Pollution*, 2008, **151**, 362–367 (cit. on p. 1).

(12) W. Fulkerson, R. R. Judkins and M. K. Sanghvi, 1990, **263**, 128–135 (cit. on p. 1).

(13) C. Bauer, K. Treyer, T. Heck and S. Hirschberg, in *Encyclopedia of the Anthropocene*, 2017, vol. 1-5, pp. 473–484 (cit. on p. 1).

(14) Y. Hirabayashi et al., *Nature Climate Change*, 2013, **3**, 816–821 (cit. on p. 1).

(15) P. Stott, *Science*, 2016, **352**, 1517–1518 (cit. on p. 1).

(16) J. Spinoni, J. V. Vogt, G. Naumann, P. Barbosa and A. Dosio, *International Journal of Climatology*, 2018, **38**, 1718–1736 (cit. on p. 1).

(17) C. D. Thomas et al., *Nature*, 2004, **427**, 145–148 (cit. on p. 1).

(18) R. C. Robbins and E. Robinson, *American Petroleum Institute* (cit. on p. 1).

(19) National Centers for Environmental Information, *Global Time Series - Climate at a Glance*, https://www.ncei.noaa.gov/access/monitoring/climate-at-a-glance/global/time-series/globe/land_ocean/ytd/5/1968-2023?trend=true&trend_base=100&begtrendyear=1968&endtrendyear=2023 (cit. on p. 2).

(20) CO2 Earth, *Daily CO2*, https://www.co2.earth/daily-co2 (cit. on p. 2).

(21) U.S. Global Change Research Program, *Climate science special report: Fourth national climate assessment, volume I*, tech. rep., U.S. Global Change Research Program, 2018, p. 470 (cit. on p. 2).

(22) G. H. Brundtland et al., *Medicine and War*, 1988, **4**, 17–25 (cit. on p. 2).

(23) I. Dincer, *Renewable & sustainable energy reviews*, 2000, **4**, 157–175 (cit. on p. 2).

(24) O. Ellabban, H. Abu-Rub and F. Blaabjerg, *Renewable and Sustainable Energy Reviews*, 2014, **39**, 748–764 (cit. on p. 2).

(25) World Economic Forum, *The Speed of the Energy Transition Gradual or Rapid Change? [White paper]*, tech. rep. September, 2019, p. 32 (cit. on p. 2).

(26) UNFCC, *The Paris Agreement*, tech. rep., 2015, p. 18 (cit. on p. 2).

(27) UNFCC, *The Glasgow Climate Pact – Key Outcomes from COP26 | UNFCCC*, tech. rep. (cit. on p. 2).

(28) United Nations, *What is renewable energy?*, 2023, https://www.un.org/en/climatechange/what-is-renewable-energy (cit. on p. 2).

(29) R. A. Berner, *Nature*, 2003, **426**, 323–326 (cit. on p. 2).

(30) P. Mann, L. Gahagan and M. B. Gordon, in *AAPG Memoir*, American Association of Petroleum Geologists Memoir, 2005, ch. 2, pp. 15–105 (cit. on p. 2).

(31) J. G. Speight, in *Environmental Organic Chemistry for Engineers*, Butterworth-Heinemann, 2017, pp. 43–86 (cit. on p. 3).

(32) C. M. Lok, J. Van Doorn and G. Aranda Almansa, *Renewable and Sustainable Energy Reviews*, 2019, **113**, 109248 (cit. on pp. 3, 5).

(33) C. Jaiswal, *Aromatic Market Research Report Information By Type (P-Xylene, O-Xylene, Toluene, Benzene, and Others), By Application (Additive and Solvent), By Industry (Paint & Coatings, Adhesives, Pharmaceuticals, Chemicals, and Others), and By Region (North America*, tech. rep., Chitranshi_2023, 2023 (cit. on p. 5).

(34) J. L. Pellegrino, *Energy and Environmental Profile of the U.S. Chemical industry*, tech. rep., 2000 (cit. on p. 5).

(35) S. Matar and L. F. Hatch, in *Chemistry of Petrochemical Processes*, 2001, pp. 262–300 (cit. on p. 5).

(36) M. Bender, *New Technologies and Alternative Feedstocks in Petrochemistry and Refining DGMK Conference*, 2013, 59–65 (cit. on p. 5).

(37) D. A. Bulushev and J. R. Ross, *Catalysis Today*, 2011, **171**, 1–13 (cit. on p. 5).

(38) A. V. Bridgwater, *Applied Catalysis A, General*, 1994, **116**, 5–47 (cit. on p. 5).

(39) R. W. Thring, S. P. Katikaneni and N. N. Bakhshi, *Fuel processing technology*, 2000, **62**, 17–30 (cit. on p. 5).

(40) A. C. Hansen, N. Clarke and A. W. Hegnes, *Energy, Sustainability and Society*, 2021, **11**, 1–23 (cit. on p. 5).

(41) A. Lindfors and R. Feiz, *The current Nordic biogas and biofertilizer potential : An inventory of established feedstock and current technology*, tech. rep., 2023, p. 28 (cit. on p. 5).

(42) European Union, *Eurostat Online Database*, 2020, http://ec.europa.eu/eurostat/data/database (cit. on p. 5).

(43) X. Zhou, L. J. Broadbelt and R. Vinu, in *Advances in Chemical Engineering*, Academic Press, 2016, vol. 49, pp. 95–198 (cit. on p. 6).

(44) T. Werpy and G. Petersen, *US NREL*, 2004 (cit. on p. 6).

(45) S. H. Shinde, A. Hengne and C. V. Rode, in *Biomass, Biofuels, Biochemicals: Recent Advances in Development of Platform Chemicals*, Elsevier B.V., 2019, pp. 1–31 (cit. on p. 6).

(46) Y. T. Cheng and G. W. Huber, *ACS Catalysis*, 2011, **1**, 611–628 (cit. on pp. 6, 21).

(47) Y. T. Cheng and G. W. Huber, *Green Chemistry*, 2012, **14**, 3114–3125 (cit. on p. 6).

(48) E. A. Uslamin et al., *ACS Catalysis*, 2019, **9**, 8547–8554 (cit. on p. 6).

(49) E. A. Uslamin et al., *Chemical Engineering Science*, 2019, **198**, 305–316 (cit. on p. 6).

(50) S. Dutta and N. S. Bhat, *Biomass Conversion and Biorefinery*, 2020 (cit. on pp. 6, 20).

(51) J. G. Calvert, *Pure and Applied Chemistry*, 1990, **62**, 2167–2219 (cit. on p. 6).

(52) K. Laidler, *Pure and Applied Chemistry*, 1996, **68**, 149–192 (cit. on pp. 6, 7).

(53) P. E. V. Paul, V. Sangeetha and R. G. Deepika, *Emerging trends in the industrial production of chemical products by microorganisms*, Academic Press, 2018, pp. 107–125 (cit. on p. 7).

(54) P. van Leeuwen, *Homogeneous Metal Catalysis*, Elsevier, 2016 (cit. on p. 7).

(55) R. Di Monte, J. Kašpar and E. Farnetti, *Homogeneous and heterogeneous catalysis*, 2009 (cit. on p. 7).

(56) T. K. Sherwood, *Pure and Applied Chemistry*, 1965, **10**, 595–610 (cit. on p. 7).

(57) T. C. Ong, R. Verel and C. Copéret, in *Encyclopedia of Spectroscopy and Spectrometry*, Academic Press, 2016, pp. 121–127 (cit. on p. 8).

(58) G. Ertl, H. Knözinger and J. Weitkamp, *Handbook of Heterogeneous Catalysis*, ed. G. Ertl, H. Knözinger and J. Weitkamp, Wiley, 2008, vol. 1-5 (cit. on p. 8).

(59) X. Hu and A. C. K. Yip, *Frontiers in Catalysis*, 2021, **1**, 667675 (cit. on p. 8).

(60) K. Li, H. Wang and Y. Wei, *Journal of Chemistry*, 2013 (cit. on p. 8).

(61) C. Baerlocher and L. B. McCusker, *Database of Zeolite Structures*, http://www.iza-structure.org/databases/ (cit. on pp. 8, 9, 30).

(62) K. S. Sing et al., *Pure and Applied Chemistry*, 1985, **57**, 603–619 (cit. on pp. 8, 31).

(63) J. Haber, *Pure and Applied Chemistry*, 1991, **63**, 1227–1246 (cit. on p. 8).

(64) V. Komvokis, L. X. L. Tan, M. Clough, S. S. Pan and B. Yilmaz, in *Zeolites in Sustainable Chemistry: Synthesis, Characterization and Catalytic Applications*, Springer Berlin Heidelberg, 2015, pp. 271–297 (cit. on p. 8).

(65) J. L. White, in *Catalysis Science and Technology*, Royal Society of Chemistry, 2011, vol. 1, pp. 1630–1635 (cit. on p. 8).

(66) M. B. Park, E. D. Park and W. S. Ahn, *Frontiers in Chemistry*, 2019, **7**, 1–7 (cit. on p. 8).

(67) R. D. Shannon et al., *Journal of Physical Chemistry*, 1985, **89**, 4778–4788 (cit. on p. 8).

(68) M. Ravi, V. L. Sushkevich and J. A. van Bokhoven, *Chemical Science*, 2021, **12**, 4094–4103 (cit. on p. 8).

(69) R. D. Shannon, *Acta Crystallographica Section A*, 1976, **32**, 751–767 (cit. on p. 9).

(70) A. Karttunen and L. Tong, *Zeolites in catalysis - Aalto University wiki*, https://wiki.aalto.fi/display/SSC/Zeolites+in+catalysis#cite-summary-8-2 (cit. on p. 10).

(71) R. Szostak, *Molecular sieves — principles of synthesis and identification*, 1989, vol. 213, p. 325 (cit. on p. 10).

(72) C. D. Baertsch, H. H. Funke, J. L. Falconer and R. D. Noble, *Journal of Physical Chemistry*, 1996, **100**, 7676–7679 (cit. on p. 10).

(73) J. Jae et al., *Journal of Catalysis*, 2011, **279**, 257–268 (cit. on p. 10).

(74) F. D. Magalhães, R. L. Laurence and W. C. Conner, *Journal of Physical Chemistry B*, 1998, **102**, 2317–2324 (cit. on p. 10).

(75) L. Song, Z. L. Sun, H. Y. Ban, M. Dai and L. V. Rees, *Physical Chemistry Chemical Physics*, 2004, **6**, 4722–4731 (cit. on p. 10).

(76) H. Shi, A. N. Migues and S. M. Auerbach, *Green Chemistry*, 2014, **16**, 875–884 (cit. on p. 10).

(77) J. Gancedo, L. Faba and S. Ordóñez, *Applied Catalysis A: General*, 2022, **641**, 118683 (cit. on p. 10).

(78) B. F. Mentzen and P. Gelin, *Materials Research Bulletin*, 1995, **30**, 373–380 (cit. on p. 10).

(79) S. Caro-Ortiz, E. Zuidema, M. Rigutto, D. Dubbeldam and T. J. Vlugt, *Journal of Physical Chemistry C*, 2020, **124**, 24488–24499 (cit. on p. 10).

(80) S. Creci, X. Wang, P. A. Carlsson and M. Skoglundh, *Topics in Catalysis*, 2019, **62**, 689–698 (cit. on pp. 13, 18, 32).

(81) R. Szostak, V. Nair and T. L. Thomas, *Journal of the Chemical Society, Faraday Transactions 1: Physical Chemistry in Condensed Phases*, 1987, **83**, 487–494 (cit. on p. 13).

(82) W. Zhang, B. Wang, P. Rui, N. Fan and W. Liao, *Catalysis Letters*, 2021, **151**, 2716–2723 (cit. on p. 16).

(83) A. H. Boonstra and J. M. Baken, *Journal of Non-Crystalline Solids*, 1990, **122**, 171–182 (cit. on p. 16).

(84) J. E. Lofgreen and G. A. Ozin, *Chemical Society Reviews*, 2014, **43**, 911–933 (cit. on pp. 16, 17).

(85) C. J. Brinker, *Journal of Non-Crystalline Solids*, 1988, **100**, 31–50 (cit. on p. 16).

(86) N. V. Roik and L. A. Belyakova, *Journal of Solid State Chemistry*, 2013, **207**, 194–202 (cit. on p. 16).

(87) C. Colleoni et al., *Physical Chemistry Chemical Physics*, 2016, **18**, 772–780 (cit. on p. 16).

(88) G. J. Owens et al., *Progress in Materials Science*, 2016, **77**, 1–79 (cit. on p. 16).

(89) M. A. Camblor, A. Corma and S. Valencia, *Chemical Communications*, 1996, 2365–2366 (cit. on p. 17).

(90) X. Li et al., *Microporous and Mesoporous Materials*, 2020, **305**, 110346 (cit. on p. 17).

(91) T. Montheil, C. Echalier, J. Martinez, G. Subra and A. Mehdi, *Journal of Materials Chemistry B*, 2018, **6**, 3434–3448 (cit. on p. 18).

(92) C. J. Brinker and G. W. Scherer, *Sol-Gel Science: The Physics and Chemistry of Sol-Gel Processing*, Academic Press, Inc., 1st edn., 1990 (cit. on p. 18).

(93) Z. Gabelica and S. Valange, *Microporous and Mesoporous Materials*, 1999, **30**, 57–66 (cit. on p. 18).

(94) X. Yang et al., *Microporous and Mesoporous Materials*, 2022, **329** (cit. on p. 18).

(95) C. Sauer, Ph.D. Thesis, Chalmers University of Technology, 2021 (cit. on pp. 19, 20).

(96) C. Sauer, A. Lorén, A. Schaefer and P. A. Carlsson, *Analytical Chemistry*, 2021, **93**, 13187–13195 (cit. on pp. 19, 20, 80).

(97) K.Leiter, J.Hirber, M.Andriollo and W.Lindinger, *IMR-MS (Ion-Molecule-Reaction Mass-Spectrometry) - A diagnostic tool for analysis of gaseous components*, tech. rep., 1991 (cit. on p. 20).

(98) W. Lindinger, J. Hirber and H. Paretzke, *International Journal of Mass Spectrometry and Ion Processes*, 1993, **129**, 79–88 (cit. on p. 20).

(99) M. Munson and F. Field, *Journal of The American Chemical Society*, 1966, **88**, 2621–2630 (cit. on p. 20).

(100) S. Lin and C. W. Dence, *Comparative Biochemistry and Physiology Part B: Comparative Biochemistry*, 1993, **105**, ed. S. Y. Lin and C. W. Dence, 422 (cit. on p. 20).

(101) H. W. Siesler, 2002, 348 (cit. on p. 20).

(102) E. A. Uslamin, N. A. Kosinov, E. A. Pidko and E. J. Hensen, *Green Chemistry*, 2018, **20**, 3818–3827 (cit. on p. 21).

(103) W. H. Bragg and W. L. Bragg, *Proceedings of the Royal Society of London. Series A, Containing Papers of a Mathematical and Physical Character*, 1913, **88**, 428–438 (cit. on p. 21).

(104) M. Ermrich and D. Opper, *X-RAY Powder Diffraction for the analyst*, 2011 (cit. on pp. 22, 23).

(105) L. Ge, W. Lai and Y. Lin, *X-Ray Spectrometry*, 2005, **34**, 28–34 (cit. on p. 23).

(106) I. Langmuir, *Journal of the American Chemical Society*, 1918, **40**, 1361–1403 (cit. on p. 24).

(107) S. Brunauer, P. H. Emmett and E. Teller, *J. Am. Chem. Soc.*, 1938, **60**, 309–319 (cit. on p. 24).

(108) K. S. Sing, *Advances in Colloid and Interface Science*, 1998, **76-77**, 3–11 (cit. on p. 24).

(109) J. Rouquerol, P. Llewellyn and F. Rouquerol, *Studies in Surface Science and Catalysis*, 2007, **160**, 49–56 (cit. on pp. 24, 31, 46, 51, 58).

(110) K. S. Sing, *Journal of Porous Materials*, 1995, **2**, 5–8 (cit. on p. 24).

(111) Y. S. Bae, A. Ö. Yazayd'n and R. Q. Snurr, *Langmuir*, 2010, **26**, 5475–5483 (cit. on p. 24).

(112) M. Thommes et al., *Physisorption of gases, with special reference to the evaluation of surface area and pore size distribution (IUPAC Technical Report)*, tech. rep. 9-10, 2015, pp. 1051–1069 (cit. on pp. 24, 25, 31, 45, 46, 51, 52, 57).

(113) J. W. M. Osterrieth et al., *Advanced Materials*, 2022, **2201502**, 2201502 (cit. on p. 24).

(114) K. Sing, Colloids and Surfaces A: Physicochemical and Engineering Aspects, 2001, vol. 187-188, pp. 3–9 (cit. on pp. 24, 31, 46).

(115) G. Jura and W. D. Harkins, *Journal of the American Chemical Society*, 1944, **66**, 1356–1362 (cit. on p. 24).

(116) T. Sakaki, *Bulletin of the Chemical Society of Japan*, 1953, **26**, 213–218 (cit. on p. 24).

(117) J. H. de Boer et al., *Journal of Colloid And Interface Science*, 1966, **21**, 405–414 (cit. on p. 24).

(118) S. W. Thomson, *Philosophical Magazine*, 1871, **42**, 448–452 (cit. on p. 24).

(119) E. G. Derouane, J. M. Andre and A. A. Lucas, *Journal of Catalysis*, 1988, **110**, 58–73 (cit. on p. 24).

(120) A. Galarneau, F. Villemot, J. Rodriguez, F. Fajula and B. Coasne, *Langmuir*, 2014, **30**, 13266–13274 (cit. on pp. 24, 25).

(121) L. Desmurs et al., *ChemNanoMat*, 2022, **8** (cit. on pp. 24, 51).

(122) F. Rouquerol, J. Rouquerol, K. Sing, P. Llewellyn and G. Maurin, *Adsorption by powders and porous solids: Principles, Methodology and Applications*, Academic Press, 2nd edn., 2014, p. 631 (cit. on pp. 25, 31, 46).

(123) S. Storck, H. Bretinger and W. F. Maier, *Applied Catalysis A: General*, 1998, **174**, 137–146 (cit. on p. 25).

(124) A. L. McClellan and H. F. Harnsberger, *Journal of Colloid And Interface Science*, 1967, **23**, 577–599 (cit. on p. 25).

(125) P. I. Ravikovitch, D. Wei, W. T. Chueh, G. L. Haller and A. V. Neimark, *Journal of Physical Chemistry B*, 1997, **101**, 3671–3679 (cit. on pp. 25, 51).

(126) A. V. Neimark, P. I. Ravikovitch, M. Grün, F. Schüth and K. K. Unger, *Journal of Colloid and Interface Science*, 1998, **207**, 159–169 (cit. on p. 25).

(127) M. Kruk and M. Jaroniec, *Chemistry of Materials*, 2003, **15**, 2942–2949 (cit. on p. 25).

(128) D. Klank and C. Reichenbach, *Why do we measure surfaces and pores with argon and krypton gas adsorption much more often in future?*, tech. rep. June, 2018, pp. 26–29 (cit. on p. 25).

(129) W. L. Earl, P. O. Fritz, A. A. Gibson and J. H. Lunsford, *The Journal of Physical Chemistry®*, 1987, **91**, 2091–2095 (cit. on p. 27).

(130) A. Zecchina, L. Marchese, S. Bordiga, C. Pazè and E. Gianotti, *Journal of Physical Chemistry B*, 1997, **101**, 10128–10135 (cit. on p. 27).

(131) J. M. Kanervo et al., *Chemical Engineering Science*, 2015, **137**, 807–815 (cit. on p. 27).

(132) M. Niwa, K. Suzuki, N. Katada, T. Kanougi and T. Atoguchi, *Journal of Physical Chemistry B*, 2005, **109**, 18749–18757 (cit. on p. 27).

(133) M. Niwa and N. Katada, *Chemical Record*, 2013, **13**, 432–455 (cit. on p. 27).

(134) C. Sauer, G. J. L. de Reijer, A. Schaefer and P. A. Carlsson, *Topics in Catalysis*, 2022, 1–12 (cit. on pp. 27, 29, 37, 80).

(135) L. Rodríguez-González, E. Rodríguez-Castellón, A. Jiménez-López and U. Simon, *Solid State Ionics*, 2008, **179**, 1968–1973 (cit. on p. 27).

(136) R. J. Cvetanović and Y. Amenomiya, *Advances in Catalysis*, 1967, **17**, 103–149 (cit. on p. 27).

(137) M. Jin et al., *Angewandte Chemie - International Edition*, 2023, **62**, e202306183 (cit. on p. 27).

(138) A. Palčić and V. Valtchev, *Applied Catalysis A: General*, 2020, **606**, 117795 (cit. on p. 27).

(139) A. Wang et al., *ACS Catalysis*, 2017, **7**, 3681–3692 (cit. on p. 27).

(140) C. A. Trujillo, N. T. Ramírez-Marquez and J. S. Valencia-Rios, *Thermochimica Acta*, 2020, **689**, 178651 (cit. on p. 27).

(141) H. van Koningsveld, J. C. Jansen and H. van Bekkum, *Zeolites*, 1990, **10**, 235–242 (cit. on p. 30).

(142) T. Ungár, *Scripta Materialia*, 2004, **51**, 777–781 (cit. on p. 30).

(143) M. Hunger et al., *Journal of the Chemical Society, Faraday Transactions 1: Physical Chemistry in Condensed Phases*, 1987, **83**, 3459–3468 (cit. on p. 30).

(144) H. Kosslick et al., *Journal of the Chemical Society, Faraday Transactions*, 1993, **89**, 1131–1138 (cit. on p. 30).

(145) U. Müller and K. K. Unger, *Studies in Surface Science and Catalysis*, 1988, **39**, 101–108 (cit. on pp. 31, 46).

(146) P. L. Llewellyn et al., *Langmuir*, 1993, **9**, 1846–1851 (cit. on p. 31).

(147) B. Hunger, M. Heuchel, S. Matysik, K. Beck and W. D. Einicke, *Thermochimica Acta*, 1995, **269-270**, 599–611 (cit. on p. 32).

(148) S. Creci, A. Martinelli, S. Vavra, P. A. Carlsson and M. Skoglundh, *Catalysts*, 2021, **11**, 1–12 (cit. on pp. 32, 45).

(149) S. Creci, Ph.D. Thesis, 2021 (cit. on p. 32).

(150) F. Arena, R. D. Chio and G. Trunfio, *Applied Catalysis A: General*, 2015, **503**, 227–236 (cit. on p. 37).

(151) T. Miyamoto, N. Katada, J. H. Kim and M. Niwa, *Journal of Physical Chemistry B*, 1998, **102**, 6738–6745 (cit. on pp. 37, 60).

(152) S. W. Choi et al., *Journal of Catalysis*, 2017, **345**, 113–123 (cit. on p. 37).

(153) Y. Zhou et al., *Angewandte Chemie - International Edition*, 2020, **59**, 19592–19601 (cit. on pp. 37, 38).

(154) M. Ravi, V. L. Sushkevich and J. A. van Bokhoven, *Nature Materials*, 2020, **19**, 1047–1056 (cit. on p. 38).

(155) W. G. Kim et al., *Chemistry of Materials*, 2017, **29**, 7213–7222 (cit. on p. 38).

(156) G. D. McLellan, R. F. Howe, L. M. Parker and D. M. Bibby, *Journal of Catalysis*, 1986, **99**, 486–491 (cit. on p. 38).

(157) Y. Shizuri, S. Nishiyama, H. Shigemori and S. Yamamura, *Journal of the Chemical Society, Chemical Communications*, 1985, 292–293 (cit. on p. 40).

(158) P. Kernen and P. Vogel, *Tetrahedron Letters*, 1993, **34**, 2473–2476 (cit. on p. 40).

(159) S. Kramer and T. Skrydstrup, *Angewandte Chemie - International Edition*, 2012, **51**, 4681–4684 (cit. on p. 40).

(160) J. Deng et al., *Scientific Reports*, 2013, **3** (cit. on p. 40).

(161) R. Fernandes, K. Mhaske and R. Narayan, *Tetrahedron*, 2022, **103**, 132553 (cit. on p. 40).

(162) M. Inui, T. Ikeda, T. Suzuki, K. Sugita and F. Mizukamil, *Bulletin of the Chemical Society of Japan*, 2009, **82**, 1160–1169 (cit. on pp. 42, 43, 49, 56).

(163) E. Bourgeat-Lami, F. Di Renzo, F. Fajula, P. H. Mutin and T. Des Courieres, *Journal of Physical Chemistry*, 1992, **96**, 3807–3811 (cit. on p. 47).

(164) M. E. Kassem, M. B. Sayed, W. M. Arafa, H. M. El-Samman and I. M. Al-Emadi, *Thermochimica Acta*, 1992, **197**, 265–275 (cit. on p. 47).

(165) L. M. Parker, D. M. Bibby and J. E. Patterson, *Zeolites*, 1984, **4**, 168–174 (cit. on p. 47).

(166) E. R. Geus, J. C. Jansen and H. van Bekkum, *Zeolites*, 1994, **14**, 82–88 (cit. on p. 47).

(167) L. W. Beck and M. E. Davis, *Microporous and Mesoporous Materials*, 1998, **22**, 107–114 (cit. on p. 47).

(168) M. E. Fleet, *American Mineralogist*, 1991, **76**, 92–99 (cit. on p. 49).

(169) K. Kihara, *European Journal of Mineralogy*, 1990, **2**, 63–78 (cit. on p. 49).

(170) C. Balzer, S. Braxmeier, A. V. Neimark and G. Reichenauer, *Langmuir*, 2015, **31**, 12512–12519 (cit. on p. 51).

(171) M. Thommes, R. Köhn and M. Fröba, *Applied Surface Science*, 2002, **196**, 239–249 (cit. on p. 51).

(172) C. Hackett and K. D. Hammond, *Microporous and Mesoporous Materials*, 2018, **263**, 231–235 (cit. on p. 51).

(173) W. Di et al., *Journal of CO2 Utilization*, 2023, **72**, 102512 (cit. on p. 59).

Appendix

Appendix A

Table A.1: Chemicals used for synthesis

Catalyst set	Chemical	Formula
1, 2, 3, 4	Tetraethyl orthosilicate* (TEOS, 98 %)	$Si(OC_2H_5)_4$
1	Tetrapropylammonium hydroxide* (TPAOH, 1.0M in water)	$C_{12}H_{29}NO$
1	Sodium aluminate* (Al 50-56 %, Na 37-45 %)	$NaAlO_3$
1	Gallium nitrate† (9-10 wt % in water)	$Ga(NO_3)_3$
1	Oxalic acid*	$C_2H_2O_4$
1, 2, 3, 4	Sodium hydroxide† (98 %, pellets)	NaOH
1, 2, 3, 4	Mili-Q water (18 MΩ · cm)	H_2O
2, 3, 4	Tetrapropylammonium bromide* (98 %)	$(CH_3CH_2CH_2)_4N(Br)$
2, 3, 4	Gallium(III) nitrate hydrate* (99.9 %)	$Ga(NO_3)_3 \cdot H_2O$

* Sigma-Aldrich
† Alfa Aesar

Table A.2: Overview synthesis conditions per catalyst with the substituted metal (M), hydrothermal treatment (H.T.), calcination (calc.), and ion exchange (I.E.)

Set: Catalyst	Si/M (gel)	NaOH / Si	H_2O /Si	H.T.	1^{st} calc.	I.E.	2^{nd} calc.
1: Si-MFI(∞)	N.A.	N.A.	25	170 °C, 5 d	500 °C, 5 h[1]	N.A.	N.A.
1: Ga-MFI(33)	50	N.A.	25	170 °C, 5 d	500 °C, 5 h[1]	2·24 h[2]	550 °C, 5 h[3]
1: Al-MFI(41)	50	N.A.	25	170 °C, 5 d	500 °C, 5 h[1]	2·24 h[2]	550 °C, 5 h[3]
1: Al-MFI(11)	N.A.	N.A.	N.A.	N.A.	N.A.	N.A.	500 °C, 0.2 h
2: Ga-MFI(13)	10	0.65	37	170 °C, 5 d	500 °C, 5 h[4]	2·24 h[5]	550 °C, 5 h[4]
2: Ga-MFI(34)	22	0.37	32	170 °C, 5 d	500 °C, 5 h[4]	2·24 h[5]	500 °C, 5 h[4]
2: Ga-MFI(95)	60[6]	0.16	25	170 °C, 5 d	500 °C, 5 h[4]	2·24 h[5]	500 °C, 5 h[4]
2: Ga-MFI(238)	155	0.16	28	170 °C, 5 d	500 °C, 5 h[4]	2·24 h[5]	500 °C, 5 h[4]
3: Ga-MFI(7)	12.5	1.15	32	170 °C, 10 d	550 °C, 5 h[7]	2·24 h[5]	500 °C, 5 h[7]
3: Ga-MFI(8)	15	0.65	20	170 °C, 10 d	550 °C, 5 h[7]	2·24 h[5]	500 °C, 5 h[7]
3: Ga-MFI(17)	20	0.37	25	170 °C, 10 d	550 °C, 5 h[7]	2·24 h[5]	500 °C, 5 h[7]

[1] 5 °C/min
[2] 60 °C, 1M NH_4NO_3
[3] 4 °C/min
[4] 1 °C/min
[5] R.T., 1M NH_4NO_3
[6] Weighing error, inaccurate gallium mass
[7] 2 °C/min

Table A.3: Information about the analysed molecules of the gas stream. Xe = 12.13 eV (for CO (28), CO_2 (44), O_2 (33), Ar (40)) or Hg = 10.44 eV (all others) as ionisers. Based on a previously described analysis method with additions and adaptions [96, 134]

Compound	Formula	m/z	IR band /cm^{-1}
Other rings			
2-methylnaphthalene	$C_{11}H_{10}$	142	785.38 – 831.18
Naphthalene	$C_{10}H_8$	128	758.62 – 807.32
Indene	C_9H_8	116	2811.26 – 3176.23
2-methyl-CPO	C_6H_8O	68	1668.88 – 1809.90
3-methyl-CPO	C_6H_8O	68	1701.42 – 1811.83
Furans			
2,5-dimethylfuran	C_6H_8O	96	1168.43 – 1282.69
2,4-dimethylfuran	C_6H_8O	68	1074.17 – 1174.70
2-methylfuran	C_5H_6O	81	1117.57 – 1176.87
BTX			
Benzene	C_6H_6	78	606.51 – 726.80
Toluene	C_7H_8	92	689.44 – 769.95
o-xylene	C_8H_{10}	106	702.45 – 779.59
p-xylene	C_8H_{10}	106	735.32 – 867.92
Olefins			
Ethene	C_2H_4	27	900.12 – 1000.16
Propene	C_3H_6	42	900.61 – 1019.69
1,3-butadiene	C_4H_6	39	822.26 – 977.02
C1			
Methane	CH_4	-	3000.25 – 3176.23
Carbon monoxide	CO	28	2146.16 – 2159.90
Carbon dioxide	CO_2	44	2223.57 – 2280.94
Formaldehyde	CH_2O	30	2698.93 – 2822.36
Water	H_2O	18	1416.97 – 1502.31
Ammonia	NH_3	16	903.98 – 977.27

Conversion, selectivity, and carbon balance

The carbon mass balance is based on the inlet feed of 2,5-DMF. The carbon balance describes the difference between the inlet feed of the reactant and the sum of all detected product species during a catalytic conversion plus the amount of carbon that was deposited as coke on the catalyst surface and was later detected as CO and CO_2. The carbon mass balance was usually greater than 90 %, which means that less than 10 % of products were not identified. Some carbon is stored on the zeolite as coke and can thus only be quantified during an oxidative regeneration treatment of the catalyst after the catalytic experiment. Because of this, the shown selectivities do not take into consideration the amount of coke formed during catalytic reactions. During the catalytic experiment of 10 hours, the amount of coke deposited on the zeolite was found to be between 5 and 10% of the total carbon feed. This means that if the coke is taken into account for selectivity calculations, the given selectivities will be lower.

The carbon mass balance consists of the concentrations of all product species detected in relevant concentrations C (typically $\geq$1 %). These products include the following species: 2,4-dimethylfuran (2,4-DMF), methylfuran, 2-methyl-2-cyclopentenone (2-MCPO), 3-methyl-2-cyclopentenone (3-MCPO), benzene, toluene, indene, ethene, propene, butadiene, methane, CO and CO_2. To calculate

the conversion, the product concentrations are normalised to account for the reaction stoichiometry by multiplication with their number of carbon atoms n, followed by division by the number of carbon atoms in the reactant 2,5-DMF (6 carbon atoms). The conversion X can then be calculated according to equation 1

$$X = 1 - \frac{C_{\text{2,5-dmf}}}{\sum \frac{n}{6} \cdot C_{\text{all products}} + C_{\text{2,5-dmf}}} \tag{1}$$

Similarly, the selectivity S of each species can be calculated according to equation 2.

$$S = \frac{n \cdot C_{\text{product}}}{6 \sum \frac{n}{6} \cdot C_{\text{all products}}} \tag{2}$$